Title
Investigation of Organometallic Reaction Mechanism and Rotational Dynamics via Ultrafast Infrared Spectroscopies

Author
Nguyen, Son Chi

Publication Date
2014

Peer reviewed|Thesis/dissertation

Investigation of Organometallic Reaction Mechanism and Rotational Dynamics via Ultrafast Infrared Spectroscopies

By

Son Chi Nguyen

A dissertation submitted in partial satisfaction of the

requirements for the degree of

Doctor of Philosophy

in

Chemistry

in the

Graduate Division

of the

University of California, Berkeley

Committee in charge:

Professor Charles B. Harris, Chair

Professor Martin P. Head-Gordon

Professor Roger W. Falcone

Spring 2014

Investigation of Organometallic Reaction Mechanism and Rotational Dynamics via Ultrafast Infrared Spectroscopies

By

Son Chi Nguyen

Abstract

Investigation of Organometallic Reaction Mechanism and Rotational Dynamics via Ultrafast Infrared Spectroscopies

By

Son Chi Nguyen

Doctor of Philosophy in Chemistry

University of California, Berkeley

Professor Charles B. Harris, Chair

Vibrational spectroscopy is a powerful tool for structural characterization. Modern spectroscopy has been used ultrashort laser pulses in infrared region to monitor the structure evolution of species involving in chemical reaction. This spectroscopic technique can give dynamics of chemical reaction in ultrafast timescale, helping us understand the reaction mechanism in great detail. In this thesis, a wide range of ultrafast dynamics in solution triggered via photochemical reactions has been investigated: the photoisomerization mechanism of solar storage molecules (Fulvalene)tetracarbonyldiruthenium, the photo-inactive of analog molecules (Fulvalene)tetracarbonyldiiron, the spin state and reactivity of 14-electron species $Fe(CO)_3$ and the heat transfer from various photochemical reaction to solvent. Finally, the dynamics of molecular rotational diffusion was also investigated to measure the effect of molecular mass on rotational motion of small solute in solution. The trends discovered from these prototypical complexes are expected to be applicable to other organometallics complexes. These results will have a great contribution to the ultrafast spectroscopy as well as the synthesis research community.

To my little family,

Huyen and Nana

Contents

Acknowledgement

I attribute all my accomplishment in the past five years to the people around me. Without them, all my effort would not go very far.

I would like to express the deepest appreciation to my advisor, Professor Charles Harris, for his giving me independence to purse the research that I am interested in. Charles encourages me not only think deeply about research in our lab but also need to broaden my knowledge to other field. “Depth and broad” is his advice. I also own Charles for his recommendation on my future work, challenging me to new field to maximize my ability. Looking back over many years at Berkeley, I have been had the luckiest opportunity to work in a group that the adviser always thinks each of his students is great scientist.

I would also like to acknowledge my collaborator, Professor Peter Vollhardt, my qualifying exam and/or thesis committee, Professor Martin Head-Gordon, Professor Bradley Moore, Professor Jeffrey Long and Professor Roger Falcone, for their giving other aspects of my research and valuable advice filling hole in my knowledge.

The people deserve the biggest thank are my labmates. Their friendship makes the tough graduate school become a fascinating journey. Justin Lomont has constantly helped me with critical comments on each paper as well as his relentless supporting in correcting my bad writing. My research would not be so meaningful and productive without his help. Ben Caplins usually brings interesting topics to the conservation with his broad knowledge. Discussion with him always sparks new ideas and excitement for new experiments. Matthew Zoerb and Adam Hill had constantly gave fruitful comments on either experimental problems or scientific discussions. Zoerb had spent hundred hours keeping the laser in good shape. Adam Hill, Eric Muller and Jacob Schlegel taught me English (and slang) and random knowledge. David Suich and Alex Shearer are always available for day-to-day advice, struggles and triumphs.

I would like to extend my thanks to the group alumni, James Cahoon, James Johns and Karma Sawyer. Their exceptional mentoring will have great influence on my research career. Their success is a big motivation for me.

I would also like to acknowledge the support from NSF Grant (CHE-0909632, CHE-1213135), resources of the Molecular Graphics and Computation Facility at UC-Berkeley (grants CHE-0840505, CHE-0233882) and the National Energy Research Scientific Computing Center (supported by the Office of Science of the U.S. Department of Energy under Contract No. DE-AC02-05CH11231), and the financial support through a VIED fellowship.

Finally, I especially thanks all to my family for their love and support. My wife and my daughter have been understanding and sharing for either my late night experiment or the quite space for writing.

Chapter 1

Introduction

Studying how molecules behaves in microscopic detail is the fundamental research to understand the physical world. This knowledge also helps us control or design the chemical reaction in the way we want. At microscopic level, we want to know structure of molecules, how molecules interact each other, how they react to turn into new molecules as well as their exchange energy with environment during the course of the chemical reaction. In other words, we ultimately want to know each elemental step of a chemical reaction. To access to the molecular dynamics of these elemental steps, we have to use an appropriate spectroscopic technique that is able to gain rich structural information at high time resolution. In this thesis, our approach is ultrafast vibrational spectroscopy using ultrafast infrared laser pulses to probe the structure of molecules of interest via vibrational motion in the picosecond time regime.

Most chemistry happens in condensed phase in which the reactant, intermediate, product are surrounded by the solvent. However, the best known fundamental work on reaction dynamics are in the gas phase, in which the studied molecules are isolated. At this isolated state, the quantum states and velocity of the reactants are prepared and controlled in the crossed molecular beam experiment so that the velocity and angular distribution of the products are detected and analyzed, giving the energy landscape of the reaction.[1] Beside the molecular beam experiment, ultra-short laser pulses have been used to trigger and trace the gas phase reaction, thus the electronic excited state, vibration, rotation of intermediate and product are detected, giving the reaction dynamics at atomic scale resolution.[2,3-5] In solution, much information about the state of the system are lost due to interaction with solvent. For example, the translational and rotational states of the nascent product are obliterated within a few collisions with solvent molecules. However, vibrational states have longer lifetimes, up to picoseconds, that can be long enough to study some interesting ultrafast dynamics.[6-11] Through vibrational state does not give complete information to map the potential energy surface of the reaction, its structural sensitivity can identify intermediates and products during the course of the reaction in solution and help us understand the reaction dynamics and mechanisms in great detail. Indeed, knowing the structural evolution of species involving in the chemical reaction in solution is more practical than knowing the quantum state (translation, rotation, vibration) of that system to study the reaction dynamics. Vibrational spectroscopy is a prefect tool for probing structure with high time resolution. Time-resolved vibrational spectroscopy has been developed for many decades with the improvement of higher time resolution and broader range of probing frequency, giving rich structural information from femtoseconds to hours dynamics.[12-15]

Chemical reactions between molecules happen in probabilistic way that there is no coherent state of the reaction at a given time. This nature makes it impossible to probe the reaction dynamics due to the low probability of each dynamics at a given time. When using laser pulses, a high power coherent light source, to label particular molecules or trigger a reaction, a high population of molecules at specific state can be prepared at the same time. Under this condition, probing the reaction dynamics becomes feasible. This is the principle of

pump-probe spectroscopy. The pump pulses start the dynamics of interest in the sample, then the probe pulses track this dynamics after a short delay time. This spectroscopic method takes the advantage of ultra-short, ultrafast laser pulses to achieve high time resolution, high signal-to-noise. I used two pump-probe techniques in this thesis: the UV/Vis pump – IR probe (known as time-resolved IR, TRIR) and IR pump – IR probe (known as two dimensional IR, 2D-IR). The former technique excites electronic states to trigger a photoreaction and then probes the structural evolution to study the dynamics of photochemical reaction. The later technique excites vibrational states and traces that vibrational energy relaxation to study the dynamics of excited molecules.

Organometallic complexes are used by synthesis chemist as homogenous catalysts under mild condition. Many complexes are the prototype molecules for studying electron transfer,[16-18] charge transfer and ligand photodissociation,[19-22] bond activation[12,13,23], etc. Photodissociation of organometallic complexes causes ligand cleavage, resulting in vacant on the metal center of the photoproducts that usually (not always) allow the metal center bind to and active organic bonds.[12,24-26] In those fundamental steps of the reaction, many transition metal organometallic complexes possess different spin states with different reactivities[27-35]. Studying dynamics of these reactions provides more insight to the effect of electronic state to chemical reactivity. Organometallic complexes also have the advantage of easily being prepared with coordination ligand having the strong oscillation strength in the mid IR region, such as CO, NO, CN^-, providing a convenient condition to do spectroscopic investigation. The vibrational frequencies of these ligands are very sensitive to the electronic structure of the complexes due to the pi-back bonding donating electron from the metal center to these ligands. The vibrational lifetimes of these complexes are also relative long enough for many studies on other ultrafast dynamics, such as fluxionality,[10] vibrational coupling and vibrational relaxation,[36-39] rotational diffusion.[40] These advantages have made organometallic complexes as prototype chemicals to study the molecular dynamic and reaction mechanism.

Beside of ultrafast spectroscopy experiment, quantum mechanics calculations were also performed to assist the interpretation of the experimental data. Mostly, density functional theory (DFT) has been used in this thesis due to the reasonable cost and reliable result of this calculation method. Calculated frequency and free energy have been used to identify and characterize the experimental structures of the intermediates or photoproducts, supporting the understanding of the reaction dynamics.

Overall, the work presented in this thesis are covered in a wide range of ultrafast phenomena: photoisomerization mechanism of solar storage molecules (chapter 3), the spin state and reactivity of 14-electron species (chapter 4), heat transfer from photoreaction to solvent (chapter 5), and effect of molecular mass on rotational motion of solute in solution (chapter 6). Below is a summary of each chapter.

In chapter 3, we used TRIR spectroscopy and DFT calculation to study the photoisomerization mechanism of the (Fulvalene)tetracarbonyldiruthenium (Ru-Fuv) complex. This robust molecule absorbs sunlight, converting to a stable photoisomer which can easily release the storage energy in form of heat via catalyzing the thermal reversal. The compound was implemented within a proof-of-principle solar storage-thermal release device, demonstrating an environmental friendly closed-cycle operation. Therefore, understanding the

isomerization mechanism of the Ru-Fuv complex is necessary to develop a cheaper and more efficient rechargeable solar thermal battery. In this study, we found that the long-lived triplet biradical intermediate formed from the Ru-Ru cleavage of the parent complex plays the key role in making the photoisomerization possible. After that study, the iron analog complex was synthesized due its natural abundance and environmental benignity, opening the hope for potential large scale application. Unfortunately, the iron analogue does not undergo photosiomerization. Our TRIR spectroscopy study showed no existence of triplet biradical intermediate after the photoexcitation of the iron analogues, explaining its photo-inactive behavior. In combination of the result from the Ru and Fe complexes, this research indicates the important of spin state to the photoisomerization of these complexes. Up to now, we finally understand both the photoisomerization and thermal reversal pathway of these complexes in mechanistic detail. This provides important insight in the search for new solar storage materials based on (fulvalene)dimetal complexes.

In chapter 4, we studied the spin state as well as chemical reactivity of a 14-electron (14e) complex $Fe(CO)_3$. Photodissociation of transition metal organometallic complexes in solution is usually formed transient 16e or 17e photoproducts, in which their spin states and reactivities have been studied recently. $Fe(CO)_5$ is well known to photodissociate a single CO ligand to formed 16e species $Fe(CO)_4$. Two CO-loss photoproduct, $Fe(CO)_3$, is unexpected in condensed phase as the single CO-loss photoproduct quickly deposits its excess energy from the UV-Vis excitation to the solvent, thus prevents further CO-loss. We, however, showed that the two CO-loss product, 14e $Fe(CO)_3$, are formed significantly from the 267 nm excitation of $Fe(CO)_5$ via single photon absorption. We found that the chemistry of this 14e species is very different from the 16e species $Fe(CO)_4$ which must convert to a singlet state to coordinate to a solvent molecule. $Fe(CO)_3$ has triplet ground state and does not change it spin state upon coordination of solvent. Since $Fe(CO)_3$ is the catalyst of alkene isomerization reaction under the irradiation of $Fe(CO)_5$, this result implies that the subsequent intermediates of $Fe(CO)_3$ in the catalyst reactions could also involve triplet states. To our knowledge, this study represents the first investigation into the detailed metal–solvent interactions of a 14-electron complex on the ultrafast time scale.

In chapter 5, instead of studying the reactivity of the organometallic photoproduct, we are interested in other aspect of chemical reaction in solution: the energy exchange between reaction and surrounded solvent. In a photochemical reaction, the excitation energy required to initiate the photoreaction is usually larger than the difference in free energy between reactant and product, thus the “hot” photoproduct possesses significantly higher thermal energy than the surrounding solvent. Here, we studied the heat transfer processes from various photoproducts to solvent by monitoring the infrared absorptions of acetonitrile solvent. The absorption cross sections of acetonitrile’s infrared bands are sensitive to changes in temperature, allowing ultrafast spectral tracking of the heat transfer. In the various photoreactions studied, the solvent spectra provide information on both the dynamics and overall magnitude of the heat transfer process. We highlight the potential of this spectroscopic approach for tracking reaction dynamics by demonstrating that it is able to distinguish the slow photoisomerization dynamics of the *trans*-stilbene from that fast dynamics of *cis*-stilbene. Conventional spectroscopy probing the structural evolution of each isomer and its photoproducts has come to well-known conclusion that the photoisomerization of *trans*-

stilbene is slower than that of the *cis*-stilbene due to the existence of a small energy barrier in the excited state of *trans*-isomer. Our spectra of the solvent are sensitive enough to distinguish these two dynamics of the two isomers. This spectroscopic technique thus provides an alternative method of studying reaction dynamics by probing the temperature of local solvent environment as it changes during the course of a photochemical reaction. It has the potential of studying photochemical dynamics when probing the solute undergoing the photoreaction is difficult or impossible.

While the TRIR spectroscopy were used to study the reaction dynamics triggered by UV-Vis laser excitation pulses as described in chapter 3-5, we used 2D-IR spectroscopy in the next chapter to study the rotational diffusion dynamics by labeling the vibrational mode of molecules of interest via IR laser excitation pulses. Since 2D-IR spectroscopy can excite and monitor vibrational dipole moments, it can give dynamic information of both vibrational and rotational motions. While the vibrational motions are widely studied, there are not many researchs focused on rotational motions. Diffusive rotation represents the large amplitude motion of the molecules which is very important to understand the molecular dynamics. In this thesis, rotational diffusion time constant of each solute was measured via polarization anisotropy measurement. In this technique, a vibrational dipole moment is labeled on the studied molecules by IR laser pump pulses, the IR laser probe pulses detect the reorientation relaxation of that dipole moment, giving the rotational diffusion time of the molecule. This technique could apply to many molecules that have vibrational lifetimes long enough for the polarization anisotropy measurement. Noted that common measurement of rotational diffusion is fluorescence spectroscopy which cannot apply to all organometallic complexes since many complexes do not have fluorescence emissions. Thus 2D-IR spectroscopy is a very unique tool to study rotational diffusion of many organometallic complexes.

In chapter 6, we study the effect of molecular mass on the rotational diffusion of small molecules in solution. Hydrodynamic model, such as Debye-Stokes-Einstein equation, has been used widely to describe the rotational diffusion of solute in solution. This model considers solvent as continuum and the rotational diffusion of the solute depends on some simple variables: such as volume of the solute, viscosity and temperature of the solution, and some scale factors for the shape of solute or the solute-solvent interaction. However, this model originally deriving from macroscopic objects cannot describe well the rotational diffusion of molecules. Instead, a microscopic picture is needed to describe better this molecular motion, such as the specific shape of the solute and solvent, the specific solvent-solute interaction (hydrogen bond, dielectric friction), the mass of the solute and solvent. In this study, we focus on the effect of mass of the solute on its rotational diffusion. This mass effect has been studied for many years via isotope tracer diffusion experiments. However, these isotope tracers have little amount mass difference that the mass effect on the rotational diffusion is too small to make a strong conclusion. In our study, we used two pairs of solutes, $CpM(CO)_3$ and $M_2(CO)_{10}$ (M=Mn, Re) to measure the rotational diffusion time constants in various alkane solutions. These pairs of solutes are significantly different in mass but almost identical in volume, shape and in their expected interactions with alkane solvents, thus we isolate the effects of mass on rotational correlation times, allowing for a clearer observation of the effects of mass on rotational diffusion motion than in previous isotope studies. The heavier substitutions were observed to cause significantly slower rotational diffusion. The physical

explanation is the translation-rotation coupling of the molecular motion. The heavier molecules have slower translational diffusion and thus this translation-rotation coupling causes the rotational diffusion become slower. This result provides a clear experimental evidence for non-hydrodynamic behavior (i.e. mass dependent behavior) of the rotational diffusion of small solutes in solution.

Chapter 2
Methods

2.1. Time-resolved (or one dimensional) vibrational spectroscopy

In the first part of this thesis, ultrafast spectroscopy is applied to the picoseconds time-resolved infrared (TRIR) spectroscopy. In this pump-probe spectroscopy method (see Scheme 2.1), ultra-short (~ 1 ps) UV or Visible laser pulses are used to excite the studied molecules to electronic excited states, triggering the photochemical reactions and subsequent reactions. After a short delay, ultra-short IR laser pulses (~ 100 fs) are used to probe the vibrational frequencies of reactant and product to give information about their structure and dynamics during the course of the reaction. For organometallic complexes, the stretching frequencies of the coordinated ligands, such as CO, NO, CN^- are very sensitive to the electronic structural change of the complexes due to pi-back bonding (see Scheme 2.2). These reported ligands could change their vibrational frequencies significantly even in the case of weak coordination of solvent to the metal center. These ligands also have strong IR absorptions (strong oscillator strength) in the mid-IR region that allow us to detect species at very low concentration, such as intermediates or low quantum yield photoproducts. Besides, the observed frequencies of these ligand are mostly around 1700 - 2200 cm^{-1} region which is almost transparent to many organic solvents and air. This is a convenient condition to perform the experiment without requiring purging the apparatus of mid-IR transparent gas as well as avoiding the overlap IR absorption of the solvent. With these advantages, the TRIR spectroscopy gives rich structural information, high sensitive to chemical environment and high time resolution to study ultrafast dynamics of photoreaction in solution.

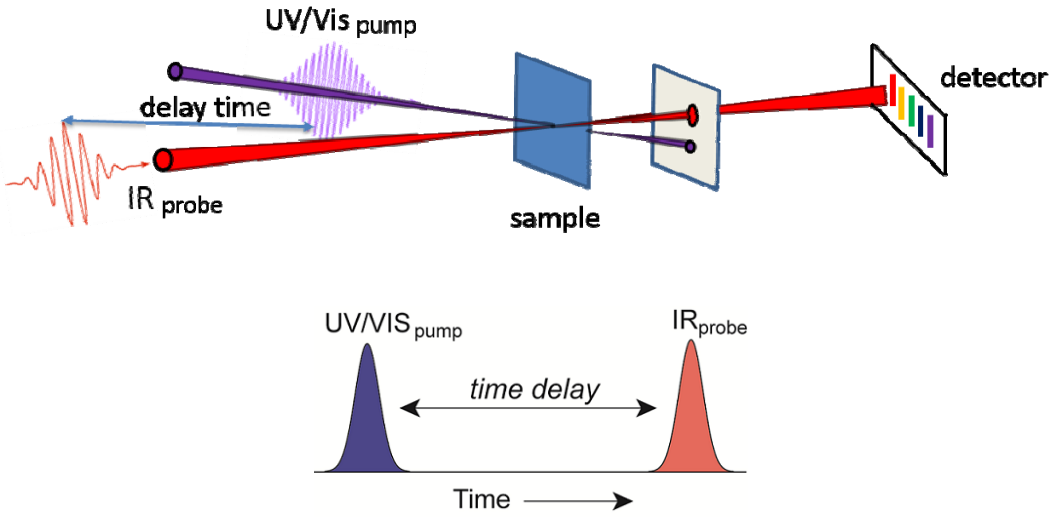

Scheme 2.1. Pump-probe geometry and sequences of laser pulses in TRIR experiment.

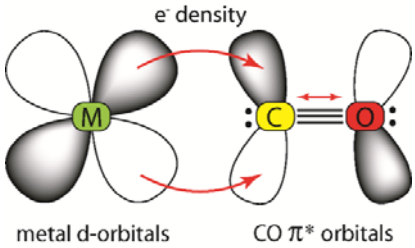

Scheme 2.2. The pi-accepting CO ligands have vibrational frequencies which are very sensitive to electronic structure change of the complex due to the amount of electron density donating from the metal center.

Photochemistry of organometallic complexes depends strongly on the wavelength of the electronic excitation. In general, low wavelength excitation mainly leads to metal-to-metal charge transfer (MMCT), resulting in metal-metal bond cleavage; while high wavelength excitation causes more metal-to-ligand charge transfer (MLCT), resulting in ligand dissociation.[24,25] In our experimental setup, the 400 as well as 267 nm excitations are both used in most experiments to gain as much information as possible about the photochemistry of the complexes. With the time resolution of 1 ps and the maximum optical delay time of 1.7 ns, ultrafast dynamics can be examined thoroughly.

2.2. Experimental setup of TRIR spectroscopy

The experimental setup has been described in detail in PhD thesis of Dr. Karma Sawyer[41] or in these publications[31,42] (see Figure 2.1). Briefly, the experimental setup consists of a Ti:sapphire regenerative amplifier (Spectra Physics, Spitfire) seeded by a Ti:sapphire oscillator (Spectra Physics, Tsunami) to produce a 1 kHz train of 100 fs pulses centered at 800 nm with an average pulse power of 1.1 mJ. The output of this commercial system is split, and 30% of the output is used to generate 400 and 267 nm pump pulses (ca. 80 and 6 μJ per pulse at sample, respectively) via second and third harmonic generation. The other 70% is used to pump a home–built two–pass BBO–based optical parametric amplifier (OPA),[43] the output of which is mixed in a $AgGaS_2$ crystal to produce mid–IR probe pulses tunable from 3.0 to 6.0 μm with a 200 cm^{-1} spectral width and a ca. 100 fs pulse duration. The 400 or 267 nm pulses pass through a 25 cm silica rod, which stretches their duration in time to 1 ps, and gives a cross correlation of the mid-IR and 400 or 267 nm pulses of 1.1 ps at the sample. The stretched 400 or 267 nm pulses are necessary to achieve a high pump fluence without generating products resulting from multi–photon excitation. The stretched pulses also reduce artifacts resulting from nonlinear optical effects in the sample cell windows.

The polarization of the pump beam is held at the magic angle (54.7°) with respect to the mid–IR probe beam to eliminate effects from rotational diffusion. A computer controlled translation stage (Newport) allows for variable time delays up to ca. 1.7 ns between pump and probe pulses. The sample is flowed using a mechanical pump through a stainless steel cell (Harrick Scientific) fitted with 2 mm thick CaF_2 windows separated by polytetrafluoroethene (PTFE) spacers with selective thickness from 25 to 2000 μm. The pump and probe beams are spatially overlapped at the sample and focused so that the beam diameters are ca. 200 and 100 μm respectively. The sample cell is moved by computer controlled translational stages

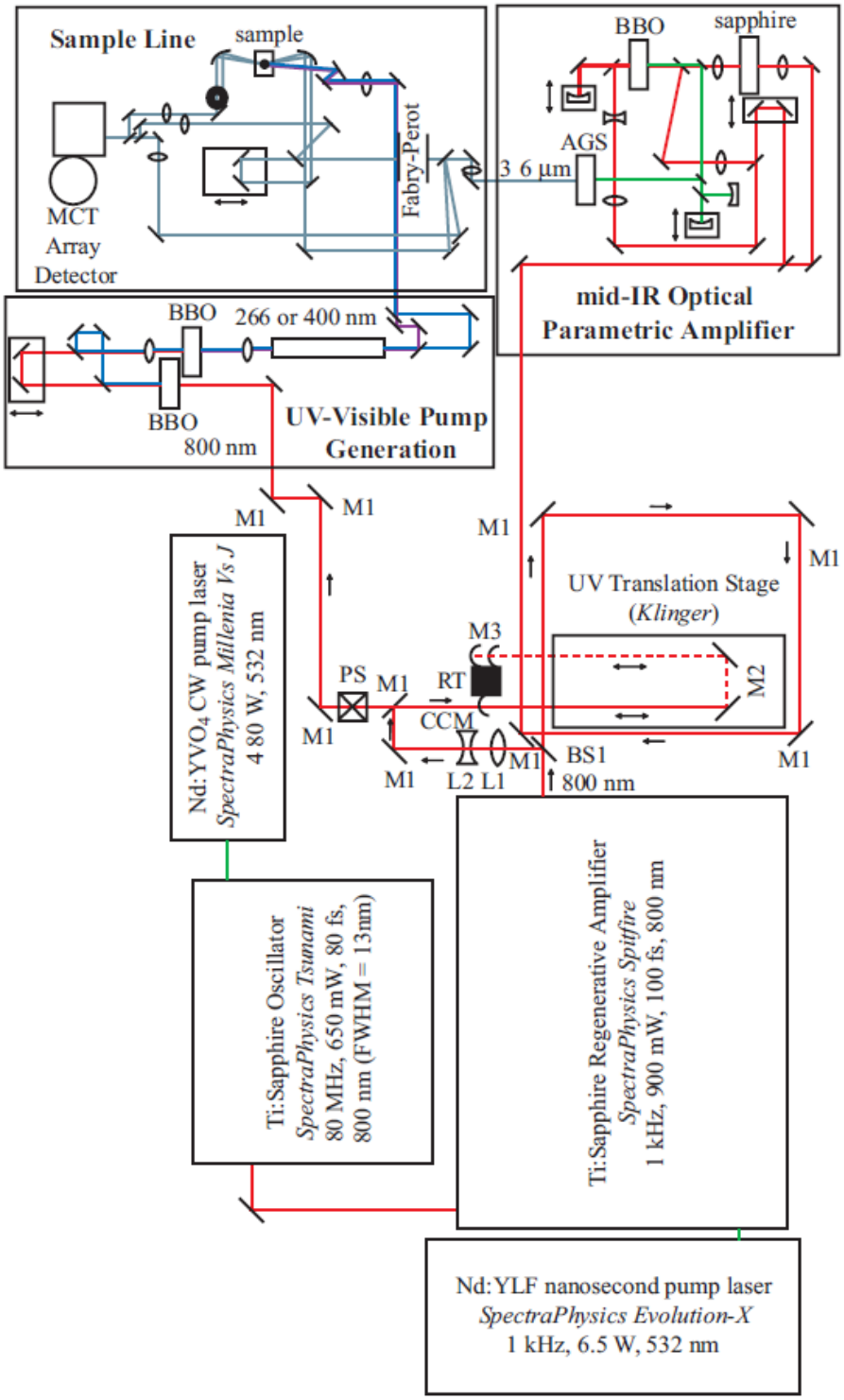

Figure 2.1. Scheme of ultrafast TRIR and 2D-IR spectroscopies. Detail of equipments, optics, operating procedures and trouble-shootings are listed in PhD thesis of Dr. Karma Sawyer[41].

(Standa) during the course of data collection so that absorptions are not altered by any accumulation of photoproduct on the sample windows. Reference and signal mid–IR beams are sent along a parallel path through a computer controlled spectrograph with entrance slits set at 70 μm (Acton Research Corporation, SpectraPro–150) and detected by a 2 × 32 element MCT–array IR detector (InfraRed Associates, Inc.) and a high-speed signal acquisition system and data-acquisition software (Infrared Systems Development Corp.) with a resolution of ca. 2.5 cm^{-1}. Collected signals are averaged over 2×10^4 laser shots to correct for shot–to–shot fluctuations of the laser system. Differences in optical density as small as 5×10^{-5} are observable after 1 s of data collection. With careful optimization, optical density difference could reach a detection limit of 1×10^{-5} within a minute of data acquisition for each spectrum.

Data collection and analysis. In this pump-probe technique, the frequency of the pump pulses is set at a haft of that of the probe pulses, thus the IR signals are collected with the UV/VIs pumped and unpumped samples. The data are presented in the format of difference spectra by subtracting the absorbance spectra of the unpumped sample from that of the pumped sample. This difference spectra give direct information of structure and dynamic change of all species involved in the photoreaction in solution (see Scheme 2.3 and Figure 2.2).

$$\Delta A_{difference} = A_{pumped} - A_{unpumped}$$

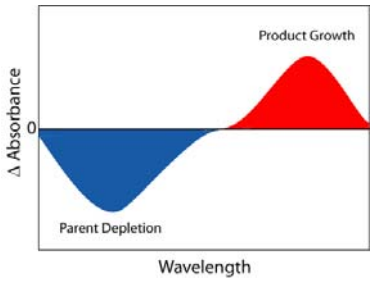

Scheme 2.3. Demonstration of a TRIR spectrum. Positive band represents the product formation while negative band represents the parent bleach.

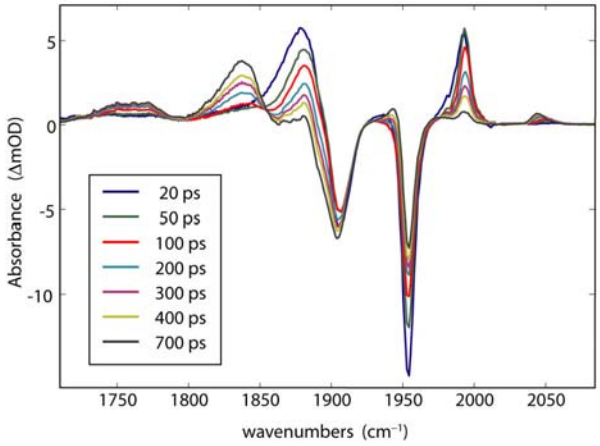

Figure 2.2. An example TRIR spectra. Positive and negative peaks are belong to the product and reactant, respectively. Positions of the peaks reflect the structure of each species while intensity changes reflect the dynamics of that species.

2.3. Two dimensional vibrational spectroscopy

In the second part of this thesis, we apply the ultrafast spectroscopy to the two dimensional infrared spectroscopy (2D-IR). This non-linear spectroscopy has been developed rapidly in recent 15 years in theory and experiment[37,44-46] as well as in application to chemistry[8,38,47-51] and biology systems.[52-55] This spectroscopy can be implemented in two ways: the time domain full four-wave mixing Fourier transform technique and the double resonance frequency domain technique. We use the later techniques in our laboratory for its convenient building. The apparatus is set up via IR pump – IR probe geometry (see Figure 2.1 and Scheme 2.4). In this experiment, an ultra-short spectrally narrow IR laser pulse labels a vibrational mode of the molecule of interest. After a short delay time, a spectrally broad IR probe pulse tracks that labeled vibration when it transfers vibrational energy to other vibrational modes via intramolecular or intermolecular vibrational relaxations. A collected spectrum is plotted at multiple narrow IR pump frequencies, creating a spectrum with two dimensions in frequency. Scheme 2.5 shows an illusion of 2D-IR spectrum with the corresponding vibrational energy level diagram. The diagonal negative peaks (in blue) correspond to the (υ=0 $\rightarrow$ υ=1) transitions while the off-diagonal positive peaks (in red) correspond to the (υ=1 $\rightarrow$ υ=2) transitions. If there is vibrational energy transfer between modes, the cross peaks (in grey) will appear. Kinetics trace of these cross peaks give dynamics of energy exchange. Figure 2.3 shows an example of conventional FT-IR and 2R-IR spectra of $Fe(CO)_5$ in alkane solution.

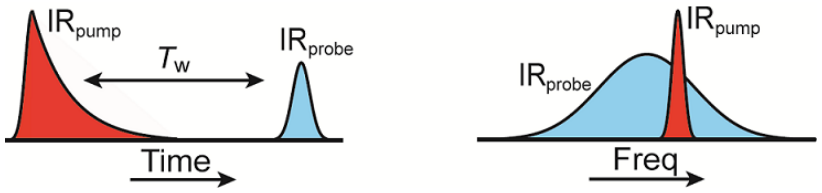

Scheme 2.4. Sequences and relative bandwidth of laser pulses in 2D-IR experiment.

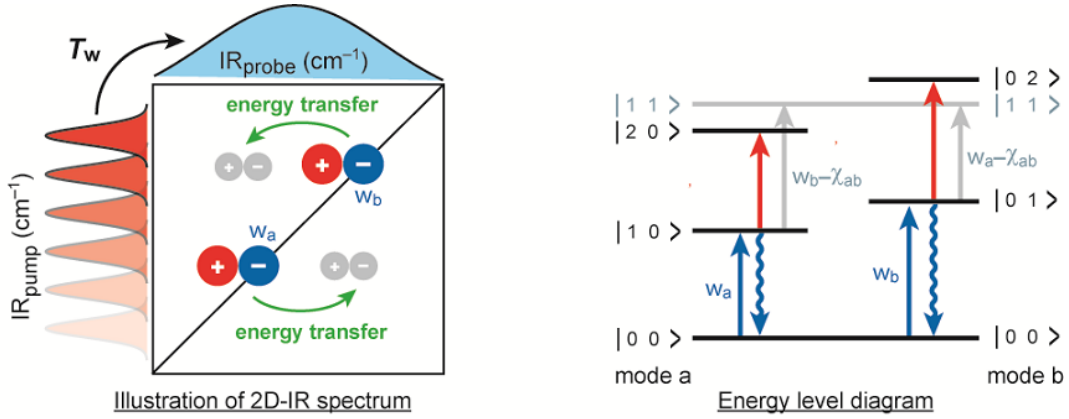

Scheme 2.5. Illustration of 2D-IR spectrum at a single delay time and corresponding vibrational energy diagram of two vibrational modes.

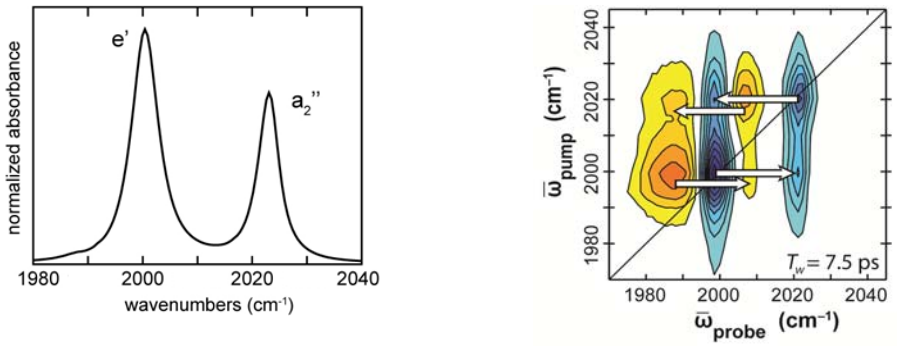

Figure 2.3. Conventional FT-IR and 2D-IR (at 7.5 ps delay) spectra of $Fe(CO)_5$[10]. The rising of the cross peaks indicates the vibrational energy exchange due to the dynamics of exchange axial and equatorial position of CO ligands (fluxional rearrangement).

Time resolved 2D-IR spectroscopy has been studied to reveal many dynamics in picosecond regime, such as: intramolecular vibrational relaxation (IVR),[36,38,50,56] intermolecular vibrational energy transfer,[47,57] isomerization,[39,58,59] ligand exchange,[10] hydrogen bond,[8,9,60,61] etc. However, there are not many studies using the advantage of this technique to study rotational motion. In this thesis, the rotational diffusion was studied via the time-dependent polarization anisotropy experiment. In this experiment, a linear polarized laser pump pulse excited a vibrational dipole moment, then the probe pulse traces the orientation relaxation of that dipole moment to extract the rotational diffusion constant, see Figure 2.4. This experiment only needs to collect the spectra right at the absorption frequency (one slide of the 2D-IR spectra) of the studied molecules with the parallel and perpendicular pump-probe polarization.

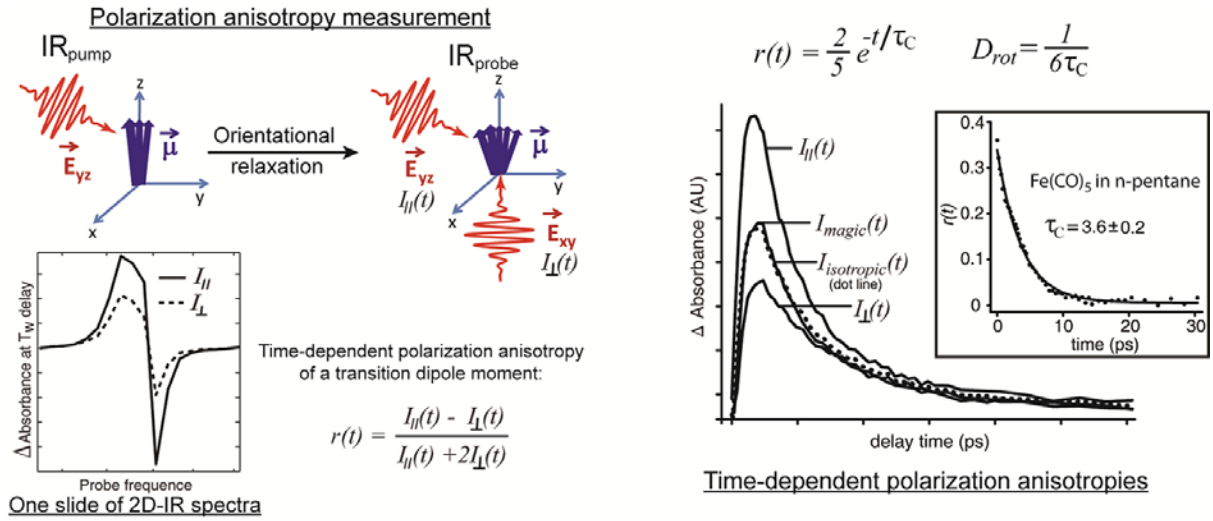

Figure 2.4. Illustration of time-dependent polarization anisotropy experiment. **μ** represents the vibrational dipole moment. $\mathbf{E_{yz}}$ and $\mathbf{E_{xy}}$ are the electric field of the pump and probe pulses in the yz and xy planes of the laboratory coordination. $I_{||}(t)$, $I_{\perp}(t)$, $I_{magic}(t)$ are the pump-probe intensities measured with parallel, perpendicular and magic angle relative polarizations,

respectively. $I_{\mathrm{Isotropic}}(t)$ is the calculated isotropic intensity from the $I_{\parallel}(t)$, $I_{\perp}(t)$. t is the delay time between the pump and probe pulses. τ_C is the rotational correlation constant or the rotational diffusion time constant.

2.4. Experimental setup of 2D-IR spectroscopy

The experimental setup has been described in detail in PhD thesis of Dr. James Cahoon[62] and Dr. Matthew Zoerb[63] or in these publications[10,40]. The experimental setup lays in the same laser table with the TRIR experiment, sharing the same commercial laser and the home-built OPA (see Figure 2.1). Briefly, the mid-IR pulses split into three beams: IR pump (84%), IR probe (8%) and IR reference (8%). The IR reference pulses are used to eliminate shot-to-shot noise of the laser system. The IR pump pulses are passed through a Fabry– Perot interferometer to narrow the pulse to c.a. 12 cm^{-1} (FWHM, Lorentzian lineshape) and extend the temporal duration of the pulse to c.a. 1 ps. The pump pulses pass the rotational haft-wave plate to control the relative polarization to the probe pulses. A linear translation stage (Newport) creates time delays between the IR pump and IR probe pulses. The pump and probe pulses then are focused and overlapped in a stainless steel cell (Harrick Scientific) with two CaF_2 windows separated by few hundreds microns PTFE spacer.

2.5. Sample handling

The quality of the spectra depends on the combination of the low shot-to-shot noise of the laser intensity, high intensity of the pump pulse, appropriate concentration of the sample and thickness of the spacer. If the concentration of the sample is too high and the spacer is too thick, there is not much IR light could pass thought the sample and come to the detector, causing less reliable subtraction in the difference spectra. If the concentration is too low and the spacer is too thin, there are not many product molecules to be detected. For the organometallic complexes in this study, a concentration of 1-5 mM or 10-20 mM in 100 - 200 μm spacer sample cell is a good start for TRIR or 2D-IR experiment, respectively.

2.6. Density functional theory modeling

Theoretical calculations have been vital to the complete understanding of spectroscopic data in this thesis. Several types of electronic structure calculations has been performed, most notably density functional theory (DFT). We typically do geometry optimizations, harmonic and anharmonic frequency calculations, potential energy surface scan, ect. All calculations describing the studied species are the gas phase calculations.

Calculations are performed with the Gaussian09 software package[64] using the BP86[65] and B3LYP[66] functionals, 6–31+G(d,p) basis set for C, O, and H, and the LANL2DZ[67,68] basis set for transition metals. We have observed that this combination of density functional and basis set yields satisfactory results for organometallic species.[10,13,30,31,69] All stable structures are optimized using tight convergence criteria, and a frequency analysis is performed to ensure that optimized geometries are genuine local minima.

Calculated IR frequencies are used without scaling. These calculated frequencies are compared to the experimental frequencies to support our assignment of species in the

reaction. It is noted that we do not compare directly the calculated frequencies to the experimental frequencies to assign the spectra because these values do not need to be the same due to our simple simulation in the gas phase condition and the limit accuracy of frequency calculation. Instead, we usually combine the calculated IR frequency result with other calculated results (such as relative free energy, binding energy, optimized geometry and symmetry, and spin state of the system) as well as the experimental data to achieve the accurate assignment.

Chapter 3
Photoisomerization mechanism of tetracarbonylfulvalenedimetal complexes - a solar storage-thermal release system

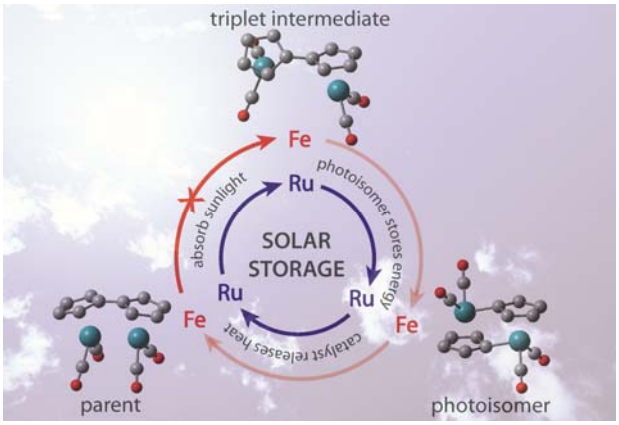

Figure 3.1. Abstract figure of chapter 3.

This chapter is reproduced in part from two published papers:

M. R. Harpham, S. C. Nguyen, Z. Hou, J. C. Grossman, C. B. Harris, M. W. Mara, A. B. Stickrath, Y. Kanai, A. M. Kolpak, D. Lee, D. Liu, J. P. Lomont, K. Moth-Poulsen, N. Vinokurov, L. X. Chen, and K. P. C. Vollhardt, X-ray Transient Absorption and Picosecond IR Spectroscopy of Fulvalene(tetracarbonyl)diruthenium on Photoexcitation, *Angew. Chem. Int. Ed., 51, 7692 (2012).*

Z. Hou, S. C. Nguyen, J. P. Lomont, C. B. Harris, N. Vinokurov and K. P. C. Vollhardt, Switching from Ru to Fe: picosecond IR spectroscopic investigation of the potential of the (fulvalene)-tetracarbonyldiiron frame for molecular solar-thermal storage, *Phys. Chem. Chem. Phys.,15, 7466. (2013).*

3.1. Introduction

A major challenge in the utilization of solar energy on a large scale is its storage.[70-74] To overcome this challenge, we must develop an effective solar energy storage technologies and materials. Recently, a (fulvalene)diruthernium complex was implemented within a proof-of-principle solar storage-thermal release device, featuring environmental friendly closed-cycle operation.[75] Unlike conventional physical-thermal storage systems (e.g. molten salt system), which require heat insulation to prevent energy loss, this chemical storage method possesses the advantage of storing solar energy in a kinetically stable photoisomer. The

photoisomer is capable of storing the captured energy for long periods of time, and can also easily release this energy "on demand" in the form of heat, when exposed to an appropriate catalyst.

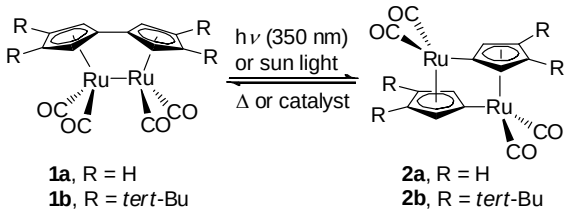

Scheme 3.1. Photoisomerization of (fulvalene)tetracarbonyldiruthenium and its thermal reversal.

In this study, a combined picosecond TRIR spectroscopic, picosecond X-ray transient, DFT computational, and laboratory time scale experimental study has elucidated the mechanism of the photostorage step in the thermally reversible photoisomerization of $FvRu_2(CO)_4$ (**1**, Fv = η^5:η^5-bicyclopentadienyl) to (μ^2-η^1:η^5-cyclopentadienyl)$_2Ru_2(CO)_4$ (**2**) (see Scheme 3.1). It encompasses fast Ru–Ru bond cleavage to both singlet and triplet syn-biradicals. The former collapses back to **1**, whereas the latter proceeds to photoisomer **2** via a triplet-singlet crossing point (**CP**) to furnish anti-biradical Fv[•$Ru(CO)_2$]$_2$ (**B**) by Cp–Cp rotation, see Figure 3.2. Species **B** then rapidly progresses to isomer **2**. The unique dynamics of this system are controlled by the sizeable barrier to rotation around the Fv single bond, which frustrates the photonic by a coupled thermal activation step (triplet→**CP**), and which enforces a preequilibrium between **2** and its anti-biradical in the thermal release process. Thus, neither process of photoisomerization nor thermal reversal are concerted, as proposed originally in steady-state experiment[76], but they involve biradical intermediates. These insights are proving valuable in the design of improved systems and in the assembly of a functioning device.

The result of the Ru system inspires the search for more economically practical and environmentally benign analogues. Next, we explore the photochemistry of the more natural abundant iron analogue. Unfortunately, the iron analogue does not undergo photoisomerization under the irradiation at any wavelength in the UV-Vis absorption. TRIR spectroscopy and DFT calculation are used to investigate why the compound is photo-inert. We found that its failure to undergo photoisomerization can be attributed to the lack of the important triplet intermediate state required for photoisomerization. Combining this work with previous studies on the Ru analogues, we now understand both the photoisomerization and thermal reversal reactions of these complexes in mechanistic detail, providing a guideline to the search for new solar storage materials based on (fulvalene)dimetal complexes. This class of complexes shows particular promise, due to their synthetically tunable electronic, solubility, and thermodynamic properties, which motivates the continued investigation toward their optimization for solar energy storage.

3.2. Studying photoisomerization of (Fulvalene)tetracarbonyl-diruthenium via Picosecond IR Spectroscopy, X-ray Transient Absorption and DFT calculation

Among of rechargeable solar thermal batteries containing photochromic molecules capable of reversible photoisomerization, organometallic compounds show particular promise, because of their complementary potential for steric and electronic tunability. In this regard, an intriguing organometallic system is the robust photo-thermal fulvalene (Fv) diruthenium couple **1⇆2** (Scheme 3.1).[76] Initially, the photoisomerization mechanism was assumed, for lack of contradicting evidence, to occur by a concerted pathway, in which both the Ru-Ru and Cp-Cp bonds are broken and the half-molecules Fv $[\bullet Ru(CO)_2]_2$ goes through a rotation to turn into the isomer **2**.[76]

A recent combined experimental and computational study of the heat releasing step **2a→1a** pinpointed a stepwise trajectory. Its salient features (Figure 3.2, black solid line) consist of a preequilibrium of **2a** (20.8 kcal mol^{-1}) with anti-biradical **B** (38.8 kcal mol^{-1}) by initial cyclopentadienyl (Cp) coupling (**TS C**, 43.2 kcal mol^{-1}), subsequent rate determining $CpRu(CO)_2$-rotation (**TS A**, 50.5 kcal mol^{-1}), and Ru–Ru bond formation to give **1a** (0.0 kcal mol^{-1}).[77] This trajectory, in particular the relative difficulty of anti to syn-biradical rotation and the ease with which **B** proceeds to **2a** ($\Delta H^{\neq}$ = 4.4 kcal mol^{-1}), prompted a reconsideration of the mechanism of the photostorage step. Originally,[76] the normally expected Ru–Ru photodissociation[78] was deemed unlikely, because added CCl_4 (1 M) had no effect on the outcome of the photorearrangement, leading again to the postulate of a concerted process. However, the lability of **B** with respect to **2a** makes it a viable photointermediate, provided that it can be reached by relaxation of an excited state of **1**. Moreover, if the result of photon absorption is indeed intermetallic cleavage, the question arises of how the system overcomes the syn to anti rotational barrier. The following experiments, executed with the relatively soluble tetra-tert-butyl derivative **1b**[79] and related computationally to the unsubstituted analog **1a**[77] (the core structures are relatively unperturbed by the tert-Bu substituents),[76] address these issues and provide a coherent picture of the photoconversion of **1** to **2**.

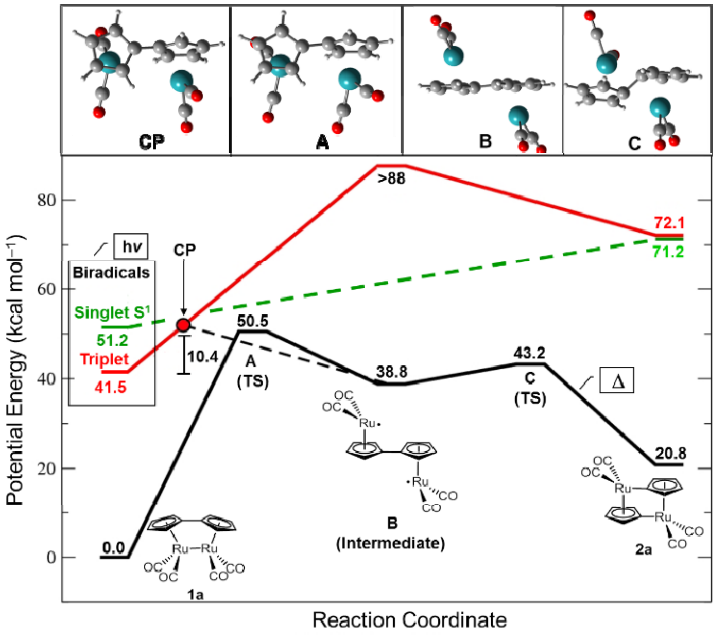

Figure 3.2. Calculated potential energy profiles for the thermal **2a→1a** manifold (black solid line), two biradical species obtained by photoexcitation of **1a** (box left), and the computed fate of these species (excited state triplet in red, singlet in green; **CP**=crossing point). Computer-rendered depictions of **A–C** and the **CP** are shown at the top. Higher excited states are omitted.

To get direct structural information of the reactive transients, we collaborated with Professor Lin Chen at Argonne National Laboratory to do X-ray transient absorption (XTA) spectroscopy.[80] This spectroscopy technique is capable of probing local metal center coordination geometry on a time scale limited mainly by the durations of X-ray pulses from a synchrotron or other light sources. The XTA measurements were performed at Beamline 11-ID-D of the Advanced Photon Source at Argonne National Laboratory. Details of this setup have been published.[80] Briefly, in a manner analogous to optical transient absorption, an ultrafast, 351 nm laser excitation pulse is used to initiate the reaction, and an X-ray pulse with a pulse duration of ~100 ps, tuned to an energy around the Ru K-edge (22.117 keV), is applied to probe the structure of the transient excited state within 100 ps. Spectra of **2b** were obtained after maximum conversion of **1b** by long exposure (ca. 8 hours) to the optical excitation.

The X-ray absorption near edge structure (XANES) region of the XTA results is shown in Figure 3.3. The XANES region is sensitive to the electronic state and coordination of the X-ray absorbing ruthenium. In control experiments, distinct differences are seen between the ground state (**GS**) spectra (without optical excitation) of **1b** and its photoisomer **2b**. On laser-illumination (**LI**) of **1b**, subtle changes are noted, which become more apparent when the full X-ray absorption fine structure (XAFS) spectra are Fourier-transformed (Figure 3.4). While the absorptions of **1b GS** and **LI** are similar in shape, the ratio between the amplitudes of the 1st and 2nd peak (the former due to scatter from Ru–C(CO), the latter to Ru–C(Cp) and multiple scattering events) varies. The large distribution of Ru–C distances is reflected in the broad peak observed in the Fourier-transformed data for **2b**.

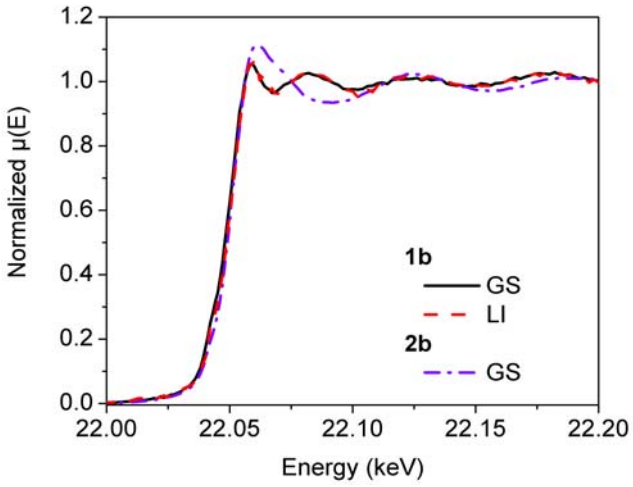

Figure 3.3. Ru K-edge XANES spectra of **1b** and photoisomer **2b** in the ground state (**GS**) and the spectrum of laser illuminated **1b** (**LI**).

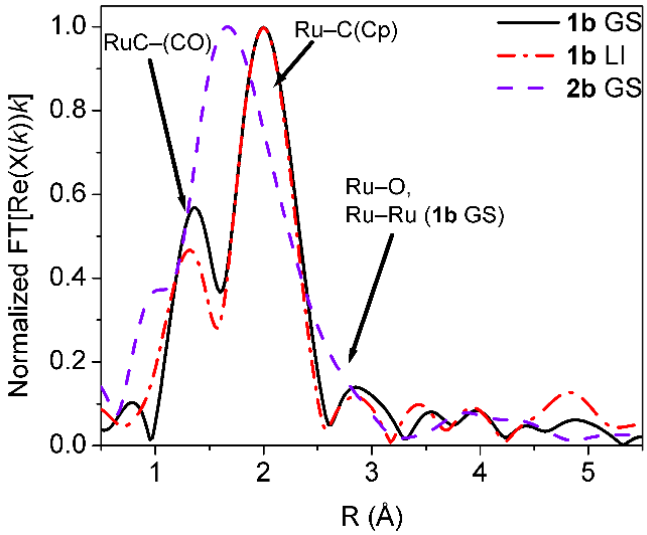

Figure 3.4. Normalized Fourier transform of the XAFS spectra of **1b** before (**GS**) and after laser-illumination (100 ps delay; **LI**), and of **2b** (**GS**). Each peak represents the average distance (not phase corrected) of neighboring atoms (arrows) from the absorbing Ru (Cp=attached cyclopentadienyl). Spectra are not phase-shift-corrected.

Employing the computed structures for the **1a**/**2a** manifold,[77] Fourier-transformed XAFS data were fit to the equation,

$$\chi(k) = \sum_i F_i(k) S_0^2(k) N_i / \left(kR_i^2\right) \exp\left(-2\sigma_i^2 k^2\right) \sin\left[2kR_i + \phi_i(k)\right]$$

in which F(k) is the magnitude of the backscattering, S_0 the amplitude reduction factor, N the coordination number, R the average distance, σ^2 the mean-squared displacement, and ϕ_i the phase shift; the subscript indicates the ith atom, k the electron wavevector. The results are shown in Figure 3.5. The ground state XAFS data for **1b** and **2b** were well-fit using the computed structures of their respective analogs **1a** and **2a**. The data for laser-illuminated **1b**(**LI**) could be fit best by a combination of the ground state **1b**(**GS**) and one intermediate species at a time delay of 100 ps. Using more than one transient structure could not be justified due to the limiting signal to noise ratio of the measurements. Hence, we chose for this purpose the structures of intermediate **B** and the topologically extreme transition states **C** and **A**.[77] The first two failed to produce satisfactory scattering profiles, while **A** fared better. Thus, varying the fractional contribution of **A** relative to **1b** from 0% (all **1b**) to 60% produced a best fit at 25% **A** and 75% **1b** (Figure 3.5, middle). Even with the caveat of the signal to noise ratio limitations, it is clear that photonic excitation of **1b** generates an entity in which the Ru-Ru linkage is ruptured and which is not **B**, **C**, or **2b**, suggesting the formation of a Ru-centered biradical with a syn configuration.

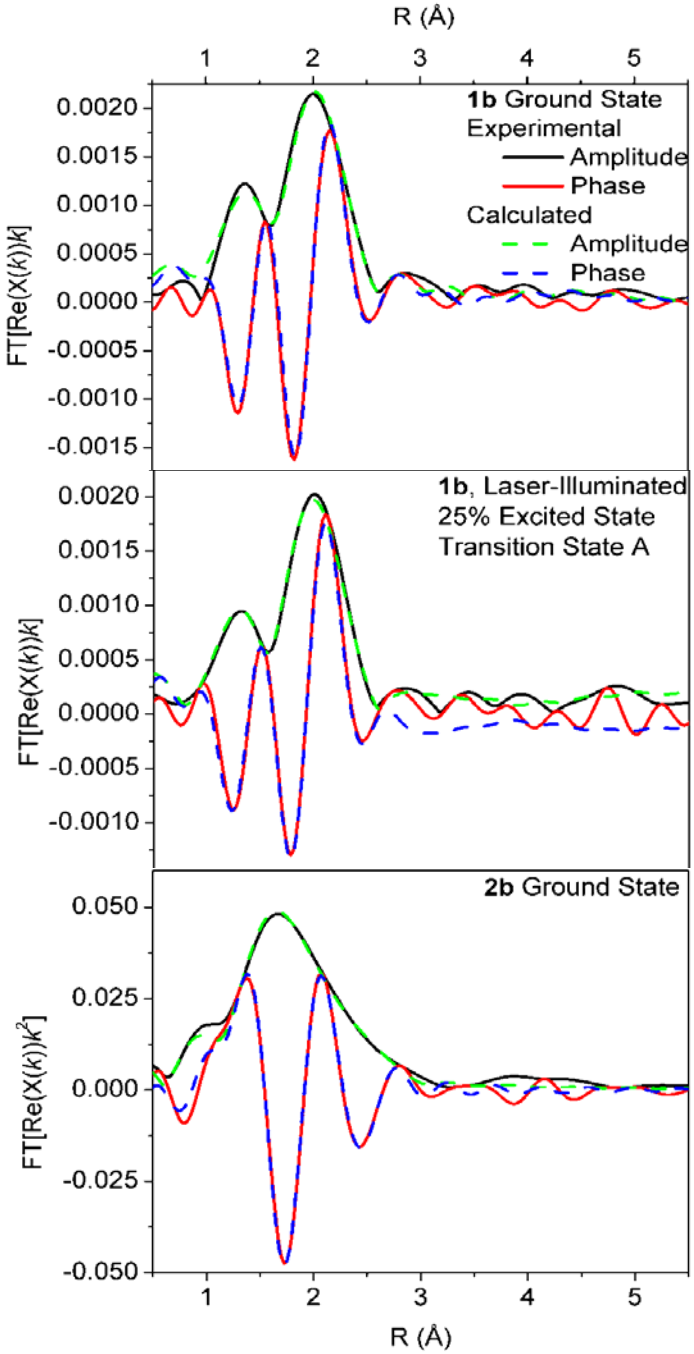

Figure 3.5. Fourier-transformed XAFS spectra for (top to bottom) **1b**, laser-illuminated **1b**, and photoisomer **2b**. Calculated results are based on computed structures. Spectra are not phase-shift-corrected.

To obtain additional information about the nature of the primary product of photon absorption, picosecond TRIR spectroscopy experiments were executed, following the course of the excitation of **1b** in heptane solution with 267 and 400 nm laser pulses, respectively. In

addition to the transient X-ray experiment, the TRIR experiment provide better time resolution (~ 1 ps) and structural features for multiple species in the reaction. Samples of **1b** used to collect TRIR spectra were prepared at a concentration of ~1 mM in *n*-heptane solution in airtight vessels, shielded from ambient light. Figures 3.6 and 3.7 show TRIR spectra of **1b** following 400 and 267 nm excitation. At delay times of <100 ps, the spectra are dominated by species **D** with three broad peaks at 1945, 1995, 2010 cm^{-1}. At delay times of >200 ps, when **D** has mostly decayed, species **E**, **F** and **2b** can be observed clearly. Figure 3.8 summarizes the spectra at short and long delay time following 400nm excitation with the assigned structures on top.

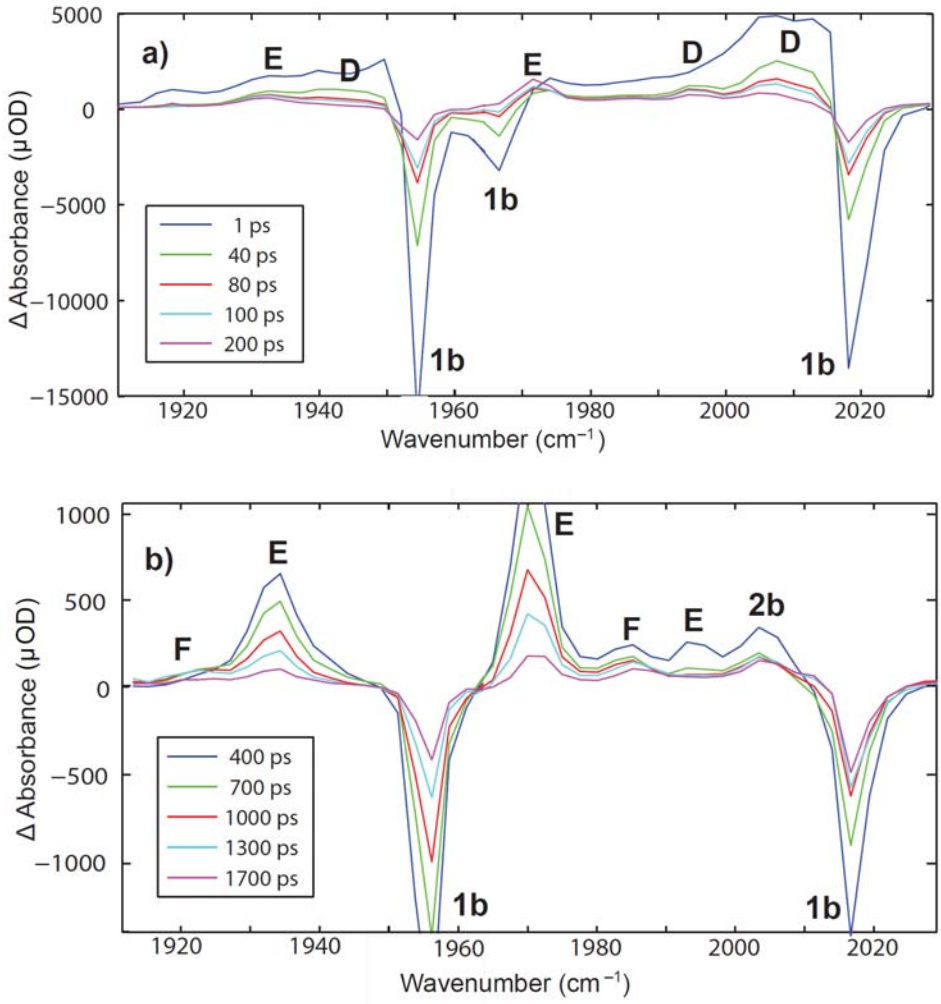

Figure 3.6. TRIR spectra of **1b** in *n*-heptane solution with 400 nm excitation pulses, using a 1800 μm spacer sample cell.

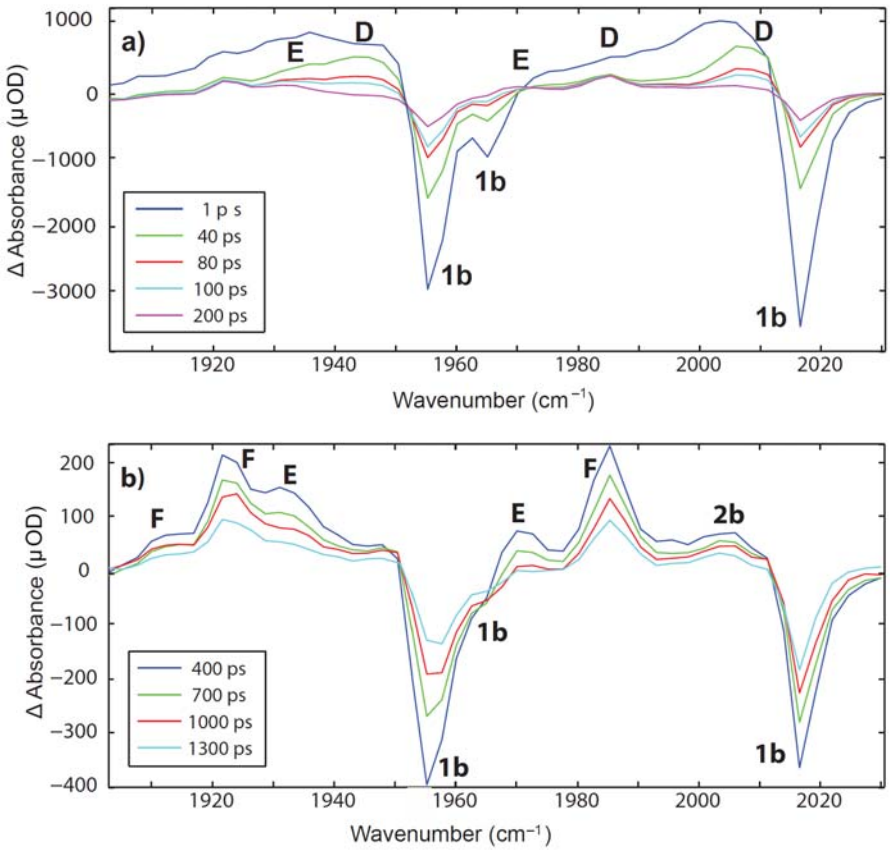

Figure 3.7. TRIR spectra of **1b** in *n*-heptane solution with 267 nm excitation pulses, using a 500 μm spacer sample cell.

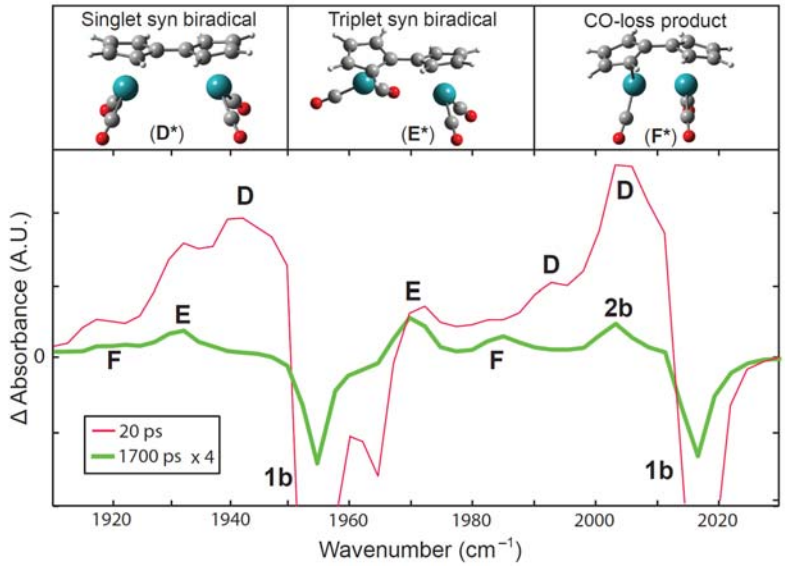

Figure 3.8. TRIR spectra of **1b** in *n*-heptane solution following 400 nm excitation. The structures depicted on top were computed for the unsubstituted analogs (*), $FvRu_2(CO)_4$ (**D***

and **E***) and $FvRu_2(CO)_3$ (**F***), using the BP86 functional and lanl2dz basis for Ru and 6-31+g(d,p) basis for all other atoms.

In general, for binuclear metal carbonyls,[24,25] the low wavelength excitation regime elicits CO loss (as observed for **1a**), the high wavelength excitation causes M-M bond cleavage (for **1a**, rearrangement).[76] With 400 nm light, new absorptions emerge at early delay times (<100 ps), which are relatively broad and dominated by a single species, but, as the latter decays, additional photoproducts become visible. Specifically, there are two sets of kinetically correlated peaks: one (**D**) comprising signals at 1945, 1995, and 2010 cm^{-1}, decaying with a time constant of ~30 ps, and a second (**E**), composed of bands at 1933 and 1970 cm^{-1} and more persistent, up to ~2 ns (see Figure 3.6 and 3.8). Both **D** and **E** disappear on the picosecond timescale correlated to that of the recovery of **1b**, consistent with the formation of transient biradicals capable of rapid recombination to starting material.[78] Since this behavior rules out the creation of tert-butyl **B** (which should go on to **2b**; Figure 3.2), we assign the entity with the faster decay to a singlet syn-biradical photoproduct **D**, and the other to its longer lived triplet relative **E** (vide infra). For comparison, the analogous near UV photolysis (>375 nm) of $[CpRu(CO)_2]_2$ produces the $CpRu(CO)_2$ radical with IR bands at 1930 and 2000 cm^{-1}.[81] The considerably weaker intensity of absorptions corresponding to **E** suggests that the primary pathway for decay of **D** is to reform **1b**, although relaxation to the more stable triplet **E** is a likely competing pathway.

We compared the photoproduct intensities in TRIR spectra using 400 nm and 267 nm excitation, and assigned the species **F** (1910, 1922, 1985 cm^{-1}) to the CO-loss product ($(tert\text{-}Bu)_4FvRu_2(CO)_3$).[82] This is the expected result for the short wavelength excitation. These absorptions reasonably match computed values for the parent $FvRu_2(CO)_3$ **F*** (1927, 1941, and 1993 cm^{-1}; intensities in agreement with experiment) and those reported for $(CpRu)_2(CO)_3$ (1935, 1964, and 1997 cm^{-1}).[81] Much smaller amounts (<1%) of species **F** appear to be formed at 400 nm (see Figure 3.8). Finally, a weak absorption at 2004 cm^{-1} is assigned to traces of isomer **2b** (authentic sample[79] $\tilde{\nu}$ film = 1932 and 1993 cm^{-1}).

To obtain further information about the nature of **D** and **E**, DFT was again applied to the parent analogs **D*** and **E*** (Figure 3.8. top). Of the two entities, only **E***, 41.5 kcal mol^{-1} more energetic than **1a**, provided a stable local minimum with $\tilde{\nu}$ calcd = 1945, 1990, and 2003 cm^{-1}, in consonance with experiment (for the two observable bands). Its topology features an intermetallic distance of 4.530 Å and a dihedral angle around the Cp-Cp bond of 37.53°. The "stability" of **E** in silico is consistent with its longer lifetime in solution relative to **D**. While the high spin-orbit coupling expected for a Ru-complex should facilitate interconversion between spin states, there appears be a small enthalpic barrier to reaching the crossing point from **D** to **E**. Because optimization of a singlet syn-biradical structure led to collapse to **1a**, for purposes of illustration an artificial topology was modelled by inserting butane into the Ru-Ru bond and subsequently deleting the solvent molecule (see Appendix A).[83] The resulting **D*** has a Ru-Ru separation of 4.790 Å and a dihedral angle around the Cp-Cp bond of 1.51°. In short, TRIR experiment confirms Ru-Ru bond rupture as the primary step of the photoconversion of **1** to **2** and the formation of a relatively stable triplet biradical species.

How do any of the postulated intermediates reach photoisomer **2**? To answer this question, we resorted to first principles DFT calculations (in collaboration with Professor Yosuke Kanai at University of North Carolina at Chapel Hill) using the methodology applied in the elucidation of the mechanism of the thermal reversal of **2a** to **1a** (Figure 3.2, black solid line).[77] Mapping minimum-energy paths from the excited singlet or triplet electronic states indicated endothermic trajectories (Figure 3.2, green and red line, respectively).[82] However, starting from the triplet **E***, a crossing point (**CP**) to the singlet surface on route to **2a** could be located at 10.4 kcal mol^{-1}, allowing access to intermediate B (Figure 3.2, black dashed line), from which further isomerization to **2a** is known to be facile.[77] The topology of the **CP** is similar to that of **TS A** for syn-anti isomerization of the biradical, with a Ru-Ru separation of 4.270 Å and Cp-Cp dihedral angle of 85.87°. It thus appears that the primary step in the mechanism of the photostorage step **1→2** is "classical"[24,25] metal-metal bond dissociation. However, the resulting triplet syn-biradical faces a thermal hurdle before it can proceed to product via intermediate **B**.

The above postulate prompted additional preparative experiments. To confirm the absence of polar excited states or intermediates, the relative extent of conversion of **1b** to **2b** was monitored in hexane, heptane, toluene, and THF, respectively [hν, 350 nm, aq. $NaNO_2$ (75% w/v) filter, 1 min, 30°C], revealing little variance (relative ratios of 2b:1b=3.9:3.8:2.7:1.0), consistent with the emerging mechanistic picture. A second, more telling study addressed the presence of a **CP** that requires 10.4 kcal mol^{-1} of thermal activation to be reached from **E** on the way to **2b**. The intervention of such a barrier was indeed corroborated by the discovery of temperature dependence of the photoconversion of **1b** to **2b** [9.3 mM in toluene, hν=350 nm, aq. $NaNO_2$ (75% w/v) filter, 5 min]. Whereas at 40°C there was 20% conversion, this number decreased steadily on lowering the temperature (e.g. 20°C, 11%; 0°C, 6%; –20°C, 3%; –60°C, 0%). Thus, low temperature photolysis renders the ensuing syn-biradical unproductive with respect to isomerization to **2b**, suggesting that it may be trappable. Indeed, while prolonged irradiation (100 min) of **1b** at –38°C in THF gave only 5.4% conversion to **2b**, added CCl_4 (1:1 v/v) caused 31% of **1b** to disappear to engender cleanly two new compounds, namely the conventional chloride abstraction product **3**[77] and the novel adduct **4**, bearing a demetallated, trichloromethylcyclopentadiene ring (Figure 3.9), in addition to **2b** (ratio=20:7:3). A control showed that **3** is stable under the conditions of its generation and not a precursor to **4**. While anti-biradical type **B** generated thermally from **2b** (CCl_4, 70° C),[77] also produces **3**, its intervention is ruled out not only by the low temperature conditions, but also by the absence of **4** in this experiment. We speculate that the emergence of this unique addition product is the result of the syn-conformation of the diruthenium species, which facilitates the capture of $\cdot CCl_3$ by the second $CpRu(CO)_2\cdot$ unit after initial abstraction of $Cl\cdot$ from CCl_4 by the first, probably in the solvent cage.[84] These data complement the mechanistic picture painted by the other techniques brought to bear on this problem.

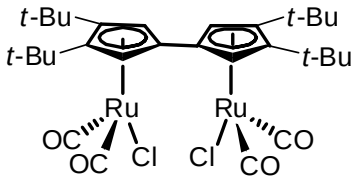

3

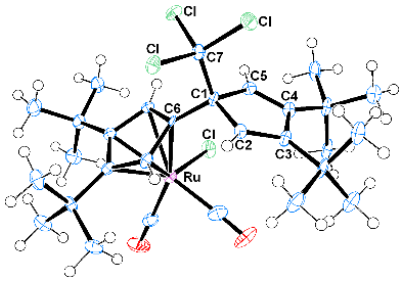

4

Figure 3.9. Products **3** and **4** (structure confirmed by X-ray crystallographic analysis) of the low temperature irradiation of **1b** in the presence of CCl_4. Selected bond lengths [Å] and angles [°] for **4** (one of two molecules in the unit cell): Ru–$Cp_{centroid}$ 1.871, Ru–Cl 2.4113(12), C1–C6 1.512(6), C1–C2 1.506(6), C2–C3 1.343(6), C3–C4 1.526(6), C4–C5 1.345(6), C1–C5 1.493(6), C1–C7 1.566(7), C7–$Cl_{average}$ 1.781.

In conclusion, a combined picosecond transient X-ray and IR spectroscopic, DFT computational, and laboratory time scale experimental study has elucidated the mechanism of the photostorage step in the thermally reversible isomerization of **1** to **2**. It encompasses fast Ru–Ru bond cleavage to both singlet and triplet syn-biradicals, the latter one of which proceeds to photoisomer **2** via a triplet-singlet crossing point to furnish anti-biradical **B** by Cp–Cp rotation, the former relaxes to the parent complex **1**. This result highlights the role of long-lived triplet syn-biradicals intermediate **E** in making the photoisomerization possible. The repulse on the triplet energy surface (see Appendix A) supports the Cp-Cp rotation for initiating isomerization process. This result provides a key reference in the next study on the iron analog complex.

3.3. Studying photoisomerization of (Fulvalene)tetracarbonyl-diiron via Picosecond IR Spectroscopy and DFT calculation

We have been study the fulvalene (Fv) diruthenium system **1⇆2** (Scheme 3.1) in previous section. In summary, **1** photobleaches in the sun (or, optimally, hν with $\lambda \geq 400$ nm), quantum yield = 0.15, in preparative runs quantitatively, to **2**, from which it is recovered completely by thermal reversal or catalytically (1–10% $AgNO_3$ on silica) with the release of ~20–23 kcal mol^{-1} (energy density 0.2 MJ kg^{-1}).[75-77,85] The bis(1,1-dimethyltridecyl) derivative **1c**,**d** has been implemented in a proof-of-principle solar storage-heat release device.[75] Both steps of the cycle are now well understood on the basis of experimental and DFT data. Thus (as depicted in Fig. 1 for **1a⇆2a**), **1a** (relative energy 0 kcal mol^{-1}) proceeds to **2a** (20.8 kcal mol^{-1}) via photoexcitation through the intermediacy of a triplet syn biradical, in which the Ru–Ru bond is broken. This species faces a barrier to rotation of 10.4 kcal mol^{-1}, represented by a crossing point **CP**, which leads directly to anti-biradical **B** (38.8 kcal mol^{-1}). The latter then rapidly (barrier **C** = 4.4 kcal mol^{-1}) rearranges to **2a**.[85] Conversely, the thermal release step is characterized by a pre-equilibrium between **2a** (20.8 kcal mol^{-1}) and **B**, followed by rate determining rotation via transition state (**TS**) **A** (50.5 kcal mol^{-1}) to (re)generate **1a**.[77]

In envisaging practical applications of the solar-thermal couple **1⇆2**, a major drawback is the requirement for ruthenium, a very rare element (abundance in the earth's crust ~1 ppb), hence expensive [$Ru_3(CO)_{12}$: ~$100/g]. It is also considered toxic. A much cheaper and environmentally benign alternative would be its higher neighbor in the triad, iron. A DFT appraisal of the thermal manifold **3a⇆4a** (Scheme 2 and Fig. 3.9) reveals that its potential photothermal storage capacity is still appreciable, 15.9 kcal mol^{-1},[77] but that the dynamics of the thermal reversal are very different. The first step, Cp–Cp coupling (**TS C**) is now rate determining and much less energetic (with a barrier of 17.3 kcal mol–1), rendering the prospects of room temperature isolation of **4a** dubious. Moreover, the photoconversion step of **3a**, assuming that it involves a trajectory analogous to that shown for Ru, would involve a biradical intermediate **B**, whose progress toward **4a** is not only relatively more encumbered (barrier via **C**: 7.8 kcal mol^{-1}), but also compromised by competition with regeneration of **3a** (barrier via A: 7.1 kcal mol^{-1}). Indeed, a cursory check using **3b** (irradiation in a Rayonet reactor, 350 nm, THF, 6 h) showed no change of starting material (NMR).[79] The present study was aimed at exploring the $FvFe_2$ framework in sufficient depth to understand its underlying features and establish its potential for photostorage.

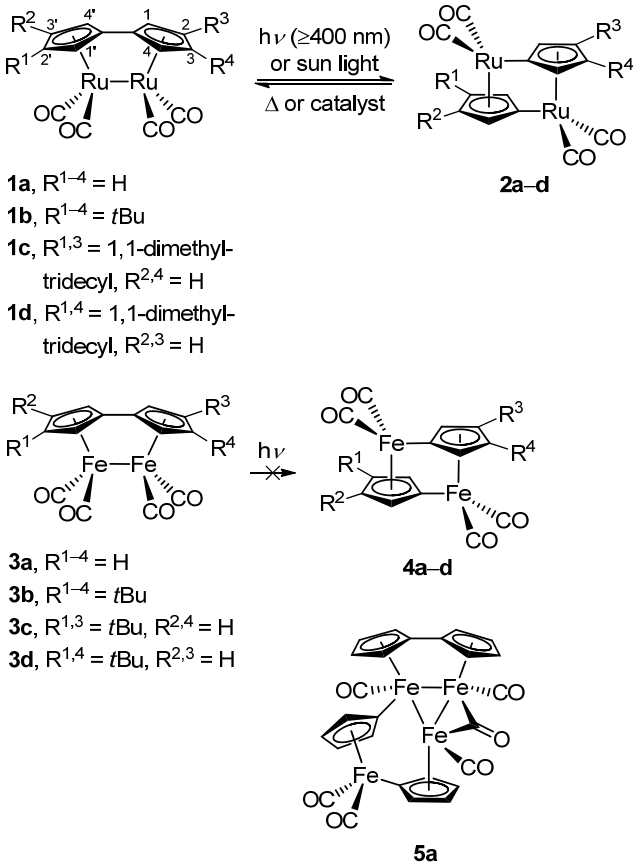

Scheme 3.2. Photoisomerization-thermal reversal systems **1**–**4**. The present study was aim to synthesize **3** as starting material, then investigated why **3** does not undergo the photoconversion.

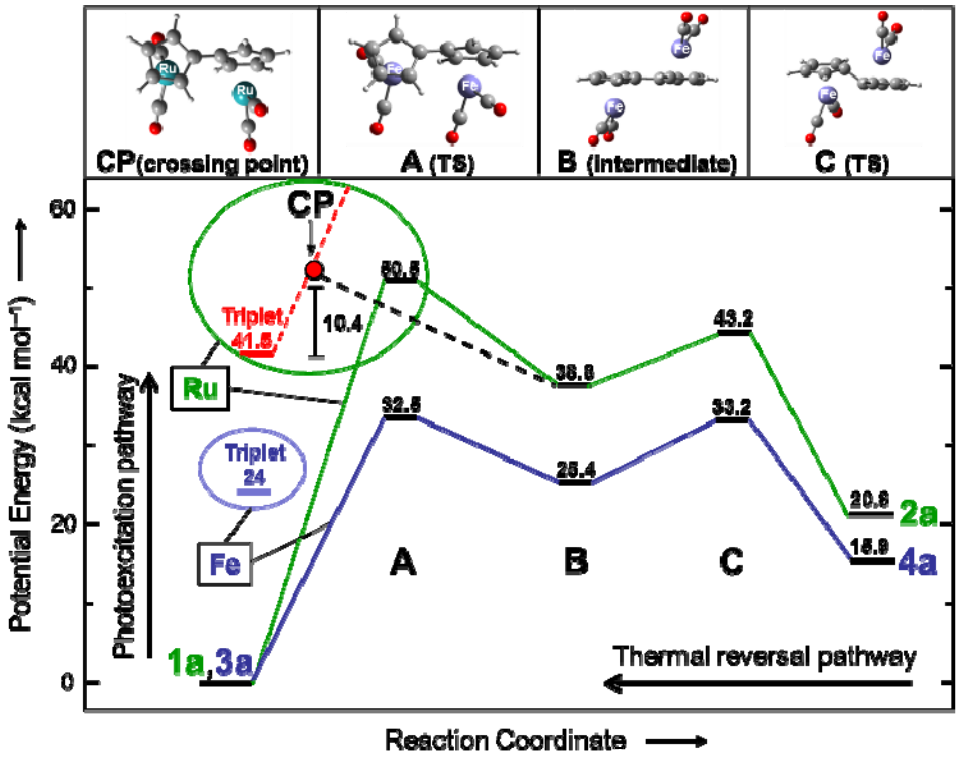

Figure 3.9. DFT computational energies of key species for: 1) the photoconversion of **1a** to **2a** and the thermal reverse (green), and 2) the corresponding cycle **3a**⇆**4a** (blue). Computer-rendered depictions of **A**–**C** (Fe) and the **CP** (for Ru) are shown at the top. Other excited states are omitted.

The first task was to gain convenient access to suitable starting materials. Metal-metal bonded first row transition metal Fv complexes are exceedingly rare.[86-88] For Fe, they were, at the outset of this work, restricted to **3a**, **3b**, and 1,1',3,3'-tetra(tert-butyl)fulvaleneFe$_2$(CO)$_4$ (**5a**). Parent **3a** had been obtained previously, serendipitously through a low-yielding multi step route that was impractical for our purposes.[89] Similarly, **3b**, while the end point of a designed synthesis, required 7 steps for its assembly.[79] Finally, **5a** was not considered because it appeared sufficiently restricted conformationally to prevent the syn-anti rotation needed to undergo photoisomerization,[90] as confirmed by the inertness of the corresponding Ru system under standard photochemical conditions.[91] Gratifyingly, however, the synthetic challenge was met by developing expedient one-pot syntheses of **3a** and the new complexes **3c** and **3d**. Thus, the former became accessible via a modification of the protocol that furnished **1a** and its congeners, but was unsuccessful for **3a**,[92] namely the direct metallation of a purified dihydrofulvalene solution with Fe(CO)$_5$. The key alteration (see ESI in Ref. [93]) was the employment of the higher boiling solvent o-xylene (b.p. 144 °C), as opposed to 1,2-dimethoxyethane (DME; b.p. 85 °C). In this way, **3a** was obtained from NaCp(DME) in one operational sequence in 34.1% yield. Equally conveniently, the highly soluble derivatives **3c** and **3d** were accessed starting from 6,6'-dimethylfulvene by successive treatment with MeLi,[94] I_2, and Fe(CO)$_5$ in 26% yield (Scheme 3.3 and ESI in Ref. [93]). An X-ray structural analysis of **3a** (Fig. 3.10)[95] is instructive in comparison with that of **1a**[76] and [CpFe(CO)$_2$]$_2$.[39] Similar to its Ru relative, **3a** adopts a strictly terminal CO ligand configuration, both in the

solid and in solution.[89] This contrasts with the unlinked CpM dimers, which exist in various forms: bridged, unbridged, cis, and trans,[39] and is the result of the constrains imposed by the Fv frame. The two Cp rings are only slightly twisted (with near eclipsing carbonyls), but the angle between their mean planes (the Fv "bend")[86] is a relatively large 32.8° (cf. 1a, 28.5°). Strain is also evident in the elongated Fe–Fe bond distance (2.7431 Å), compared to that in cis-$[CpFe(CO)_2]_2$ (2.531 Å).[96]

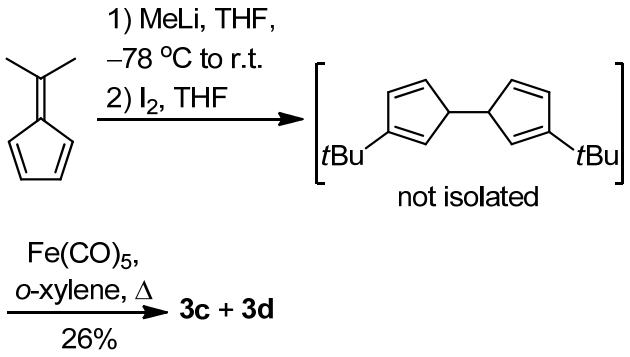

Scheme 3. Synthesis of di(tert-butyl)fulvalene iron complexes **3c**,**d**.

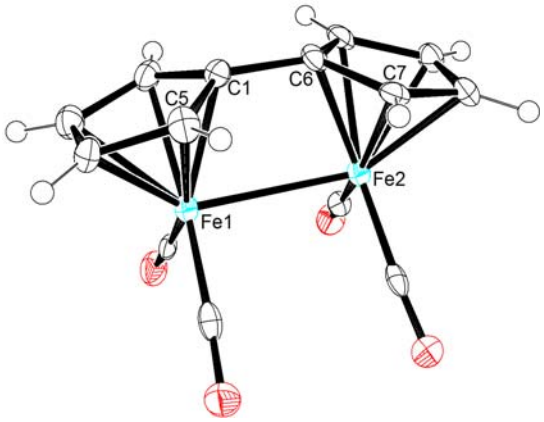

Figure 3.10. ORTEP diagram of **3a**. Thermal ellipsoids are set at 50% probability. Selected bond lengths (Å) and angles (°): Fe–Fe 2.7431(8), C1–Fe1 2.083(4), C1–C6 1.469(5), C6–Fe2 2.069(2), C5–C1 1.416(6), C6–C7 1.418(5), $Cp1_{centroid}$–Fe1 1.716, $Cp2_{centroid}$ –Fe2 1.712, Fe–$CO_{average}$ 1.762, C–Oaverage 1.155, C5–C1–C6–C7 3.3, Fe1–Cp1centroid–$Cp2_{centroid}$–Fe2 3.53, $Cp1_{centroid}$–$C1/6_{centroid}$ $Cp2_{centroid}$–Fe2 159.4.

In contrast to the yellow Ru analogues, the Fe complexes are deep red, as quantified in the UV/Vis spectra that exhibit peaks at λ_{max}(THF) ~270, 310, and 370 nm, a shoulder at ~450 nm, and end absorptions tailing >600 nm. In short, structural and spectral data appear to make **3** an ideal candidate for photoinduced Fe–Fe bond rupture. Surprisingly, however, **3a–d** proved remarkably resilient to any photoconversion. Thus, on irradiation under the same conditions as those employed used for the Ru system ($\lambda \geq 400$ nm, Newport Corporation photo filter 65CGA-400, or 325-375 nm, Rayonet) in various solvents (THF, C_6H_6, toluene), there was no observable change (^{1}H NMR). Prolonged light exposure caused slow, in the presence of excess PEt_3 (10 equiv), fast decomposition (**3a** or **3c**,**d**, THF). To probe the

possibility that photoisomerization to **4** was occurring, but not observable because of rapid thermal reversal at room temperature, these experiments were repeated at –45 °C (**3b**) and 0 °C (**3a**), to no avail. The triplet biradical can be minimized by DFT computation and lies energetically 24 kcal mol^{-1} above **3a** (Figure 3.9). To investigate the option that, if reached, it was slow in crossing over to intermediate B, irradiation of **3a** was performed at temperatures up to 70 °C, with no change in the outcome. Interestingly, high energy UV light (275 nm, THF, Rayonet, quartz tube) elicited only slow degradation of the sample in the absence of decarbonylative dimerization to **5a** (Scheme 3.2), a tetranuclear cluster of the type isolated for **1a**.[76] Since the latter was surmised to arise via **2a**, the combined preceding results raised the spectre of a fundamentally different photochemical behaviour of **3**.

To shed light on the primary step involved on photoexcitation of the Fe system, we carried out a picosecond TRIR spectroscopic investigation, patterned after that executed previously for Ru with **1b**.[85] There, it was observed that photon impingement effected Ru–Ru bond dissociation to a pair of transiently lived 17-electron syn biradicals: a singlet and its triplet analog. While the former rapidly reforms starting material with a time constant of 30 ps, the triplet persists on the timescale of ≥ nanoseconds. It is this species that is ultimately responsible for photoisomerization to **2b** (Fig. 3.9). Could it be that **3** behaves differently, thus perhaps shedding light on its failure to exhibit the desired chemistry?

Because of the relatively poor solubility of **3a** in the requisite heptane solvent, we turned to the highly soluble diastereomer mixture **3c**,**d**. Its dynamics were followed after excitation with 267 and 400 nm laser pulses. Samples of **3c**,**d** used to collect TRIR spectra were prepared at a concentration of ~1 mM in *n*-heptane in airtight vessels, shielded from ambient light. With 400 nm excitation, species **D** shows broad bands at 1943, 2008 cm^{-1}, decaying with a time constant of 28 ± 2 ps (time constant for the 1943 cm^{-1} band), consistent with the concomitant recovery time of 27 ± 2 ps (time constant for the 1960 cm^{-1} band) of the starting material bleaches at 2015, 1960, 1953 (shoulder) cm^{-1} (Figure 3.11). With 267 nm excitation, the analogous time constants are 36 ± 3 (1943 cm^{-1} band) and 39 ± 5 ps (1960 cm^{-1} band), respectively (Figure 3.12). The signals for starting material **3c**,**d** recover on a timescale commensurate with the decay of species **D** and show no changes in intensity at longer delay times (Figure 3.14). Species **D** is assigned to the singlet syn biradical photoproduct formed upon cleavage of the Fe–Fe bond on the basis of its kinetic kinship to the Ru analog, both of which exhibit the timescales typical of primary geminate recombination of 17e radicals upon M–M cleavage.[78,83,97]

In the spectra obtained after either 267 or 400 nm excitation, at long delay times (beyond ca. 300 ps), the starting material molecules are not regenerated completely. A minor product (**E**) exhibits absorptions at 1921, 1930, and 1991 cm^{-1} (Figures 3.11-3.13), the intensities of which remain invariant at much longer delay times (>300 ps; the dynamics at earlier delay times are attributed primarily to overlap with the bands of **D**). Moreover, its IR absorptions virtually coincide with those reported for $CpFe(CO)_2\cdot$ obtained by flash photolysis of $[CpFe(CO)_2]_2$ (2004 and 1938 cm^{-1}).[98] The data for **E** are consistent with the product of monodecarbonylation, tert-$Bu_2FvFe_2(CO)_3$, containing all terminal CO ligands.[78] Thus, its IR bands reasonably match calculated values for $FvFe_2(CO)_3$ (1932, 1940, 1989 cm^{-1}, with a similar ratio of intensities to those observed experimentally; see Appendix A) and experimental data for $[CH_2(\eta^5\text{-}C_5H_4)_2]Fe_2(CO)_3$ (1918, 1925, and 1991 cm^{-1} in a methane

matrix).[78,81] Consistent with its formulation as a decarbonylated species,[24,25] its relative abundance doubles (from 5% to 10%) on switching to 267 nm excitation pulses. To calculate the percent of CO-loss product relative to the total number of starting material molecules initially excited, we compare the intensities of the starting material peaks at long delay time (500 ps) to those at 1 ps delay. Due to the spectral overlap of the species **D** with **3c**,**d** at 1ps, Lorentzian fitting is used to obtain accurate intensities for the latter. The fraction of CO-loss product formed is ca. 5% and 10% using 400 and 267 nm excitations, respectively. These values are significantly larger than those for the Ru analog system (< 1% at either 400 or 267 nm excitation).[85]

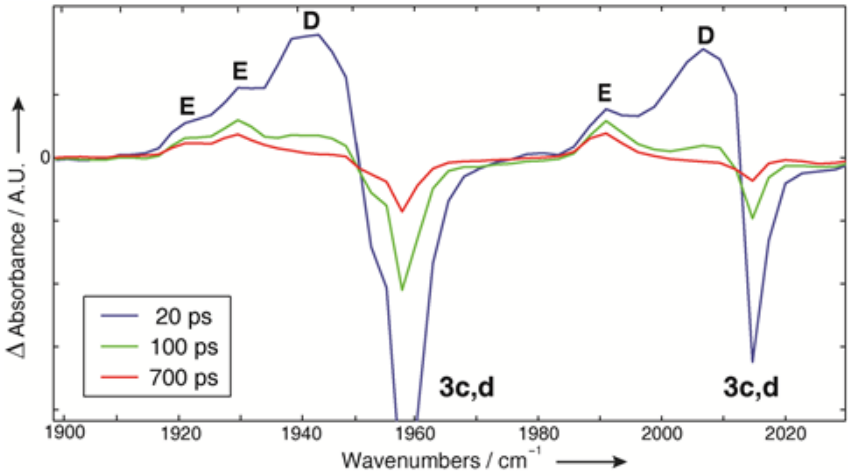

Figure 3.11. TRIR spectra of **3c**,**d** in *n*-heptane solution, following 400 nm excitation.

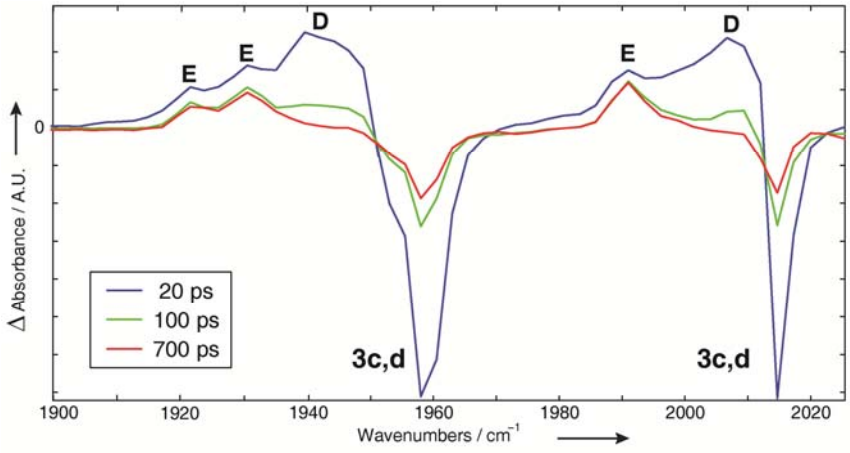

Figure 3.12. TRIR spectra of **3c**,**d** in *n*-heptane solution, following 267 nm excitation.

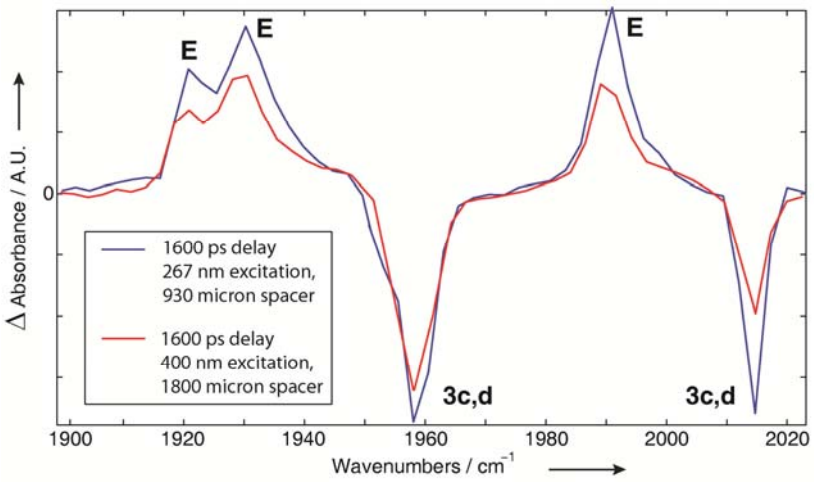

Figure 3.13. TRIR spectra of **3c**,**d** in *n*-heptane solution after 267 and 400 nm excitations at long delay time. The 400 nm excitation spectra were recorded with a thicker spacer (1800 μm) sample cell to improve the signal-to-noise ratio.

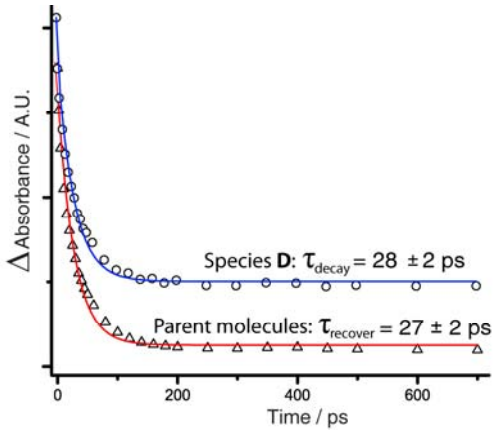

Figure 3.14. Kinetic traces of the decay of singlet syn biradical photoproduct **D** and the corresponding recovery of starting **3c**,**d** in *n*-heptane solution, following 400 nm excitation.

To summarize, the TRIR spectra show only two transient species following photoexcitation: the short-lived singlet biradical **D** and the CO-loss product **E**. Significantly, there is no evidence for the formation of a long-lived triplet biradical arising from Fe–Fe cleavage. Since traversing the triplet is a requirement for photoisomerization, its absence explains the inertness of **3** in comparison to **1**. The lack of triplet formation from the initially photoexcited singlet state suggests that the Fe complex can be added to the growing list of transition metal complexes for which the "heavy atom effect" is significantly attenuated.[99-103] An alternative, if unlikely, possibility, which we cannot discount, is that the triplet biradical is so strongly coupled to the singlet state that its lifetime is on the order of, or shorter than, that of the singlet, rendering it unobservable. The insights gained from the TRIR study, in conjunction with our improvements of synthetic methodology, point the way to the design and assembly of modified complexes that might circumvent the limitations uncovered.

Chapter 4

Spin state and metal-solvent interaction of 14-electron complex $Fe(CO)_3$ in solution

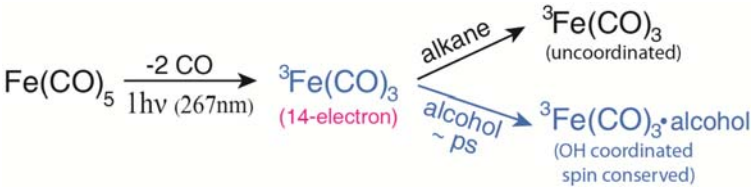

Figure 4.1. Abstract Figure of Chapter 4

This chapter is reproduced from S. C. Nguyen, J. P. Lomont, M. C. Zoerb, A. D. Hill, J. P. Schlegel, and C. B. Harris, Chemistry of the Triplet 14-Electron Complex $Fe(CO)_3$ in Solution Studied by Ultrafast Time-Resolved IR Spectroscopy, *Organometallics, 31, 3980-3984 (2012)*

4.1. Introduction

Photodissociation of ligands from 18-electron transition metal complexes leads to coordinatively unsaturated products, which often have the capacity to behave as catalysts for chemical reactions. For 16-electron photoproducts, reactivity has been shown to strongly depend on the ground spin state of the metal centers. The general understanding is that ground state singlet complexes are reactive, and also coordinate to solvent molecules as token ligands, while the ground state triplet complexes are typically inert towards solvent interactions and only bind to solvent molecules or other reactants after undergoing spin crossover to a singlet state.[23,27,28,30,33,35,104,105] For example, triplet $^3Fe(CO)_4$ interacts very weakly at best with alkanes in solution until it undergoes spin crossover to a singlet state, at which point the metal can coordinate to an alkyl group.[35,105]

The chemical reactivity of 14-electron photoproducts is still relatively unexplored, and the general expectation is that 14-electron species must be very reactive, relative to their 16-electron counterparts.[106] $Fe(CO)_3$ is an ideal candidate for a picosecond time-resolved investigation into the photochemistry of 14-electron complexes, as it can be readily generated from $Fe(CO)_5$ via a single-photon process.[59] Photoactivated $Fe(CO)_5$ is well known as a homogenous catalyst in alkene isomerization reactions, in which the photoproduct, triplet $^3Fe(CO)_3$ coordinates to an alkene, creating a key allyl hydride intermediate in the reaction mechanism.[107,108]

In a previous study, the rearrangement times of $^3Fe(CO)_4$ to form a hydroxyl-coordinated complex were measured in various alcohol solutions, and these were compared to

the rearrangement times of singlet $Cr(CO)_5$, a species also known to coordinate to alkyl groups before eventually rearranging to form a more stable hydroxyl coordinated species in the same alcohol solutions.[28,109] The differences in rearrangement kinetics were used to demonstrate that the triplet photoproduct interacts weakly at best with alkyl groups in the solvent, and that no alkyl-coordinated intermediate complexes were formed with $^3Fe(CO)_4$. Here, we use a similar approach to investigate the coordination of $^3Fe(CO)_3$ with alkyl groups, and to provide further insight to its metal-solvent interaction.

We have carried out photolysis experiments of $Fe(CO)_5$ in alcohol solutions (methanol, 1-propanol, 1-butanol, and 1-hexanol), monitoring the IR-active CO-stretching frequencies of $^3Fe(CO)_3$ and its solvent coordinated complexes to probe its rearrangement kinetics. If $^3Fe(CO)_3$ does not coordinate with alkyl groups, it it will interact minimally with the alkyl portion of the alcohol molecules, quickly rearranging to find the more strongly-coordinating hydroxyl group and forming a hydroxyl-coordinated species (**3•L2**)[110]; that is to say, $^3Fe(CO)_3$ will diffuse freely through the solution prior to encountering the hydroxyl site, and the hydroxyl-solvation kinetics of $^3Fe(CO)_3$ in alcohols of varying lengths will occur at relative rates consistent with those of other diffusion-limited processes. In contrast, if $^3Fe(CO)_3$ coordinates to alkyl groups, the hydroxyl-solvation kinetics will be slowed and the rearrangement times will increase rapidly with the number of alkyl sites present in the solvent.[28,109]

Previous studies on $Fe(CO)_3$ in *n*-heptane solution concluded that it is solvated by alkyl groups to form an alkane-coordinated complex (^{3}**3•L1**) rapidly after its formation.[35,105] In contrast, our study provides direct evidence that $^3Fe(CO)_3$ does not coordinate to alkanes. In doing so, we also prove that $^3Fe(CO)_3$ forms hydroxyl-coordinated complexes without undergoing a change of spin state. The chemistry of $^3Fe(CO)_3$ is thus distinct from that of triplet $^3Fe(CO)_4$, as it does not need to change its spin state to coordinate to a token ligand, as 16-electron species typically do.[23,27,28,30,33,35,104,105]

4.2. Sample Preparation

$Fe(CO)_5$ and all solvents were purchased from Sigma–Aldrich Co. and used without further purification. Samples of $Fe(CO)_5$ used to collect TRIR spectra were prepared at a concentration of ca. 4 mM in 150μm spacer cell, giving an absorption of ca. 1.2 OD at 2000 cm^{-1}. The solution was shielded against ambient light.

4.3. Quantum Chemical Modeling

DFT calculations are used to assist in the assignment of the chemical species observed experimentally. All calculations are performed with the Gaussian09 software package using the BP86 and B3LYP functional, 6–31+G(d,p) basis set for C, O, and H, and the LANL2DZ basis set for Fe; we have observed that this combination of density functional and basis set yields satisfactory results for organometallic species.[10,13,69] All stable structures are optimized using tight convergence criteria, and a frequency analysis is performed to ensure that optimized geometries are genuine local minima. All calculated IR frequencies are used without scaling. Calculated IR frequency values are not directly compared to IR band

positions in experiment, but they are used to determine the spin state of $Fe(CO)_3$, which can be correlated to a specific molecular symmetry and number of distinct observed CO-stretching frequencies. All calculations describe species in the gas phase. The results are given as the BP86 value with the B3LYP value in parentheses.

4.4. Result and discussion

4.4.1. Determining the spin state of hydroxyl-coordinated $Fe(CO)_3$

Figure 4.2 shows TRIR spectra of $Fe(CO)_5$ collected in room temperature 1-hexanol solution using 267-nm pump pulses; spectra in other alcohol solutions (methanol, 1-propanol, 1-butanol) are qualitatively similar and differ only in their hydroxyl solvation kinetics. We first seek to determine whether the hydroxyl solvated complex exists in a singlet or triplet state.

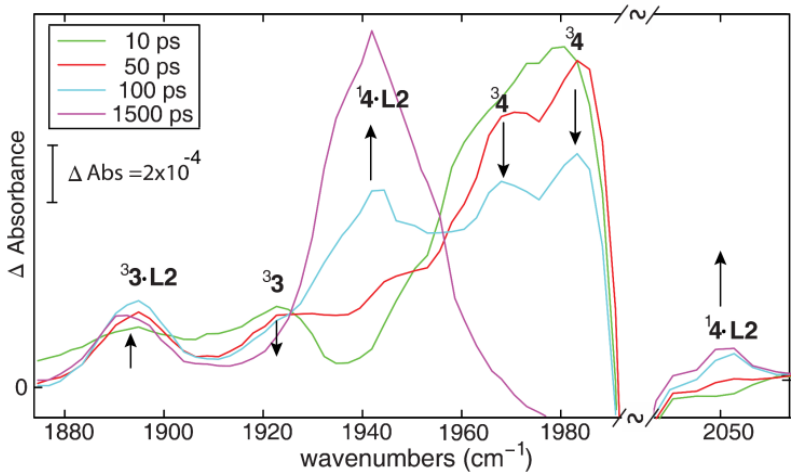

Figure 4.2. TRIR spectra of $Fe(CO)_5$ in 1-hexanol with 267-nm excitation pulses in the absorbance region corresponding to $Fe(CO)_3$ and $Fe(CO)_4$. Parent bleaches are not shown. The assignments of $^3Fe(CO)_4$ (^{3}**4**) and hydroxyl-coordinated $^1Fe(CO)_4$ (^{1}**4•L2**) are based on Ref. 28.

In the lower energy region of Figure 4.2, a broad peak at 1893 cm^{-1} rises at early times and then remains constant in intensity until 1.5 ns. The kinetics of this peak are correlated to the decay of the absorption at 1923 cm^{-1} (Figure 4.4), which has previously been assigned to alkyl-coordinated $^3Fe(CO)_3$.[35,105,111] On this basis, we assign the absorption at 1893 cm^{-1} to the hydroxyl-coordinated complex, $Fe(CO)_3$•OHC_6H_{13}, and we next look to assign its spin state. A previous molecular orbital theory approach[112], combined with DFT calculations, allows us to address this issue.

Burdett previously applied a minimum internal energy method, which predicts $Fe(CO)_3$ to exist in a triplet ground state with C_{3v} symmetry, while the molecule in a singlet state would adopt C_s symmetry.[112] Our DFT calculations confirm this to be the case for both the unsolvated and the hydroxyl solvated species. The DFT calculations show that unsolvated $Fe(CO)_3$ and the $Fe(CO)_3$ moiety in the hydroxyl-solvated complex have the same symmetry for each spin state. We also find that unsolvated $^3Fe(CO)_3$ (^{3}**3**) is more stable than

$^1Fe(CO)_3$ (**^{1}3**) by about 12(22) kcal mol^{-1} and hydroxyl-solvated $^3Fe(CO)_3$ (**^{3}3•L2**) is more stable than hydroxyl-solvated $^1Fe(CO)_3$ (**^{1}3•L2**) by 6(16) kcal mol^{-1} (see Appendix B). The hydroxyl solvated C_{3v} triplet is predicted to have a 2-fold degenerate CO-stretching absorption, while the C_s structure is predicted to have two well-resolved, strong absorptions (Table 1, Figure 4.3). Solvation by the OH group only slightly distorts the C_{3v} local symmetry of the $^3Fe(CO)_3$ moiety, resulting in a very minor separation of the degenerate frequencies (Table 1). The fact that only one absorption is experimentally (Figure 4.2) observed for the hydroxyl solvated complex, therefore, indicates that $Fe(CO)_3$•OHC_6H_{13} exists in a triplet state.

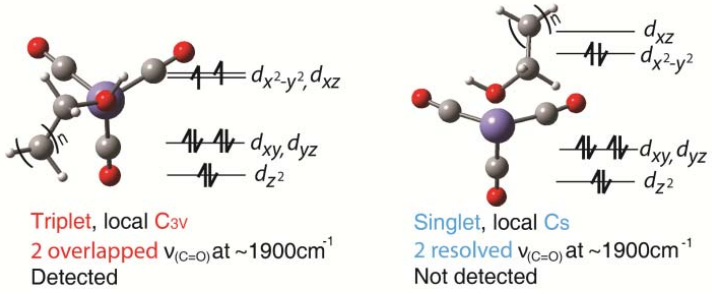

Figure 4.3. DFT calculations show different symmetries and ν(C=O) of local structure triplet $^3Fe(CO)_3$ and singlet $^1Fe(CO)_3$ coordinated to one alcohol molecule. Next to structures are d-orbital splitting schemes.[22,112]

Table 1. ν(CO) IR Frequency of $Fe(CO)_3$ Species

Complex	Exp. solvent	Exp. ν(CO) freq. (cm^{-1})		Calc. ν(CO) freq. (Intensity)[a]	Local Symmetry[a]
		our assignment	previous assignment	in cm^{-1} (km/mol)	
$^3Fe(CO)_3$ (**^{3}3**)	n-heptane	1928, 2036w[b]		2032 (98), 1953 (1203), 1953 (1205)	C_{3v}
	1-hexanol	1923[c]			
$^1Fe(CO)_3$	n-heptane	Not detected		2028(100), 1952(743), 1939(1436)	C_s
$3Fe(CO)_3$•OHC_6H_{13} (**^{3}3•L2**)	1-hexanol	1893		2004(233), 1932(1086), 1929(1078)	C_{3v}
$^1Fe(CO)_3$•OHC_6H_{13}	1-hexanol	Not detected		2007 (313), 1931(691), 1907(1312)	C_s
$^3Fe(CO)_3$•(alkane) (**^{3}3•L1**)	n-heptane	Not detected	1926[d]		
	cyclohexane		1926[e]		
$^1Fe(CO)_3$•(alkane)	n-heptane	Not detected			

[a]BP86/6–31+G(d,p) for C, O, H & LANL2DZ for Fe calculation result; [b]See Appendix B; [c]Only exist at early time; [d]Ref. 35,105; [e]Ref. 111

4.4.2. Rearrangement kinetics of triplet $^3Fe(CO)_3$ in alcohol solutions.

As mentioned earlier, the broad band at ca. 1923 cm^{-1} decreases in intensity from early times while the 1893 cm^{-1} absorption of $^3Fe(CO)_3 \bullet OHC_6H_{13}$ increases concomitantly (Figure 4.2). We observed a clear trend of conversion from the 1923 cm^{-1} absorption to the 1893 cm^{-1} absorption (Figure 4.4). We now seek to determine whether $^3Fe(CO)_3$ does, in fact, exist coordinated to alkyl groups in the solvent.

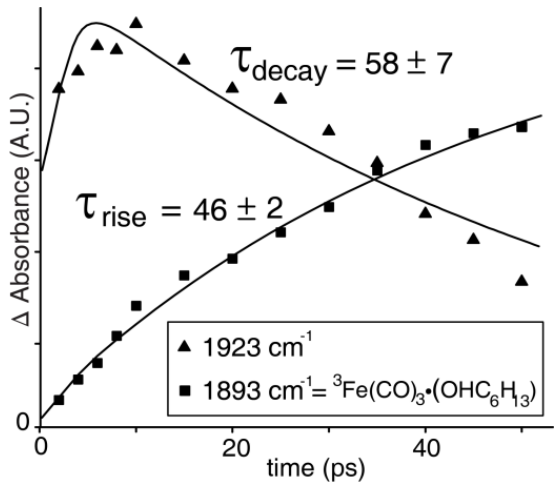

Figure 4.4. TRIR kinetic traces at 1893 and 1923 cm^{-1} in 1-hexanol solution following 267-nm photolysis. The 1893 cm^{-1} peak has a rise time constant of 46 ± 2 ps after fitting experimental points out to 200 ps. The 1923 cm^{-1} peak has a rise time constant of 2 ± 0.5 ps and a decay time constant of 58 ± 7 ps after fitting out to 50 ps, when the intensity of this peak is still strong enough to characterize with only small interference from the slow rising 1941 cm^{-1} peak.

Kinetic studies were carried out in various alcohol solvents to determine the influence of the length of the alkyl chain on the rearrangement times. Kinetic traces of the 1923 cm^{-1} in 1-bultanol, 1-propanol and methanol were quite difficult to intergrate due to its faster decay and high baseline (see an example in Appendix B). We, therefore do not use the decay time of the 1923 cm^{-1} peak to assign its structure. However, kinetic traces of hydroxyl-coordinated $^3Fe(CO)_3$ in various alcohol solvents gave clear rise time constants of 46 ± 2, 38 ± 5, 29 ± 2, and 25 ± 2 ps in 1-hexanol, 1-butanol, 1-propanol and methanol, respectively.[113,114] We compared these rise time constants in alcohol solutions with the results of two other studies to understand the nature of the rearrangement kinetics.

The first comparison is made to previous studies on the conversion of triplet $^3Fe(CO)_4$ to hydroxyl-coordinated $^1Fe(CO)_4$ in alcohol solutions. This process has been shown to be controlled by the diffusion of the metal complex through solution before encountering the hydroxyl group, since $^3Fe(CO)_4$ interacts weakly at best with the alkyl groups of the solvent. This species undergoes spin crossover to a singlet state and solvent coordination upon encountering the hydroxyl site.[28] The associated rise time constants of hydroxyl-coordinated

$^1Fe(CO)_4$ are 138, 94, and 42 ps in 1-hexanol, 1-butanol and methanol, respectively. These time constants are longer than our observed rise time constants for hydroxyl-coordinated $^3Fe(CO)_3$, but are in very reasonable agreement with the present results, considering that the total conversion process of $^3Fe(CO)_4$ is slowed by the spin-crossover, while the present case is not.

The second example, which contrasts with the present results, is a study on the rearrangement dynamics of $Cr(CO)_5$ in alcohols.[109] The rearrangement dynamics of this species are known to follow non diffusion-limited dynamics.[109] In an analogous experiment, the OH-bound $Cr(CO)_5$ complexes have rise time constants of 1800, 314 and 226 ps in 1-hexanol, 1-butanol, and 1-propanol, respectively.[28,109] These time constants are much longer than the rise time constants for hydroxyl-coordinated $^3Fe(CO)_3$. Moreover, these time constants increase rapidly with the number of alkyl groups present, which is not the case in the present study. These differences can be interpreted as follows: the hydroxyl-solvation kinetics of $Cr(CO)_5$ differ from those of $^3Fe(CO)_3$ in that $Cr(CO)_5$ interacts strongly with alkyl groups, slowing down the rearrangement process to form hydroxyl-coordinated complexes, whereas $^3Fe(CO)_3$ does not form these alkyl-coordinated intermediates, allowing it to diffuse rapidly through solution.[109]

The rise time constants of hydroxyl-coordinated $^3Fe(CO)_3$ do not depend significantly to the length of the alkyl groups in various alcohols raises the question whether the vibrational cooling of $^3Fe(CO)_3$, about 10 ps[105], prevents the coordination of solvent at early time. Thus, even the alkyl-coordinated intermediates are formed after the cooling time, they will quickly rearrange to form the hydroxyl-coordinated product due to the strong coordination of the hydroxyl group. We eliminate this possibility by comparing with the rearrangement dynamics of transient $Cr(CO)_5$ in the same alcohols[109] because the vibrational cooling do not prevent the alkyl-coordination, causing in significant large rise time constants of the hydroxyl-solvated species.

Based on these comparisons, there is strong evidence that the solvation of $^3Fe(CO)_3$ by hydroxyl groups is a diffusion-limited process, demonstrating that $^3Fe(CO)_3$ does not form alkyl-coordinated complexes. Therefore, the peak at 1923 cm^{-1} in alcohol solution (Figure 4.2) and 1928 cm^{-1} in alkane solutions (See Appendix B) should actually be assigned to unsolvated $^3Fe(CO)_3$. As we mentioned, the peak at 1928 cm^{-1} has been assigned to alkane-coordinated $^3Fe(CO)_3$ by other authors (Table 1, the previous assignment was at 1926 cm^{-1}, the reason for this difference likely comes from the resolution of the detector).[35,105,111]

4.5. Conclusion

In conclusion, we have provided experimental TRIR evidence showing that $^3Fe(CO)_3$ does not coordinate to alkanes, which is in contrast to the conclusions of previous studies.[35,105,111] Looking at previous results from the flash photolysis of $Fe(CO)_5$ in CO-saturated cyclohexane solution,[67] which show the absorption at 1926 cm^{-1} remains present at the same frequency until ca. 500 ns, we believe unsolvated $^3Fe(CO)_3$ is more thermodynamically stable in alkanes than any alkane-coordinated $^3Fe(CO)_3$.

In alcohol solutions, due to the lack of interactions with alkyl groups, $^3Fe(CO)_3$ is solvated by hydroxyl groups on the time scale of tens of picoseconds by a diffusion controlled

process. The system's spin state is conserved as the solvent molecule coordinates to the metal center. Previous studies have shown that ground state triplet 16-electron species usually undergo a change of spin state upon coordinating to a ligand,[23,27,28,30,33,35,104,105] while in this interesting case of a 14-electron species, solvation of $^3Fe(CO)_3$ does not involve a change of spin state. This result implies the subsequent intermediates of $Fe(CO)_3$ in other reactions could also involve triplet states. It is known, for example, that $^3Fe(CO)_3$•(η^2-alkene) acts as an important intermediate in the catalysis of alkene izomerization.[108] Since a substantial amount of $^3Fe(CO)_3$ is created in by single photon absorption of $Fe(CO)_5$ in solution (see Appendix B),[105] its chemistry should be considered in all reactions involving UV photolysis of $Fe(CO)_5$.

Chapter 5

Studying Heat Transfer from Photoreactions to the Solvent via Ultrafast Time-Resolved Infrared Spectroscopy of the Local Solvent

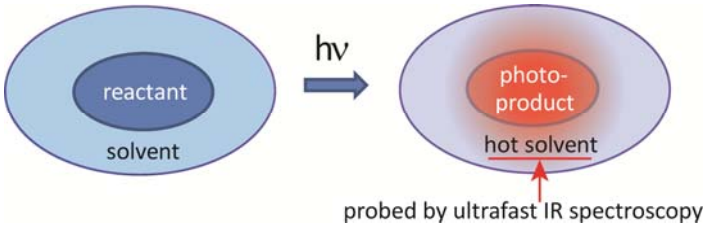

Figure 5.1. Abstract Figure of Chapter 5

5.1. Introduction

The solvent plays an essential role in modulating the transfer of energy in condensed phase chemical reactions. Probing the energy exchanged to the solvent during the course of a photochemical reaction can help us study fundamental steps of photochemical reaction dynamics. Photochemical reactions typically involve the transfer of excess heat to solvent because "hot" photoproducts possess significantly more energy than the surrounding solvent.[115-117] In this study, we demonstrate that ultrafast spectroscopy can probe the transfer of heat from both "hot" photoproducts as well as from an exothermic chemical reaction triggered photochemically. The special about this spectroscopy technique is it probes only the local solvent environment around the photoreaction to obtain information on the ultrafast dynamics of the reaction. It has potential to indirectly monitor reaction dynamics of a solute when direct spectroscopic probing of the solute is difficult or impossible.

Local heat transfer to the surrounding solvent has been demonstrated on the ultrafast time scale via time-resolved infrared (TRIR)[118], IR_{pump}-$Raman_{probe}$[119,120] and recent two dimensional IR[57] spectroscopy. In this work, ultrafast vibrational spectroscopy is used to probe the heat transfer from a photochemical reaction to the surrounding solvent. This heat transfer causes the temperature of the solvent to increase. As a result, the absorption cross sections of solvent vibrations may change due to population redistribution of the vibrational states, or due to microscopic structural changes.[57,118,121-123] Acetonitrile (MeCN) is selected as our solvent of choice for its strong absorption bands in the mid-IR region as well as the temperature sensitivity of the absorption cross section of these bands.[124,125]

To assign our spectra to the heat transfer from the photoreaction, we examined reactions in which the photoproducts possess significant excess thermal energy following completion of the photochemical reaction. These experiments include photolysis of I_2 and transition metal

complexes as well as the photoisomerization reactions of *trans*- and *cis*-stilbene (see Scheme 1). The well-known dynamics of these reactions will allow us to attribute the dynamics observed in the TRIR spectra (via the MeCN solvent) for these reactions as a result of heat transfer.

Scheme 5.1. Photochemical reactions in acetonitrile solution in this study (*)

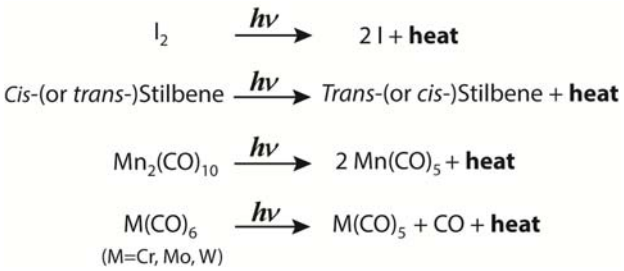

(*) The excitation energy initiating the photochemical reactions are larger than the difference in free energy between reactants and products, resulting in releasing the excess energy in form of heat to solvent.

To demonstrate that this spectroscopic technique is capable of detecting heat released not only from the hot photoproduct, but also from an exothermic chemical reaction, we also compare the response times of the solvent for these two processes. For most of the photoreactions in this study, the photoproducts are known to form within 1 ps,[126-128] and thus the dynamics observed in the TRIR spectra of MeCN solvent within the first ca. 10 ps are attributed to heat transfer from the hot photoproduct(s) to the solvent. However, the photoisomerization of *trans*-stilbene takes place on a longer timescale due to a low kinetic barrier on the excited state surface, resulting in a ca. 30 ps reaction time for this exothermic reaction,[128] and the TRIR spectra of the MeCN solvent in this study are sensitive to this slower dynamics.

5.2. Sample Preparation

All chemicals were purchased and used without further purification. Concentrations of the solutes were typically 0.01 to 0.03 M. Solutions were shielded from ambient light. All reported FTIR and TRIR spectra were recorded using 25 μm spacers. The 56 μm spacers were only used for kinetic traces when the signal/noise ratio was lower.

5.3. Results

5.3.1. Temperature dependent IR spectra of pure MeCN solution.

To understand the heat transfer from the photoreaction to the solvent in the ultrafast TRIR spectra, we first examined the variation of the IR absorptions of neat MeCN solution with respect to temperature. The spectral response of MeCN in these FTIR experiments support and facilitate our assignment of the TRIR solvent spectra to heat transfer.

MeCN has a CN-stretching absorption band at 2254 cm^{-1}, which appears asymmetric due to the existence of a hot band[129] red-shifted 5 cm^{-1} from the main absorption.[121,124,130] Another band at 2294 cm^{-1} is a symmetric combination band arising from symmetric CH_3

deformation and CC stretching.[131,132] Figure 5.2 shows FTIR difference spectra of MeCN solution in which the spectrum at room temperature has been subtracted from those collected at elevated temperatures. When increasing the solution temperature from 21°C to 50°C, the difference spectra show that the bands under investigation are slightly blue-shifted and broadened. The effect of the temperature on the spectral line shape of the CN stretching band is more evident than that of the combination band. At higher temperatures, the increased intensity on the high energy side of the CN stretching band (seen as a positive feature from 2057 to 2070 cm^{-1} in Figure 5.2b) can be explained by its blue-shift while the increased intensity at the low energy side (seen as positive feature from 2030 to 2047 cm^{-1} in Figure 5.2b) can be explained by the increased intensity of the hot band coupling to the low frequency mode, which is more highly populated at elevated temperatures.

Most importantly, the absorption cross section of these bands decreases with increasing temperature due to the redistribution of vibrational states.[121,124] This observation is consistent with observations made in the gas phase.[125] Based on the changes in intensity of these bands in Figure 5.2b, we found that the relationship between the change in absorption and the change in temperature is linear within the measured temperature regime. For example, this relationship for the maximum height of the 2294 cm^{-1} band is $\Delta OD/\Delta T = -\ 1.3 \times 10^{-3}$/°C. This linear dependence will be used to determine the temperature change for the solvent in the TRIR experiments.

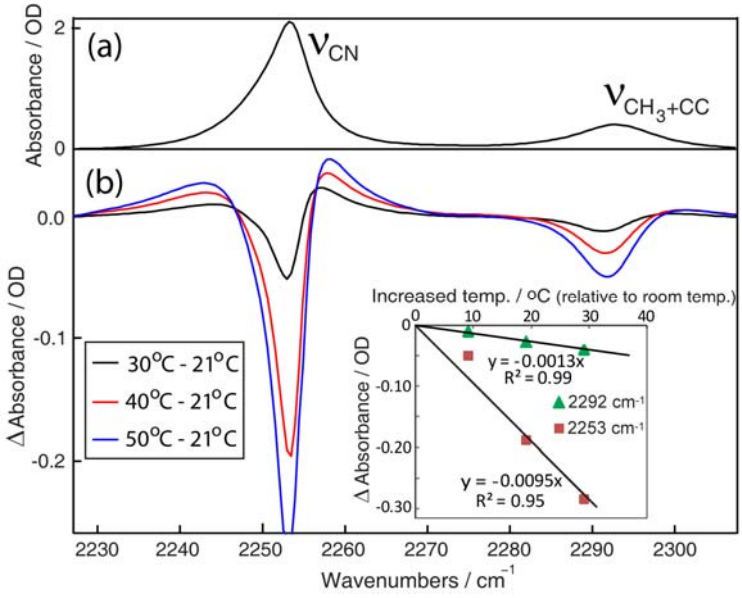

Figure 5.2. FTIR spectra of pure MeCN, (a): at 21°C, (b): difference spectra in which the spectrum at 21°C has been subtracted from those collected at higher temperatures.[133] The inset shows the linear relationship observed between the temperature change and the change in the IR absorption (the peak height at 2292 and 2253 cm^{-1}).

5.3.2. TRIR spectra of MeCN solutions during the course of photochemical reactions.

We first carried out the TRIR experiment using a solution of neat MeCN to verify that these spectra do not yield any signal following 267 or 400 nm excitation, which they do not. Thus, all of the reported signals observed in the TRIR spectra involving photochemical

reactions results from the photochemistry of the solutes studied. We selected several solutes of interest for which the solutes can be expected to possess a large amount of excess thermal energy following photoexcitation, so as to facilitate observation of temperature changes in the solvent. Note that the 267 and 400 nm excitation involve excitation energies of 107 and 71 kcal mol^{-1} respectively, while the free energy changes associated with the reactions studied are typically much smaller. In Scheme 5.1, the bond-dissociation enthalpies of I_2 and transition metal complexes are ca. 40 kcal mol^{-1},[134-139] and the enthalpy change associated with the isomerization of *cis*-to-*trans* stilbene is ca. 4 kcal mol^{-1}.[140] It noted that in addition to the heat generated via the creation of the known photoproducts, excited state relaxation and geminate recombination can and will also generate substantial thermal energy on relevant timescales. In the following subsections we will report the solvent response observed in each TRIR experiment, and in the Discussion section we will explore the information gained from the sum of our observations.

TRIR spectra of MeCN containing of I_2: Upon optical excitation, excited I_2 molecules can either relax or dissociate, and among those which dissociate, some fraction will recombine inside the solvent cage while the remaining fraction will diffuse apart into the solution.[126,141-147] Previous studies shown that the parent I_2 recovers in the solvent cage from the excited state relaxation[147] or the primary geminate recombination[148] on the timescale of ca. 1-2 ps, simultaneously dissipating its excess excitation energy to solvent in form of heat. Vibrational cooling of nascently formed I_2 takes place on the timescale of tens of picoseconds.[142] In addition, the dissociated iodine atoms out of the solvent cage also transfer their kinetic energy to the solvent. In our result, the dynamic changes in the TRIR spectra occur with a time constant of 13.5 ± 3.2 ps (see Figure 5.3), in the similar time scale of the previously known vibrational cooling of re-formed I_2. The recombination of iodine atoms outside the solvent cage happen on the μs time scale,[134] and thus this process does not affect our observation in picoseconds regime.

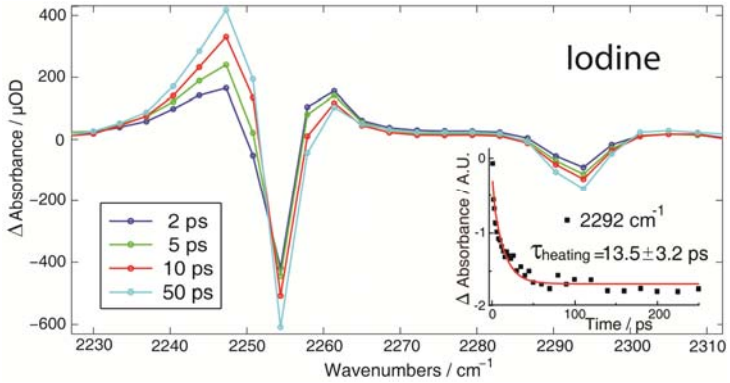

Figure 5.3. TRIR spectra of MeCN containting 0.02 M I_2 following 400 nm excitation.[149] The colored dots represent experimental data points. The inset shows the kinetic trace of the integrated intensity of combination band.

TRIR spectra of MeCN containing cis or trans-stilbene: Both the *cis*- and *trans*-stilbene isomers can undergo photoisomerization to the other form upon 267 nm excitation.[150-152] In a study on *cis*-stilbene in methanol following 295 nm excitation, the newly formed, vibrationally hot *trans*-stillbene photoproduct was observed to display a vibrational cooling

time of 17 ± 5 ps.[153] To our knowledge, we would expect the vibrational cooling of the new formed *cis*-stillbene would be on a similar time scale due the similar structure to the *trans*-isomer. In an another study under similar experimental conditions in MeCN solution to the present experiments, the isomerization of *cis*-stilbene was observed to be completed within 1 ps, while the isomerization of *trans*-stilbene proceeds via a longer-lived excited state and correspondingly exhibits a rate constant of 32 ps.[128] In our spectra, experiments involving excitation of *cis*-stilbene cause the MeCN solvent to exhibit a fast response time, closed to the vibrational cooling time. However, the excitation of *trans*-stilbene leads to a longer solvent response time, closed to the slow dynamics of the reaction, as seen in Figure 5.4. This important result will be discussed further in the Discussion section.

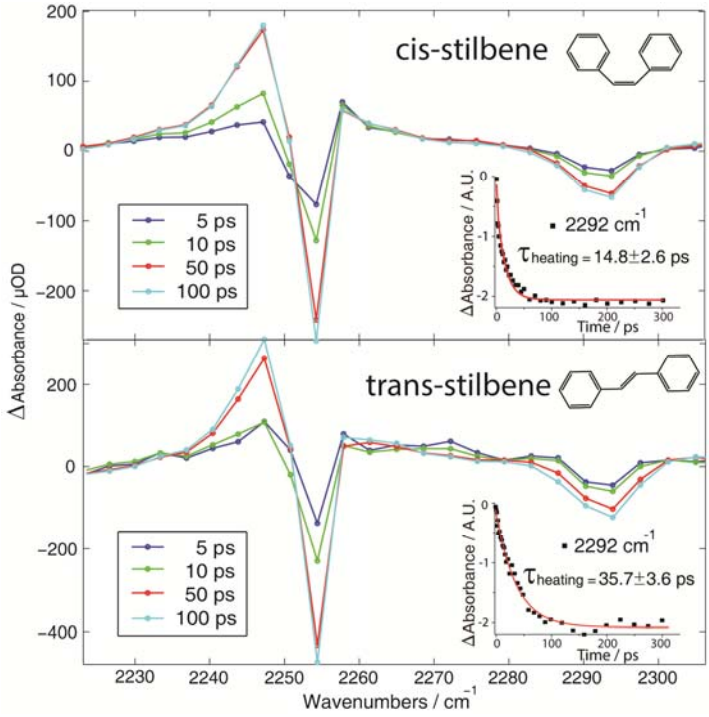

Figure 5.4. TRIR spectra of MeCN containing 0.03 M *cis*-stilbene (top) and 0.03 M *trans*-stilbene (bottom) following 267 nm excitation. The colored dots represent experimental data points. The inset shows the kinetic trace of integrated intensity of the combination band.

TRIR spectra of MeCN containing transition metal carbonyl complexes: The 267 nm excitation of Mn_2CO_{10} in MeCN solution yield $Mn(CO)_5$ as the only detectable photoproduct in our experiment.[154,155] The vibrational cooling time of $Mn(CO)_5$ in cyclohexane solution is about 40 ps.[154,156] However, this value has large error because the determination of this value, via the narrowing time of the product band, is strongly interfered by the overlapping of the parent band.[154] The 267 nm excitation of $Cr(CO)_6$, $Mo(CO)_6$ or $W(CO)_6$ in MeCN solution yields metal pentacarbonyl photoproducts, while 400 nm excitation yields no detectable photoproducts due the low absorption cross section of these species at this wavelength. In a similar study, the vibrational cooling constants of $Cr(CO)_5$, $Mo(CO)_5$ and $W(CO)_5$ were shown to be about 10 ps in hexane solution.[157]

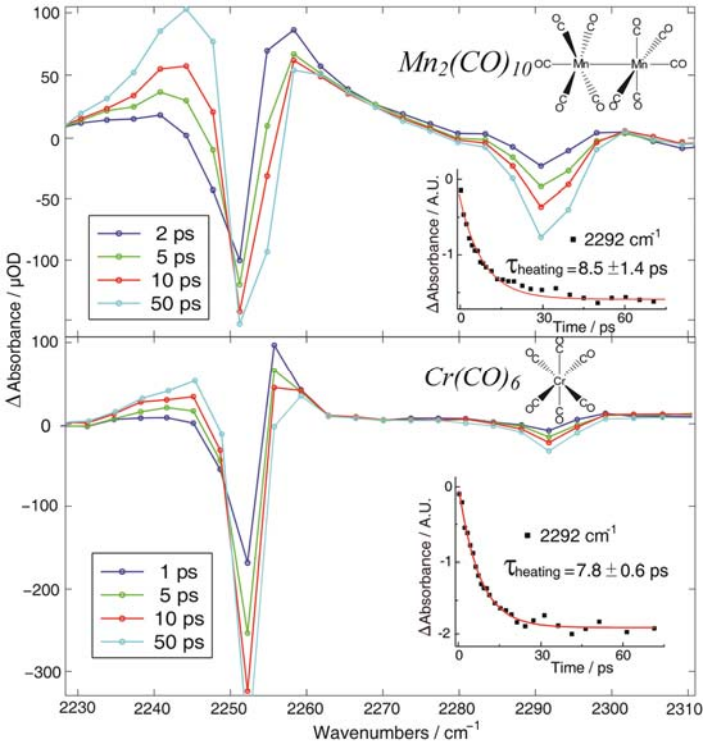

Figure 5.5. TRIR spectra of MeCN solution containing 0.01M $Mn_2(CO)_{10}$ (top) and 0.01M $Cr(CO)_6$ (bottom) following 267 nm excitation. The colored dots represent experimental data points. The inset shows the kinetic trace of integrated intensity of the combination band.

The TRIR spectra of solutions of these complexes show very similar band positions and kinetic traces for the MeCN absorptions. Figure 5.5 shows an example of the TRIR solvent spectra of $Mn_2(CO)_{10}$ and $Cr(CO)_6$ solution. The solvent response time constants for $Mn_2(CO)_{10}$, $Cr(CO)_6$, $Mo(CO)_6$, and $W(CO)_6$ solutions are 8.5 ± 1.4, 7.8 ± 0.6, 10.6 ± 0.8, and 7.9 ± 1.2 ps, respectively. Overall, the response times of the solvent are similar to the vibrational cooling time of these photoproducts. It is noted that the vibrational relaxation of the high frequency COs stretching modes of the $M(CO)_5$ (M=Cr, Mo, W) photoproducts happens in the time scale of 160 ps.[157,158] However, our spectra are not sensitive enough to observe this small energy transfer at this long time scale.

5.4. Discussion

5.4.1. Assigning the TRIR solvent spectra to the heat transfer:

Though this experimental approach is designed to study heat transfer to solvent during a photochemical reaction, there are many other processes that may also contribute to the TRIR spectra of the MeCN solvent. These processes include charge transfer,[159] changes in the dipole moment[160] of the reactant or photoproduct, vibrational energy transfer from the photoproduct to the solvent,[161,162] and finally coordination of the solvent to the photoproduct.[157,163] We will begin by discussing these possibilities in detail to systematically show that the spectral dynamics we have observed are indeed the result of heat transfer to the solvent due to a photochemical process.

A photo-induced charge transfer process, or a change in the dipole moment of the molecule after photoexcitation has been shown to cause a rapid rearrangement of the solvation shell, resulting in a detectable change of its vibrational frequency and absorption cross section.[159,160] Here, we point out that our spectral dynamics do not match those expected from rearrangement of the solvation shell. In a previous study on photoexcited LDS750 dye in MeCN, a long-lived excited state is produced, not generating much heat, but inducing a rapid change in the dipole moment relative to the ground state.[160] Consequently, the solvation shell quickly rearranges with a response time constant of 0.2 ps. In our experiment, the solvent response times take place on far too long of timescales to be caused by rearrangement of the solvation shell. Also in that study, the CN stretching vibrational frequency of the solvent is redshifted about 10 cm^{-1} when the dipole moment of the solute changes. However, in our experiment, with a wide range of dipole moment changes in various reactions, we do not see vibrational frequency shift of MeCN across these reactions. Another piece of evidence is that the TRIR spectra observed involving I_2 cannot involve a change in dipole moment, yet the TRIR spectra observed have identical band positions with those in the spectra of all of the other reactions studied. Thus we believe the contribution of solvation shell rearrangement to our TRIR spectra is negligible.

We believe that there is no direct vibrational energy transfer[164] (i.e. vibrational coupling) from the photoproduct to the 2254 and 2294 cm^{-1} bands of the solvent contributing to our TRIR results. If vibrational energy transfer from the hot photoproduct to the fundamental vibrations of the solvent at 2254 and 2294 cm^{-1} were to occur, the IR probe pulse would then cause a $v = 1 \rightarrow v = 2$ transition (along with stimulated emission of the fundamental). For the 2254 cm^{-1} band, which has a higher oscillator strength, we would expect to see a positive band for the $v = 1 \rightarrow v = 2$ transition redshifted ca. 19 cm^{-1} from the fundamental.[165] In fact, our spectra do not show clear evidence for this $v = 1 \rightarrow v = 2$ band.

Finally, solvent coordination to organometallic photoproduct could also contribute to the TRIR spectra of the solvent. However, we will explain why we also believe this contribution to be negligible in the observed TRIR spectra. In the case of $Mn_2(CO)_{10}$, it is well-known that the 17-electron $Mn(CO)_5$ photoproduct does not coordinate to a solvent molecule in picosecond scale,[32] and nor do other 17-electron photoproducts that have been studied.[32,83] Thus the spectra in Figure 5.5 (top) must not be affected by solvent coordination to the metal center. For the cases of $Cr(CO)_6$, $Mo(CO)_6$ and $W(CO)_6$, the solvent coordination time constants expected for the metal pentacarbonyl photoproducts are ca. 1-3 ps.[166,167] However, the solvent response time constants in our TRIR spectra are much longer than that value. We also found that the contribution of the CN-stretching band of photoproduct-coordinated MeCN to our TRIR spectra is expected to be quite small.[168]

Having eliminated all other reasonable potential contributions to the TRIR spectra, we can confidently attribute all of the observed spectral dynamics to heating of the solvent. There are two additional pieces of experimental evidence to strongly support this conclusion. First, each of the TRIR spectra show a similar pattern to the temperature dependent FTIR spectra in Figure 5.2b, with matching frequencies for the positive and negative bands. Note that the relative intensities between the bands in the TRIR spectra may not necessarily look identical to that observed in the temperature dependent FTIR spectra due to the lower (ca. 3 cm^{-1}) spectral resolution of the TRIR setup. Secondly, the solvent IR absorption response time

constants are about 7-15 ps, which are very close to the known vibrational cooling times of the photoproducts. During the vibrational cooling period, the photoproduct transfers its excess energy to the solvent via collisions.[115,118,161,169,170] The rate of energy transfer depends on the frequency of the collisions, the amount of energy transferred during each collision, as well as the detailed energy level structure of the solute and the solvent. As in previous studies, energy transfer may occur in form of vibrational, translational and rotational energy.[161,169,170] The sum of these energy transfer processes is responsible for local heating of the surrounding solvent, resulting in a change of its vibrational absorption cross section.

After the initial spectral dynamics due to heat transfer have ceased, the TRIR spectra do not change from 100 ps to 1.7 ns (the longest experimentally accessible delay time). This indicates that the average temperature of the solvent in the volume of the IR probed beam is constant from 100 ps to 1.7 ns.[171] It is reasonable to consider why the heat does not diffuse out of the probed area at the longer delay times studied. In fact, the thermal diffusivity χ of MeCN is 10.7 $Å^2/ps$[172] and the mean diffusion length at time t is $2(\chi t)^{1/2}$ under the ambient conditions.[118,173] For heat to diffuse only 1 μm outside of the probed area (ca.100 μm in diameter), it is expected to take about 2 μs, and thus the lack of spectral dynamics at longer delay times is to be expected.

The average temperature of the probed volume can be determined by using the linear relationship between changes in temperature and the height of peak maximum determined from the FTIR spectra (discussed in the Results section). For example, in Figure 5.5 (bottom), the absorbance change at long delay time of the 2294 cm^{-1} band is about -50 μOD, corresponding to an increase temperature of 0.038 °C. This small incremental change in average temperature indicates that thermal expansion or thermally-induced change in the refractive index of the solvent does not affect the observed spectra.[174]

It is also important to understand the temperature changes taking place immediately in the solvent surrounding the photoproduct molecule, rather than only the average temperature in the micron-size region mentioned above. To determine the local solvent rising temperature we use thermal conduction model in an infinite medium adapting the total energy transfer and heat transfer rate from the experiment (see detail in the SI).[118,173] Figure 5.6 shows the calculation for an example of the photodissociations of $Cr(CO)_6$. This temperature increase is also similar to the case in which the solutes absorb the excitation photons but follow a non-radiative relaxation to the ground state or recover from geminate recombination of photoproducts, resulting in transferring all excitation energy to heat (see Appendix C). These results show that the temperature increases for the local solvent are not very large, and are also short-lived. The temperature jumps at first few picoseconds then the heat spreads out to further distance from the photoreaction center. This result is supported by our TRIR spectra as the 2254 cm^{-1} band shows strong blue-shift (best seen in Figure 5.3, 5.5) at first few picoseconds due to the high temperature, then this band becomes more red-shifted when the temperature decreases.

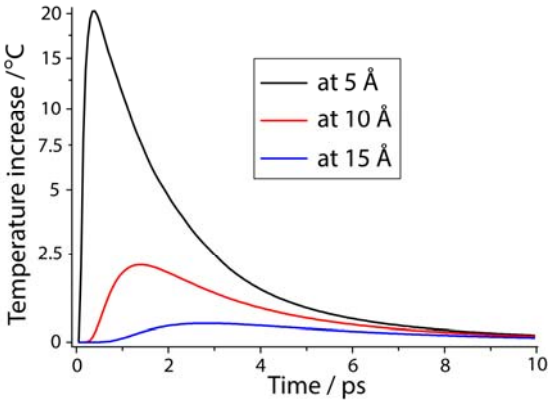

Figure 5.6. Calculated temperature increase (relative to room temperature) of local MeCN solvent at various distances from a $Cr(CO)_5$ photoproduct via thermal conduction model. (See detail calculation in the SI).

5.4.2. Prospects for following reaction dynamics:

We now discuss the fact that this method for probing heat transfer can provide us information about the dynamics of a photochemical reaction. In the case of *trans*-stilbene, as was mentioned in the Result section, the time constant for heat transfer is much longer than the values observed for all of the other reactions studied. Considering the *trans*-isomer has a similar structure to the *cis*-isomer, the vibrational cooling of its photoproduct is expected to be in about 15 ps, as observed in the UV excitation of the *cis*-isomer. Thus the slow heat transfer to solvent during the photoisomerization of *trans*-stilbene is a surprising result. Looking into the photochemical reaction dynamics from a previous study, we see that the isomerization of *trans*-stilbene is quite different from all of the other reactions studied, because the isomerization reaction takes place on a longer timescale of ca. 32 ps.[128] The reaction has a long-lived excited state due to a small barrier on potential energy surface. This long-lived excited state has vibrational cooling time in about 10 ps, then it relaxes, predominantly to reach a conical intersection, before either reacting to form the *cis*-product or to re-form the *trans*-reactant, (see Figure 5.7).[128] A very small portion of the exited state population relaxes to the ground state via fluorescence decay and can be ignored for the purposes of this study.[151,175] As a result, the heat is released from two steps: first as the hot electronically excited state of the reactant is populated, and second as the hot newly formed ground state of the product is reached, (see in Figure 5.7). All of this energy is simultaneously transferred to the solvent, resulting in a longer heat transfer time than that observed for each of the other reactions in this study. A kinetic trace of the solvent response fits well to a single exponential function with a time constant of 35.7 ± 3.6 ps, but does not fit to a bi-exponential function. Though the isomerization happens via a two-step mechanism, we are unable to resolve these dynamics with this experiment since the slow dynamics of heat transfer are comparable to the time scale of the reaction dynamics.

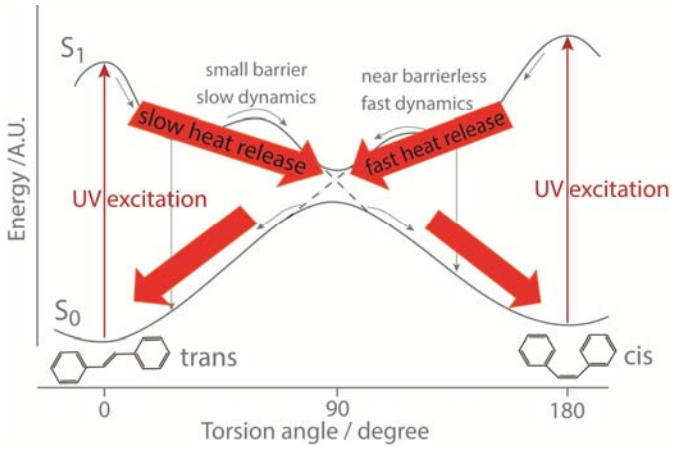

Figure 5.7. Sketch of the potential energy diagram for *trans*- and *cis*-stilbene upon UV excitation.[128,151] Barriers are exaggerated for visualization purpose. The large red arrows represent the heat released during the reaction.

This result demonstrates that TRIR spectroscopy of the solvent is sensitive to the rate of an exothermic reaction. The long time constant for heat transfer to the solvent indicates that the photoreaction must exhibit slow dynamics beyond those of vibrational cooling of the immediately formed ground state hot photoproduct or hot recovered reactant. Thus, TRIR solvent spectroscopy probes not only the cooling time of the photoproduct, but also the dynamics that occur during the course of a photochemical reaction. Probing the solvent environment to study reaction dynamics in the ultrafast regime has also been demonstrated recently via a vibrational Stark-Effect spectroscopic study on the solvation shell during a charge transfer reaction.[159] The present spectroscopic approach has the advantage of being sensitive to heat exchange between the reactant/photoproduct and the solvent, and thus it can in principle be used to detect the ultrafast dynamics involving heat exchange triggered photochemically, so long as the dynamics are not affected too strongly (i.e. occur in the same time-regime) by vibrational cooling dynamics. Since the heat does not diffuse out of the probed area within few microseconds as we calculated, this technique could be applied on timescales as long as microseconds. Longer timescales could be easily achieved by adjusting the size of probe beam relative to the pump to account for the thermal diffusion, and sample flow. As we also demonstrated, this technique is more sensitive to heat transfer than the thermal lens techniques which currently are limited to ns time resolution[176] and usually require a large amount of heat release[134,177].

There exist a few drawbacks of this approach that are worth mentioning: it cannot give structural information of the solute undergoing the photoreaction, it is limited by the fact that the reaction dynamics of interest may be temporally masked by vibrational cooling, there will be cases in which the total heat release is too small to cause a detectable TRIR signal, or there may be cases in which some competitive processes contribute to the TRIR spectra, as was discussed at the beginning of this section. Nevertheless, we feel this spetroscopic technique has the potential to observe heat tranfer from solute to solvent in cases where a direct spectroscopic study on the solute is impossible. For example, studying the dynamics of heat disscipation from nanoparticles to the solvent is not easy due to the difficulty of probing the temperature of the nanoparticales.[178,179] With this spectroscopic technique of probing the

solvent, we may hope to elucidate the ultrafast dynamics and magnitude of similar heat disscipation process.

5.5. Conclusions

We have shown that heat transfer from a photochemical reaction to MeCN solvent can be monitored via the TRIR spectra of the solvent. The time constants observed for heating of the surrounding solvent are consistent with the well-known vibrational cooling times of the photoproduct, thus confirming that the vibrational spectrum of the photoproduct is a good indication of heat transfer to solvent. During the heat transfer process, the local solvent surrounding the photoproduct is heated up to ~20°C above ambient temperature within a picosecond, then the heat dissipates quickly to the bulk solvent after few picoseconds.

The TRIR spectra of the solvent are sensitive to not only the heat dissipated by cooling of hot photoproduct, but also to heat dissipation during the course of a photochemical reaction, as demonstrated in the observed slow dynamics of *trans*-stilbene photoisomerization. We have demonstrated that this spectroscopic technique has the potential to track photochemical reaction dynamics when the reaction releases energy into the solvent. Since this technique does not require a spectroscopic probe to be present in the solute undergoing the photochemical reaction, it has the advantage of being able to potentially study photochemical reaction dynamics in which the solute cannot be directly probed.

Chapter 6

Mass Effect on Rotational Diffusion of Small Solutes in Solution

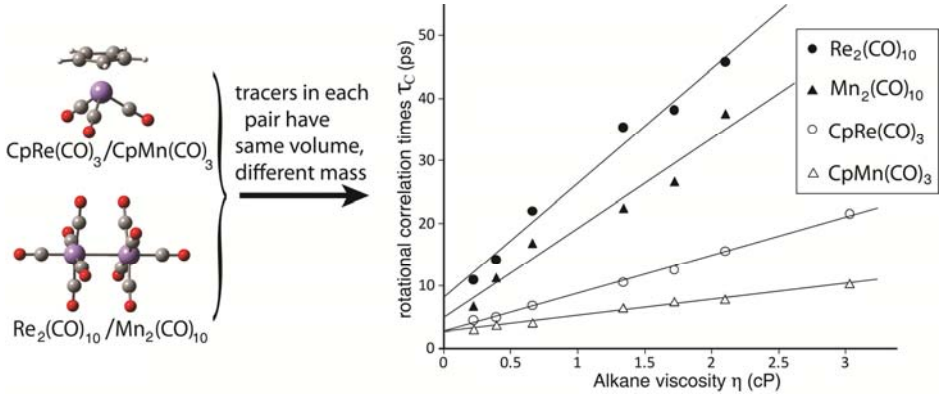

Figure 6.1. Abstract figure of chapter 6.

This chapter is reproduced from S. C. Nguyen, J. P. Lomont, C. B. Harris, Mass effect on rotational diffusion of small solutes in solution, *Chem. Phys. 422 31–36, (2013)* (a special issue in honor Professor Robin Hochstrasser)

6.1. Introduction

Understanding the rotational diffusion of solute molecules in liquids is a fundamental problem in physical chemistry. Rotational diffusion can be studied experimentally, by measuring rotational correlation times (τ_C), and theoretically, by diffusion models or molecular-dynamics (MD) simulations. Early approaches using a hydrodynamic model (the Debye-Stokes-Einstein equation, or DSE) can predict the τ_C value well when some modification factors are used.[180-182] The DSE, which describes the solvent as a continuum, has been applied successfully for very large solute molecules in dilute solution. Importantly, this equation does not include mass as a variable.

When the solute molecules are comparable in size to the solvent molecules, the hydrodynamic model is not expected to be valid. Examples demonstrating this point include the experimental τ_C values for CCl_4 and C_{60}, both in chlorobenzene-d_5, or fluorene in alcohol solvents, each of which are substantially lower than the values predicted by the DSE equation.[183,184]

Microscopic models implemented by molecular-dynamics (MD) simulations can better describe microscopic collisional effects on molecular motion.[185-187] These MD simulations show that the size and mass of solute and solvent molecules can strongly affect

their diffusive motion.[186-189] The general result is that the smaller and lighter solutes, still comparable in size and mass to the solvent molecules, have larger diffusion coefficients compared to those predicted by the DSE. The physical explanation is that their motions are more affected by collisions with solvent molecules. When the size and mass of solute molecules increase, the hydrodynamic behavior is more pronounced.

From an experimental point of view, τ_C is described successfully for many small solute systems by the following semiempirical relationship, which is written as a sum of hydrodynamic and inertial contributions: [185,190-192]

$$\tau_C = \frac{V\eta}{k_B T}\lambda\kappa + \tau_C^0 \qquad (1)$$

In equation (1), V is the effective hydrodynamic volume of the probe molecule, η is the shear viscosity of solvent, k_B is the Boltzmann constant, T is the temperature, λ is the molecular shape parameter, κ is a solute-solvent interaction parameter, and τ_C^0 is the inertial, or "free rotor," correlation time. The first component of equation (1) has the same form as the DSE equation in which κ instead presents the stick or slip boundary conditions.

While equation (1) is widely used and cited, the question remains as to whether the first component accurately describes hydrodynamic behavior, since it has similar form to the DSE (i.e. it is mass independent). Recent MD simulations actually showed a strong mass dependence for translational diffusion of small solute tracers in dilute solution.[186,187,189] While these studies focused on translational motion, the results are also applicable to rotational motion. Another question is whether τ_C^0, a "zero-viscosity" extrapolation from equation (1), can be considered an accurate "free rotor" correlation time, which is a value that is only expected in the gas phase. To answer these questions, and to further evaluate the effect of mass on diffusion of small tracers, we need to measure τ_C values under conditions that vary the molecular mass of the tracers, while keeping all other parameters constant. To our knowledge, no such experiment has been reported. In a similar spirit, translational diffusion of isotopic tracers have been studied to address the effects of mass, but the results have not always been consistent from experiment to experiment. [180,193,194] For example, Dunlop et al. and Aoyagi et al. have showed that labeled benzene derivatives in many organic solvents exhibit lower tracer diffusion coefficients for heavier isotopic substitution.[195,196] On the other hand, Harris et al. demonstrated that C_6H_5T and C_6D_5T in normal benzene or cyclohexane solution have no isotope effect on diffusion coefficient.[193]

The main obstacle of isotope tracer diffusion experiments is that the difference in mass due to isotopic substitution is small, often quite comparable to the experimental error in determining τ_C [189,193]. Therefore we introduce two pairs of solute molecules, $CpM(CO)_3$ and $M_2(CO)_{10}$ (M=Mn, Re), as perfect candidates for observing the effect of mass on the rotational diffusion of small tracers. Note that these molecules are considered small in the context of comparison to the solvent molecules. The two molecules in each pair are highly different in mass, but similar in volume, shape, and in their expected interactions with alkane solvents. The molecular mass increase when replacing Mn by Re atom in each pair of complexes is about 65%, an order of magnitude larger than our experimental error (ca. 7%). The correlation time, τ_C, is determined by ultrafast narrow-band IR pump broad-band IR probe spectroscopy, which actually gives a slice of two dimensional IR spectra (2D-IR) , a

technique that has been used successfully to determine τ_C values for small molecules in solution.[156] The effect of mass on rotational diffusion is evaluated based on the τ_C values of each pair of solutes in alkane solutions. Alkanes are chosen as solvents, since they do not interact strongly with the observed solutes and span a wide range of viscosities.

6.2. Methods

6.2.1. Sample Preparation. $CpMn(CO)_3$, $CpRe(CO)_3$ and $Re_2(CO)_{10}$ were purchased from Strem Chemicals. $Mn_2(CO)_{10}$ was purchased from Alfa Aesar. Most solvents were purchased from Sigma-Aldrich. Samples used to collect polarization anisotropy were prepared at concentrations of ca. 10-15 mM.

6.2.2. Time-dependent polarization anisotropy measurement. IR pump-probe spectroscopy is well established as a method for using polarization anisotropy measurements to determine τ_C .[156,197-199] The time-dependent polarization anisotropy of a transition dipole moment in a molecule is defined as:

$$r(t) = \frac{I_{\parallel}(t) - I_{\perp}(t)}{I_{\parallel}(t) + 2I_{\perp}(t)} \qquad (2)$$

where $I_{\parallel}(t)$ and $I_{\perp}(t)$ are the pump-probe intensity measured with parallel and perpendicular relative polarizations, respectively, and *t* is the delay time between the pump and probe pulses.

In 2D-IR spectra, the diagonal signal contains information describing the rotational and vibrational motion of a vibrational dipole moment. Assuming that the rotational motion can be separated from vibrational motion,[198] the time dependent polarization anisotropy of a dipole moment fixed in a spherical molecule, or aligned along the longest axis of a rod-like molecule, has a single-exponential form. Thus τ_C can be extracted from equation:[45,181,199]

$$r(t) = \frac{2}{5} e^{-t/\tau_C} \qquad (3)$$

The anisotropy decay of a non-degenerate IR mode gives the value of τ_C directly, while the anisotropy decay of a degenerate IR mode becomes more complicated, because the dipole moments are simultaneously excited by the polarized pulses, and their orientational relaxation does not follow equation (2).[197,200,201] For that reason, we selectively excite and monitor non-degenerate IR-active modes at 2029, 2031, 2045 and 2071 cm^{-1} for $CpMn(CO)_3$, $CpRe(CO)_3$, $Mn_2(CO)_{10}$ and $Re_2(CO)_{10}$, respectively, to measure the polarization anisotropy in each molecule. For all solutes, the center frequencies move slightly to the lower energy region with increasing length of the alkane chain. The line-widths are similar in all solvents, except for a bit of broadening in *n*-pentane (see Appendix D for the FTIR spectra). These shifts do not affect the determination of anisotropy, since the spectrograph is always moved such that the pixel with maximum intensity is aligned with the center frequency of the absorption whose kinetics is being monitored. Figure 6.2 demonstrates the monitored IR dipole moments, relative to the principal axes of inertia and molecular geometries. It is noted that the monitored IR vibrations display both intramolecular vibrational energy redistribution and population relaxation, but these modes of relaxation do not contaminate the isotropic measurement, since the vibrational contribution is be canceled out in equation (2).

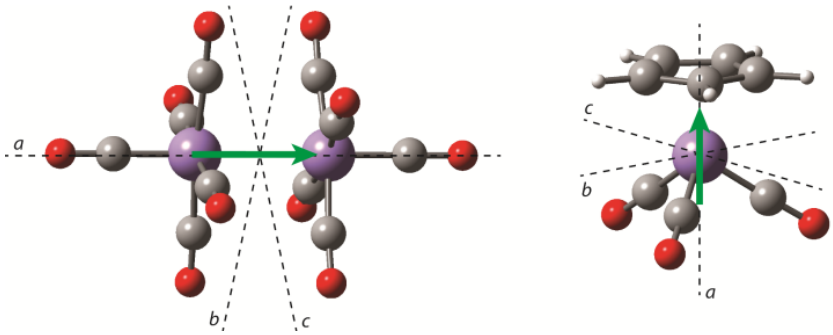

Figure 6.2. The non-degenerate IR vibrational dipole moments moments (big arrows) used to determine τ_C are along the long axis of $M_2(CO)_{10}$ molecules, or the C_3 symmetric axis of $M(CO)_3$ moieties; *a*, *b*, *c* are the principle axes of inertia.

Table 6.1. The rotational correlation times τ_C (ps) of studied solutes in several n-alkane solvents at room temperature

	pentane (η=0.22)*	Heptane (η=0.39)	Nonane (η=0.66)	dodecane (η=1.34)	tridecane (η=1.72)	tetradecane (η=2.10)	hexadecane (η=3.03)
$CpMn(CO)_3$	3.2 ± 0.2	3.7 ± 0.4	4.0 ± 0.3	6.4 ± 0.8	7.4 ± 0.6	7.8 ± 0.6	10.3 ± 1.0
$CpRe(CO)_3$	4.4 ± 0.4	5.0 ± 0.4	6.7 ± 0.5	10.5 ± 1.2	12.5 ± 1.4	15.6 ± 1.6	21.8 ± 1.6
$Mn_2(CO)_{10}$	6.7 ± 0.6	11.3 ± 0.8	16.9 ± 0.8	22.5 ± 1.6	26.7 ± 2.2	37.6 ± 2.6	
$Re_2(CO)_{10}$	11.0 ± 0.5	14.3 ± 0.4	22.0 ± 0.7	35.3 ± 1.2	38.2 ± 3.2	45.7 ± 4.0	

(*) Viscosity in cP, at room temperature. τ_C of $M_2(CO)_{10}$ in *n*-hexadecane were unable to be measured due to the fact that the rotational time constant was long relative to the vibrational life time of the vibrational mode studied [202]. All errors are reported as 95% confidence intervals.

6.2.3. Quantum Chemical Modeling. DFT calculations are used to calculate the volumes and moments of inertia of the solute molecules studied. All calculations are performed with the Gaussian09 software package using the BP86 functional, 6–31+G(d,p) basis set for C, O, and H, and the LANL2DZ basis set for transition metals; we have observed that this combination of density functional and basis set yields satisfactory results for organometallic species.[10,69] All stable structures are optimized using tight convergence criteria, ultrafine integration grid, and a frequency analysis is performed to ensure that optimized geometries are genuine local minima. Since we want to compare the relative volumes of the solutes in weakly-interacting alkane solutions, we feel that these gas phase calculations are satisfactory for our purposes.

6.3. Results

The narrow-band IR pump broad-band IR probe spectra are collected at a single IR pump frequency, centered at the absorption frequency of the peak used for determining $r(t)$. This method of collecting data is fast enough to allow us to collect τ_C values for many samples. The high frequency half of the experimental negative (v = 0->1) peak is used to calculate $r(t)$, since testing with Voigt fits showed no significant overlap of the positive (v = 1->2) peak with the high frequency half of the negative peak. The $r(t)$ plots of all compounds in all solvents are examined carefully to verify that they satisfy the conditions of equations (2) and (3). We note that $CpM(CO)_3$ (M = Mn, Re) species do not have perfectly rod-like geometries, a condition which would dictate that we could fit the $r(t)$ plots to single exponential decays.[180,181] However, the crystal structures of these species possess effective cylindrical symmetry,[203] and the experimental plot of $r(t)$ does fit very well to a single exponential decay in practice (see the $r(t)$ plots in *n*-heptane in Figure 6.3 and Appendix D). The τ_C values of all solute/solvent combinations are reported in Table 6.1. The linear regressions of τ_C vs. solvent viscosity (η) for each species are shown in Figure 6.4.

Kubarych et al. reported a τ_C value of 16 ps for $Mn_2(CO)_{10}$ in cyclohexane when monitoring the degenerate E_1 mode at 2013 cm^{-1}.[156] Knowing that monitoring degenerate modes gives smaller τ_C values than expected for non-degenerate modes,[197] our extrapolated value based on viscosity of cyclohexane is ca. 20 ps, and thus in reasonable agreement.

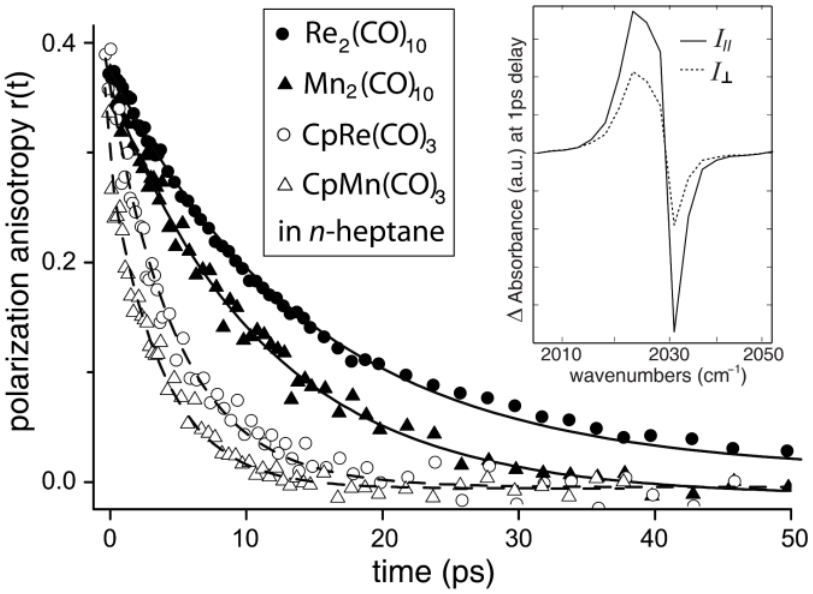

Figure 6.3. Time-dependent polarization anisotropies of $CpM(CO)_3$ and $M_2(CO)_{10}$ in n-heptane solution obtained from narrow-band IR pump broad-band IR probe spectroscopy. The inset shows example slides of 2D-IR spectra of $CpRe(CO)_3$ in *n*-heptane at 1 ps delay, IR pump frequency at 2031 cm^{-1}, 0 and 90 relative polatization. The peak volumes for calculating polarization anisotropy are integrated from 2031 to 2043 cm^{-1}.

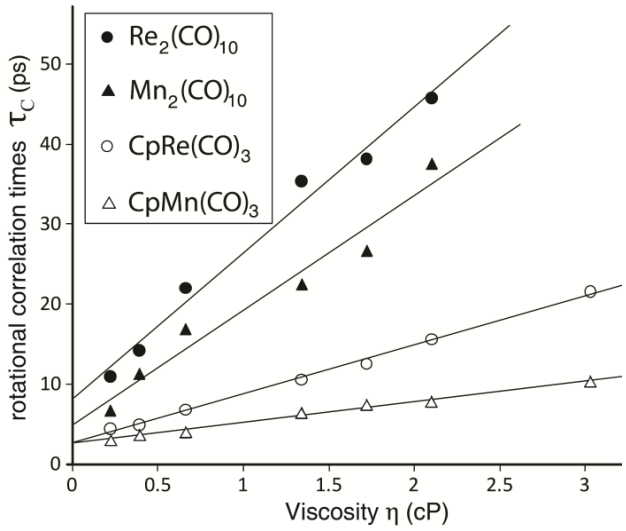

Figure 6.4. Linear dependence of rotational correlation time τ_C of $CpM(CO)_3$ and $M_2(CO)_{10}$ solutes on viscosity of alkane solutions at room temperature. Data from Table 1. The slopes and intercepts are reported in Table 2.

6.3.1. Mass effect on $CpM(CO)_3$ pair

DFT calculations indicate that $CpMn(CO)_3$ is roughly 2% larger in molecular volume than $CpRe(CO)_3$, and further comparison of their crystal structures confirms the similar volume of the two compounds.[203,204] As estimated by equation (1), the difference in τ_C values predicted from this volume difference is about 2%, which is too small to detect within our experimental error (ca. 7%). To our knowledge, it is reasonable to expect $CpMn(CO)_3$ and $CpRe(CO)_3$ to have similarly weak interactions with alkane solutions, since alkanes do not interact strongly with 18-electron complexes.[205] From DFT calculations, $CpRe(CO)_3$ has a 10% higher molecular polarizability than $CpMn(CO)_3$ (see Appendix C), which one may expect could cause stronger dipole-induced-dipole interactions with alkanes, especially in longer chain alkane solvents. To consider how this polarizability difference may affect the τ_C values, we compare our system with a more extreme case: the rotational diffusion of polar organic molecules in polar solvents. In the case of polar solutes in polar solvents, the dipole-dipole interaction causing electrostatic friction never dominates the total friction, which suggests that any differences in electrostatic friction caused by these minor differences in polarizability will be quite small in non-polar solutions. Considering the dipole-induced-dipole interaction is much weaker than the dipole-dipole interaction, we think the 10% increase in polarizability causes no significant change in the τ_C value. Thus we expect the solute-solvent interaction parameter κ in equation (1) to be the same for both complexes in the experiment. Indeed, besides the molecular mass, all other parameters that one might conventionally think to influence τ_C in are also expected to be similar for these two complexes. However, the molecular mass of $CpRe(CO)_3$ is 1.64 times greater than that of $CpMn(CO)_3$. As seen in Tables 1 and 2, $CpRe(CO)_3$ has longer τ_C than that of $CpMn(CO)_3$. We thus attribute this difference to the difference in mass between the two complexes. We note that nature of the two monitored vibrations in this pair of solutes is slightly different (see SI for a brief discussion of this point). However, we believe such differences have a minimal

effect on the τ_C values, since the rotational motion of the solutes is a diffusive process, which is not controlled by the vibrational modes.

Table 6.2. The "inverse square-root law" results for the $CpM(CO)_3$ and $M_2(CO)_{10}$ pairs, in comparison with the slope and intercept values in Figure 6.4

	$CpMn(CO)_3$	$CpRe(CO)_3$	Ratio$^{1/2}$	$Mn_2(CO)_{10}$	$Re_2(CO)_{10}$	Ratio$^{1/2}$
Mass (g/mol)	204.06	335.33	1.28	389.98	652.52	1.29
Moment of inertia(*)						
I_a /10^{-47} kg m^2	812	869	1.03	2458	2761	1.06
I_b /10^{-47} kg m^2	1016	1174	1.07	3777	5277	1.18
I_c /10^{-47} kg m^2	1019	1177	1.07	3777	5277	1.18
Linear fit of τ_C vs.η			Ratio			Ratio
Slope	2.57 ± 0.23	6.19 ± 0.37	2.41± 0.07	14.32 ± 2.94	18.26 ± 2.27	1.28 ± 0.10
Interept (τ_C^0)	2.62 ± 0.37	2.57 ± 0.59	0.98 ± 0.09	4.94 ± 3.77	8.18 ± 2.90	1.66 ± 0.68

(*) For all studies solutes, the observed IR dipole moments used to determine τ_C are along the principle axes of inertia *b* or *c* (see Figure 6.2). The moments of inertia were calculated from DFT optimized geometries.[206] All errors are reported as 95% confidence intervals.

6.3.2. Mass effect on $M_2(CO)_{10}$ pair

DFT calculations and examination of their crystal structures confirms that $Mn_2(CO)_{10}$ and $Re_2(CO)_{10}$ have the same molecular volume.[207] Similar to the $CpM(CO)_3$ pair, we expect $Mn_2(CO)_{10}$ and $Re_2(CO)_{10}$ to have the same solute-solvent interaction parameter with alkane solutions. However, the molecular mass of $Re_2(CO)_{10}$ is about 1.67 times greater than that of $Mn_2(CO)_{10}$. In Tables 6.1 and 6.2, $Re_2(CO)_{10}$ has longer τ_C values, with a larger slope and intercept for the plot in Figure 6.4 than the Mn congener. Similar to the $CpM(CO)_3$ tracers, the effect of mass on rotational diffusion is observed clearly.

Compare to "inverse square-root law"

A classical approach to the rotational motion of isotopic molecules predicts that the ratio of the rotational diffusion coefficient of the heavier isotope to that of the lighter isotope is equal to the square root of the inverse ratio of their moments of inertia:[82]

$$D_{rot}(\text{heavy})/D_{rot}(\text{light}) = (I(\text{light})/I(\text{heavy}))^{1/2}$$

For diffusional motion of a dipole moment fixed in a spherical molecule, or aligned along the longest axis of a rod-like molecule, the predicted rotational correlation time is given as:

$$D_{rot} = 1/6\tau_{rot}$$

Thus,

$$\tau_{rot}(\text{heavy})/\tau_{rot}(\text{light}) = (I(\text{heavy})/I(\text{light}))^{1/2} \quad (4)$$

This is commonly termed "the square root of moment of inertial law". We, therefore, want to compare the ratio of the slope and intercept of τ_C vs. η plot to ratios predicted by this inverse square-root law to understand the nature of the rotational diffusion (see Table 6.2).

6.4. Discussion

From Figure 6.4, we can see that the rotational correlation times of each solute depend linearly on viscosity, coinciding with the linear behavior predicted by equation (1), despite the fact that the structure, volume, and mass of the solvent molecules differ moving from *n*-pentane to *n*-hexadecane solvent. The linear regression for the $M_2(CO)_{10}$ pairs show more variation due to the fact that the values of τ_C are comparable to the vibrational lifetimes of these species (see Appendix D). All observed τ_C values increase proportionally to viscosity, consistent with reorientation of the solute molecules by a diffusive process.[208] In examining the effects of mass on rotational diffusion, we can neglect effects due to changes in V, T, λ and κ, since these are all essentially constants between each pair of molecules in our experiment. For both pairs of solutes, the heavier congeners have longer τ_C values, clearly indicating slower rotational diffusion. We now discuss the effect of solute mass on the first and second terms of equation (1), based on the slope and intercept values reported in Table 2.

The second term of equation (1), τ_C^0 , which is the intercept of the τ_C vs. η plot, has been suggested to provide the inertial contribution of the solute to τ_C .[190] As seen in Figure 6.4 and Table 2, the contribution of this term is significant. To quantitatively evaluate the mass effect in this inertial contribution, we compare our experimental results with the value predicted by the ''square root of moment of inertia law"[82]. For the $CpM(CO)_3$ tracers, the moments of inertia do not change much when replacing Mn by Re, because the metals are located very close to the center of mass for these molecules. [209] The calculated time constant ratio from the "square root of moment of inertia law" predicts an increase of 1.07 times for the heavier isotopic substitution. However, the experimental intercepts are unchanged for both complexes. Knowing that the calculated moments of inertia are from DFT calculated structures in the gas phase, and that our experimental error is ca. 7%, it is understandable that we are incapable of seeing the difference in the two intercepts if it does exist. In the case of the $M_2(CO)_{10}$ compounds, when replacing Mn by Re, the moments of inertia change strongly due to the molecular symmetry and to the distance between the two metal atoms. The calculated time constant ratio from the inverse square-root law increases about 1.18 times for the heavier congener, while the experimental intercept ratio is 1.66 ± 0.68. Knowing that any outlying data points could affect of the linear regression, and thus the intercept ratio (see Figure 6.4), we also performed the linear regressions using only the first five and last five experimental data points for each solute, which gave intercept ratios of 1.28 ± 0.10 and 1.51 ± 0.67, respectively. Clearly, these are similar to the values obtained when using all data points, which is reassuring. The two results from the two pairs of solutes support the interpretation of the intercept as a description of the inertial effect on rotational diffusion. However, for the $M_2(CO)_{10}$ pair, the intercept ratio is larger than the ratio expected from the inverse square-root law, suggesting that the τ_C^0 value may not entirely provide an accurate "free rotor correlation time" of these small molecules. Since τ_C^0 and the inverse square-root law are rough approximations, comparing them will not allow us completely understand the

real dynamics of the system. We hope that MD simulations may be able to shed light on this phenomenon.

Looking back to the semiempirical description in equation (1), the first term is understood to provide the hydrodynamic contribution (i.e. mass independent behavior). In contrast, though all parameters in this term are essentially constant in our experiments, our results give larger τ_C values for heavier isotopic substitutions, showing a clear trend of mass dependence for this term. The trend is stronger for the $CpM(CO)_3$ pair, which are smaller and lighter than the $M_2(CO)_{10}$ pair. This trend is supported by MD simulations, which suggest that when the size of the solute molecules increases relative to the size of solvent molecules, the hydrodynamic regime is more appropriate [186]. In the range of mass ratios and volume ratios of solute to solvent molecules in our experiment, the MD simulations also showed a mass effect on the tracer diffusion coefficient of translational motion, supporting the present result.[186-189] In the results involving $CpM(CO)_3$ tracers, we emphasize that even though there is a not a significant change in moments of inertia between the Mn and Re congeners, the heavier solutes undergo significantly slower rotational diffusion. This result is similar to the results of many MD simulations in which the mass of the particle, but not its moment of inertia, was increased.[186,189,193] This result is also distinct from other isotope tracer experiments for benzene, water, ammonia, ect., which cause relatively large changes in moments of inertia, with relatively small changes in the overall mass of the tracers. Since the effect of mass is only included in the first component of equation (1), which is also dependent on solvent viscosity, translational motion could interfere with rotational motion. MD simulations demonstrate the coupling of translational and rotational diffusional motion of small tracers diffusion[187] or self-diffusion[188,210]. This coupling appears in any molecules that possess non-spherical shapes, since collisions change the angular momenta of these molecules.[210] The large increase in molecular mass of $CpRe(CO)_3$ causes a significantly smaller translational diffusion coefficient, meaning that translation-rotation coupling would result in a smaller rotational diffusion coefficient (i.e. larger τ_C) as measured in the experiment. Thus translation-rotation coupling could at least partially explain the larger slope of the τ_C vs. η plot for $CpRe(CO)_3$, even though its moment of inertia does not change much from that of $CpMn(CO)_3$. In case of $M_2(CO)_{10}$ complexes, the translation-rotation coupling could also contribute to the larger slope for $Re_2(CO)_{10}$.

In both pairs of solutes, we observed a mass dependence of rotational diffusion, indicating non-hydrodynamic behavior for the rotational motion of small molecules. Even though the hydrodynamic description does not appear to hold, it is interesting that we still observe a linear dependence of τ_C on solvent viscosity. When heavier substitutions change the moment of inertia of the solute, the effect of mass on rotational diffusion can be observed via a larger intercept and slope in the plot in Figure 6.4; but even when the moments of inertia do not change, the mass effect can still be observed in the larger slope, possibly due to translation-rotation coupling.

6.5. Conclusions

A microscopic description of rotational diffusion is necessary to better understand the nature of rotational motion in solution. The effects of parameters including molecular volume, molecular shape, and solute-solvent interactions, on rotational dynamics of solute tracers in

dilute solution have been studied over 30 years. However, the effect of the molecular mass of the solute on its rotational diffusion still needs further exploration. Here we show this result to be an important parameter in developing an accurate microscopic description. Measuring the rotational correlation times, τ_C, of two pairs of solute molecules, $CpMn(CO)_3$/$CpRe(CO)_3$, and $Mn_2(CO)_{10}$/$Re_2(CO)_{10}$, allows us to clearly observe the effect of mass on rotational diffusion in solution, indicating non-hydrodynamic behavior. The effect of mass is that heavier substitution is observed to cause significantly slower rotational diffusion. In the case of $CpMn(CO)_3$/$CpRe(CO)_3$, even when the heavier substitution does not change the moment of inertia of the solute, the effect of mass can be observed via a larger slope in τ_C vs. viscosity plot, possibly due to translation-rotation coupling. For $Mn_2(CO)_{10}$/$Re_2(CO)_{10}$, in which the moment of inertia of the solute changes significantly, the effect of mass can be seen in both the larger slope and intercept. These results also indicate an inertial contribution of the solute to rotational diffusion. We present these results as experimental evidence for a mass dependence of rotational diffusion of tracer molecules in solution, which should resolve some ambiguity in previous isotope labeling experiments. We feel this is an important step toward developing a better model for describing the dynamics of small molecules in solution.

Chapter 7
Conclusions

A complete understanding of the fundamental steps of chemical reaction is important to find the optimized condition for the known reactions as well as design the new reactions. Time resolved IR spectroscopy has been applied to study reaction dynamics of organometallic complexes for over 50 years. Many reactions have been studied in great detail on their dynamics and mechanisms. Still, there are many remained unknown dynamics of these complexes. The most interesting chemistry of transition metal organometallic complexes, especially under photo-excitation and dissociation, is their non-adiabatic reaction dynamics, involving multiple potential energy surfaces having different electronic states. The work in this thesis provide insight to dynamics of some prototype complexes in solution.

In particular to the study on photoreaction of $FvRu_2(CO)_4$ and $FvFe_2(CO)_4$, the former undergoes photoisomerization, but the later does not (chapter 3). The direct conclusion from the TRIR spectroscopy is the former has the long-lived triplet intermediate that supporting the isomerization while the later does not have the long-lived triplet intermediate. Both these complexes photochemically generate singlet intermediates but these intermediates relax quickly to the parent molecules, resulting in no net reaction. In combination of this result with other work that I have been participating in the Harris' group, we can draw two general conclusions from this study. Firstly, these complexes have the same d-configuration for the metals but their chemical reactivities depend strongly on the identity of each metal. Secondly, the spin state of intermediate photoproduct plays the decision role in making the photoisomerization possible. In regard to the first conclusion, recent studies on many other organometallic complexes have shown that the identity of the metals (in the same group of the periodic table) dictates the reactivities of these complexes.[27,32,211] These results and my result in this thesis indicate that the thumb rule for chemical reactivity depending on the valence electrons is not always corrected. Instead, the nature of the whole electronic structure of the metal and the ligands defines the reactivity. With regard to the second conclusion, the triplet state has the repulsion on the potential energy surface that supports the Cp-Cp rotation of the fulvalene structure, making the photoisomerization possible. Among of many fulvalene dimetal complexes, only the Ru-based complexes can undergo photoisomerization while the other metal-based complexes (Fe, Mo and W) do not. Further study should provide more insight to why only Ru-based complexes has the long-lived triplet intermediates after photoexcitation. Along with this result, the relationship between the spin states and the reactivities has been seen more evidently in many other complexes recently.[27,28,212]

For the first time, we study the chemistry of the 14-electron intermediate, showing that its chemistry is different from the 16-electron intermediate even though they have the same spin state. For example, the 16-electron ground state triplet $^3Fe(CO)_4$ photoproduct must convert to the singlet state to coordinate to a solvent molecule. Interestingly, our study on the chemistry of 14-electron ground state triplet $^3Fe(CO)_3$ photoproduct shows that the complex does not change spin state upon coordinating to solvent (chapter 4), showing a different

chemistry from the triplet 16-electron $^3Fe(CO)_4$. Thus, the total electron count at the metal center may need to be considered beside the spin state to account for the chemistry of organometallic complex.

Another aspect of reaction dynamics in solution is the heat exchange with solvent. In chapter 5, we showed that probing the IR frequency of the solvent can tell us the temperature of the local solvent around the reaction during the heat exchange time. The spectra of the solvent are capable to detect not only the cooling time of a hot photoproduct, but also the dynamics of photochemical reaction as demonstrated in the *trans*-stilbene photoisomerization reaction. Probing the solvent environment to know the reaction dynamics has been demonstrated via a vibrational Stark-Effect spectroscopic study on the solvation shell during a charge transfer reaction.[159] Our result adds an alternative method into this research direction. The notable potential of this method is it is able to study photochemical reaction dynamics in which the solute cannot be directly probed and it can apply to study reaction in various solvents. We currently expand the application of this technique to nanomaterial research, in which we study the heat transfer dynamics from nanoparticles to water.

In the last chapter (chapter 6), we investigated how molecular mass of a solute effect on its rotational diffusion in solution. In the controlled experiment having the molecular mass of solute increase but keeping the moment of inertia unchanged, the heavier solute has significant slower rotational diffusion. This result shows that the rotational motion of molecules in solution does not simply depend on their moment of inertia. In fact, the translational collisions between the solute and solvent cause change in their angular momentum, driving the rotational diffusion (known as translation-rotation coupling). The heavier molecule has significant slower translation and thus causes slower rotational diffusion due to this translation-rotation coupling. This result gives more insight to the molecular dynamic in the solution, especially the large amplitude motion.

Overall, the chemistry of organometallic complexes has long history development due to their highly tunable property of structure and chemical reactivity. Time-resolved IR spectroscopy has been proved as a very powerful tool to study reaction dynamics of organometallic complexes. Future affordable commercial laser with high power and stability in combination with new design of IR generation source and data acquisition will give great improvement in time resolution, probed frequency range and low limit detection. Those improvements will drive more explorations in the field of ultrafast dynamics study in future.

References

(1) "The Nobel Prize in Chemistry 1986". Nobelprize.org. Nobel Media AB 2013.

(2) "The Nobel Prize in Chemistry 1999". Nobelprize.org. Nobel Media AB 2013.

(3) Garand, E.; Zhou, J.; Manolopoulos, D. E.; Alexander, M. H.; Neumark, D. M. *Science* **2008**, *319*, 72.

(4) Worner, H. J.; Bertrand, J. B.; Kartashov, D. V.; Corkum, P. B.; Villeneuve, D. M. *Nature* **2010**, *466*, 604.

(5) Wörner, H. J.; Bertrand, J. B.; Fabre, B.; Higuet, J.; Ruf, H.; Dubrouil, A.; Patchkovskii, S.; Spanner, M.; Mairesse, Y.; Blanchet, V.; Mével, E.; Constant, E.; Corkum, P. B.; Villeneuve, D. M. *Science* **2011**, *334*, 208.

(6) Voth, G. A.; Hochstrasser, R. M. *The Journal of Physical Chemistry* **1996**, *100*, 13034.

(7) Fayer, M. D. *Annual Review of Physical Chemistry* **2009**, *60*, 21.

(8) Roberts, S. T.; Ramasesha, K.; Tokmakoff, A. *Accounts of Chemical Research* **2009**, *42*, 1239.

(9) Kolano, C.; Helbing, J.; Kozinski, M.; Sander, W.; Hamm, P. *Nature* **2006**, *444*, 469.

(10) Cahoon, J. F.; Sawyer, K. R.; Schlegel, J. P.; Harris, C. B. *Science* **2008**, *319*, 1820.

(11) Kim, Y. S.; Hochstrasser, R. M. *The Journal of Physical Chemistry B* **2009**, *113*, 8231.

(12) Bromberg, S. E.; Yang, H.; Asplund, M. C.; Lian, T.; McNamara, B. K.; Kotz, K. T.; Yeston, J. S.; Wilkens, M.; Frei, H.; Bergman, R. G.; Harris, C. B. *Science* **1997**, *278*, 260.

(13) Sawyer, K. R.; Cahoon, J. F.; Shanoski, J. E.; Glascoe, E. A.; Kling, M. F.; Schlegel, J. P.; Zoerb, M. C.; Hapke, M.; Hartwig, J. F.; Webster, C. E.; Harris, C. B. *Journal of the American Chemical Society* **2010**, *132*, 1848.

(14) Calladine, J. A.; Duckett, S. B.; George, M. W.; Matthews, S. L.; Perutz, R. N.; Torres, O.; Vuong, K. Q. *Journal of the American Chemical Society* **2011**, *133*, 2303.

(15) To, T. T.; Heilweil, E. J.; Duke, C. B.; Ruddick, K. R.; Webster, C. E.; Burkey, T. J. *The Journal of Physical Chemistry A* **2009**, *113*, 2666.

(16) Ito, T.; Hamaguchi, T.; Nagino, H.; Yamaguchi, T.; Washington, J.; Kubiak, C. P. *Science* **1997**, *277*, 660.

(17) Mulder, D. W.; Ratzloff, M. W.; Shepard, E. M.; Byer, A. S.; Noone, S. M.; Peters, J. W.; Broderick, J. B.; King, P. W. *Journal of the American Chemical Society* **2013**, *135*, 6921.

(18) Cahoon, J. F.; Kling, M. F.; Sawyer, K. R.; Frei, H.; Harris, C. B. *Journal of the American Chemical Society* **2006**, *128*, 3152.

(19) Martyn Poliakoff, J. J. T. *Angewandte Chemie International Edition* **2001**, *40*, 2809.

(20) Trushin, S. A.; Kosma, K.; FuÃŸ, W.; Schmid, W. E. *Chemical Physics* **2008**, *347*, 309.

(21) Fernández, I.; Cossío, F. P.; Sierra, M. A. *Accounts of Chemical Research* **2011**, *44*, 479.

(22) Leadbeater, N. *Coordination Chemistry Reviews* **1999**, *188*, 35.

(23) Bengali, A. A.; Bergman, R. G.; Moore, C. B. *Journal of the American Chemical Society* **1995**, *117*, 3879.

(24) G. L. Geoffroy and M. S. Wrighton, O. P.; *Organometallic Photochemistry,* Academic, N. Y., 1979.

(25) Jordan, R. B. *Reaction Mechanisms of Inorganic and Organometallic Systems, Oxford University Press,* **2007**.

(26) Yang, H.; Kotz, K. T.; Asplund, M. C.; Wilkens, M. J.; Harris, C. B. *Accounts of Chemical Research* **1999**, *32*, 551.

(27) Snee, P. T.; Payne, C. K.; Kotz, K. T.; Yang, H.; Harris, C. B. *Journal of the American Chemical Society* **2001**, *123*, 2255.

(28) Snee, P. T.; Payne, C. K.; Mebane, S. D.; Kotz, K. T.; Harris, C. B. *Journal of the American Chemical Society* **2001**, *123*, 6909.

(29) Lomont, J. P.; Nguyen, S. C.; Harris, C. B. *Organometallics* **2012**, *31*, 4031.

(30) Lomont, J. P.; Nguyen, S. C.; Schlegel, J. P.; Zoerb, M. C.; Hill, A. D.; Harris, C. B. *Journal of the American Chemical Society* **2012**, *134*, 3120.

(31) Nguyen, S. C.; Lomont, J. P.; Zoerb, M. C.; Hill, A. D.; Schlegel, J. P.; Harris, C. B. *Organometallics* **2012**, *31*, 3980.

(32) Lomont, J. P.; Nguyen, S. C.; Harris, C. B. *The Journal of Physical Chemistry A* **2013**, *117*, 3777.

(33) CarreÃn-Macedo, J.-L.; Harvey, J. N. *Journal of the American Chemical Society* **2004**, *126*, 5789.

(34) Harvey, J. N. *Physical Chemistry Chemical Physics* **2007**, *9*, 331.

(35) Besora, M.; CarreoÌn-Macedo, J.-L.; Cowan, A. J.; George, M. W.; Harvey, J. N.; Portius, P.; Ronayne, K. L.; Sun, X.-Z.; Towrie, M. *Journal of the American Chemical Society* **2009**, *131*, 3583.

(36) Golonzka, O.; Khalil, M.; Demirdoven, N.; Tokmakoff, A. *J. Chem. Phys.* **2001**, *115*, 10814.

(37) Khalil, M.; Demirdoven, N.; Tokmakoff, A. *J. Phys. Chem. A* **2003**, *107*, 5258.

(38) Baiz, C. R.; McRobbie, P. L.; Anna, J. M.; Geva, E.; Kubarych, K. J. *Accounts of Chemical Research* **2009**, *42*, 1395.

(39) Anna, J. M.; King, J. T.; Kubarych, K. J. *Inorganic Chemistry* **2011**, *50*, 9273.

(40) Nguyen, S. C.; Lomont, J. P.; Harris, C. B. *Chemical Physics* **2013**, *422*, 31.

(41) Sawyer, K., One- and two-dimensional infrared spectroscopic studies of solution-phase homogeneous catalysis and spin-forbidden reactions, PhD thesis, University of California at Berkeley, 2008.

(42) Harpham, M. R.; Nguyen, S. C.; Hou, Z.; Grossman, J. C.; Harris, C. B.; Mara, M. W.; Stickrath, A. B.; Kanai, Y.; Kolpak, A. M.; Lee, D.; Liu, D.-J.; Lomont, J. P.; Moth-Poulsen, K.; Vinokurov, N.; Chen, L. X.; Vollhardt, K. P. C. *Angewandte Chemie-International Edition* **2012**, *51*, 7692.

(43) Hamm, P.; Kaindl, R. A.; Stenger, J. *Opt. Lett.* **2000**, *25*, 1798.

(44) Hamm, W. *Journal of Physics: Condensed Matter* **2002**, R1035.

(45) Hamm, P.; Zanni, M. T. *Concepts and Methods of 2D Infrared Spectroscopy,* **2011**, Cambridge University Press.

(46) Mukamel, S. *Annual Review of Physical Chemistry* **2000**, *51*, 691.

(47) Borek, J.; Perakis, F.; Kläsi, F.; Garrett-Roe, S.; Hamm, P. *The Journal of Chemical Physics* **2012**, *136*.

(48) Park, S.; Fayer, M. D. *Proceedings of the National Academy of Sciences* **2007**, *104*, 16731.

(49) Singh, P. K.; Kuroda, D. G.; Hochstrasser, R. M. *The Journal of Physical Chemistry B* **2013**, *117*, 9775.

(50) Hill, A. D.; Zoerb, M. C.; Nguyen, S. C.; Lomont, J. P.; Bowring, M. A.; Harris, C. B. *The Journal of Physical Chemistry B* **2013**, *117*, 15346.

(51) Peng, C. S.; Tokmakoff, A. *The Journal of Physical Chemistry Letters* **2012**, *3*, 3302.

(52) Middleton, C. T.; Marek, P.; Cao, P.; Chiu, C.-c.; Singh, S.; Woys, A. M.; de Pablo, J. J.; Raleigh, D. P.; Zanni, M. T. *Nat Chem* **2012**, *4*, 355.

(53) Cho, M. *Chem. Rev.* **2008**, *108*, 1331.

(54) Buchli, B.; Waldauer, S. A.; Walser, R.; Donten, M. L.; Pfister, R.; Blöchliger, N.; Steiner, S.; Caflisch, A.; Zerbe, O.; Hamm, P. *Proceedings of the National Academy of Sciences* **2013**, *110*, 11725.

(55) Lessing, J.; Roy, S.; Reppert, M.; Baer, M.; Marx, D.; Jansen, T. L. C.; Knoester, J.; Tokmakoff, A. *Journal of the American Chemical Society* **2012**, *134*, 5032.

(56) Rubtsova, N. I.; Rubtsov, I. V. *Chemical Physics* **2013**, *422*, 16.

(57) Son, H.; Park, K.-H.; Kwak, K.-W.; Park, S.; Cho, M. *Chemical Physics* **2013**, *422*, 37.

(58) Hamm, P. *Annu. Rev. Phys. Chem.* **2008**, *2008. 59:291-317*.

(59) Maekawa, H.; Sul, S.; Ge, N.-H. *Chemical Physics* **2013**, *422*, 22.

(60) Ji, M.; Odelius, M.; Gaffney, K. J. *Science* **2010**, *328*, 1003.

(61) Bakker, H. J.; Skinner, J. L. *Chem. Rev.* **2009**, *110*, 1498.

(62) Cahoon, J. Investigation of Organometallic Reaction Mechanisms with One and Two Dimensional Vibrational Spectroscopy, PhD thesis, University of California at Berkeley, 2008

(63) Zoerb, M. C. Dynamic IR Peak Coalescence and Ultrafast Chemical Exchange Reactions Studied by Two Dimensional Infrared Spectroscopy, PhD thesis, University of California at Berkeley, 2012.

(64) Gaussian 09, Revision D.01, Frisch, M. J.; Trucks, G. W.; Schlegel, H. B.; Scuseria, G. E.; Robb, M. A.; Cheeseman, J. R.; Scalmani, G.; Barone, V.; Mennucci, B.; Petersson, G. A.; Nakatsuji, H.; Caricato, M.; Li, X.; Hratchian, H. P.; Izmaylov, A. F.; Bloino, J.; Zheng, G.; Sonnenberg, J. L.; Hada, M.; Ehara, M.; Toyota, K.; Fukuda, R.; Hasegawa, J.; Ishida, M.; Nakajima, T.; Honda, Y.; Kitao, O.; Nakai, H.; Vreven, T.; Montgomery, J. A., Jr.; Peralta, J. E.; Ogliaro, F.; Bearpark, M.; Heyd, J. J.; Brothers, E.; Kudin, K. N.; Staroverov, V. N.; Kobayashi, R.; Normand, J.; Raghavachari, K.; Rendell, A.; Burant, J. C.; Iyengar, S. S.; Tomasi, J.; Cossi, M.; Rega, N.; Millam, N. J.; Klene, M.; Knox, J. E.; Cross, J. B.; Bakken, V.; Adamo, C.; Jaramillo, J.; Gomperts, R.; Stratmann, R. E.; Yazyev, O.; Austin, A. J.; Cammi, R.; Pomelli, C.; Ochterski, J. W.; Martin, R. L.;

Morokuma, K.; Zakrzewski, V. G.; Voth, G. A.; Salvador, P.; Dannenberg, J. J.; Dapprich, S.; Daniels, A. D.; Farkas, Ö.; Foresman, J. B.; Ortiz, J. V.; Cioslowski, J.; Fox, D. J. Gaussian, Inc., Wallingford CT, 2009.

(65) Becke, A. D. *Physical Review A* **1988**, *38*, 3098.

(66) Lee, C.; Yang, W.; Parr, R. G. *Physical Review B* **1988**, *37*, 785.

(67) Hay, P. J.; Wadt, W. R. *The Journal of Chemical Physics* **1985**, *82*, 299.

(68) Dunning, T. H; Hay, P. J. *Methods of Electronic Structure Theory;* Plenum: New York, 1977; Vol. 2.

(69) Niu, S.; Hall, M. B. *Chem. Rev.* **2000**, *100*, 353.

(70) Chen, H.; Cong, T. N.; Yang, W.; Tan, C.; Li, Y.; Ding, Y. *Progress in Natural Science* **2009**, *19*, 291.

(71) Cook, T. R.; Dogutan, D. K.; Reece, S. Y.; Surendranath, Y.; Teets, T. S.; Nocera, D. G. *Chemical Reviews* **2010**, *110*, 6474.

(72) Kucharski, T. J.; Tian, Y.; Akbulatov, S.; Boulatov, R. *Energy & Environmental Science* **2011**, *4*, 4449.

(73) Chu, S.; Majumdar, A. *Nature* **2012**, *488*, 294.

(74) Gur, I.; Sawyer, K.; Prasher, R. *Science* **2012**, *335*, 1454.

(75) Moth-Poulsen, K.; Coso, D.; Borjesson, K.; Vinokurov, N.; Meier, S. K.; Majumdar, A.; Vollhardt, K. P. C.; Segalman, R. A. *Energy & Environmental Science* **2012**, *5*, 8534.

(76) Boese, R.; Cammack, J. K.; Matzger, A. J.; Pflug, K.; Tolman, W. B.; Vollhardt, K. P. C.; Weidman, T. W. *Journal of the American Chemical Society* **1997**, *119*, 6757.

(77) Kanai, Y.; Srinivasan, V.; Meier, S. K.; Vollhardt, K. P. C.; Grossman, J. C. *Angewandte Chemie International Edition* **2010**, *49*, 8926.

(78) Thomas E, B. *Coordination Chemistry Reviews* **2000**, *206-207*, 419.

(79) Zhu, B.; Miljanić, O. Š.; Vollhardt, K. P. C.; West, M. J. *Synthesis* **2005**, *2005*, 3373.

(80) Chen, L. X. *Annual Review of Physical Chemistry* **2005**, *56*, 221.

(81) Bloyce, P. E.; Campen, A. K.; Hooker, R. H.; Rest, A. J.; Thomas, N. R.; Bitterwolf, T. E.; Shade, J. E. *Journal of the Chemical Society, Dalton Transactions* **1990**, 2833.

(82) H. L. Friedman, *Molecular motions* in liquids, edited by J. Lascombe; Reidel, D., 1974, pp. 87–96.

(83) Yang, H.; Snee, P. T.; Kotz, K. T.; Payne, C. K.; Harris, C. B. *Journal of the American Chemical Society* **2001**, *123*, 4204.

(84) The mechanism by which demetallation occurs is obscure, but CpM-CCl_3 complexes are (photo)labile and reactions of Cp*M systems with CCl_4 are known to form demetallated $(CCl_3)Me_5$Cyclopentadienes. For pertinent literature, see: a) Y. Chen, Y. Zhou, J. Qu, Organometallics **2008**, *27*, 666; b) H. Shimakoshi, Y. Maeyama, T. Kaieda, T. Matsuo, E. Matsui, Y. Naruta, Y. Hisaeda, Bull. Chem. Soc. Jpn. **2005**, *78*, 859; c) J. L. Male, F. W. B. Einstein, W. K. Leong, R. K. Pomeroy, D. R. Tyler, Inorg. Chim. Acta **1997**, *549*, 105; d) J. J. Schneider, R. Goddard, C. Krüger, Z. Naturforsch. B **1995**, *50*, 448; e) T. G. Richmond, A. M. Crespi, D. F. Shriver, Organometallics **1984**, *3*, 314; f) T. G. Richmond, D. F. Shriver, Organometallics **1984**, *3*, 305.

(85) Harpham, M. R.; Nguyen, S. C.; Hou, Z.; Grossman, J. C.; Harris, C. B.; Mara, M. W.; Stickrath, A. B.; Kanai, Y.; Kolpak, A. M.; Lee, D.; Liu, D.-J.; Lomont, J. P.; Moth-Poulsen, K.; Vinokurov, N.; Chen, L. X.; Vollhardt, K. P. C. *Angewandte Chemie International Edition* **2012**, *51*, 7692.

(86) de Azevedo, C. G.; Vollhardt, K. P. C. *Synlett* **2002**, *2002*, 1019.

(87) Ceccon, A.; Santi, S.; Orian, L.; Bisello, A. *Coordination Chemistry Reviews* **2004**, *248*, 683.

(88) González-Maupoey, M.; Tabernero, V.; Cuenca, T. *Coordination Chemistry Reviews* **2009**, *253*, 1854.

(89) Bister, H.-J.; Butenschön, H. *Synlett* **1992**, *1992*, 22.

(90) Jutzi, P.; Schnittger, J.; Dahlhaus, J.; Gestmann, D.; Leue, H.-C. *Journal of Organometallic Chemistry* **1991**, *415*, 117.

(91) W. B. Tolman and K. P. C. Vollhardt, unpublished.

(92) Vollhardt, K. P. C.; Weidman, T. W. *Organometallics* **1984**, *3*, 82.

(93) Hou, Z.; Nguyen, S. C.; Lomont, J. P.; Harris, C. B.; Vinokurov, N.; Vollhardt, K. P. C. *Physical Chemistry Chemical Physics* **2013**, *15*, 7466.

(94) Howie, R. A.; McQuillan, G. P.; Thompson, D. W.; Lock, G. A. *Journal of Organometallic Chemistry* **1986**, *303*, 213.

(95) CCDC 924375

(96) Bryan, R. F.; Greene, P. T.; Newlands, M. J.; Field, D. S. *Journal of the Chemical Society A: Inorganic, Physical, Theoretical* **1970**, 3068.

(97) Baiz, C. R.; McCanne, R.; Kubarych, K. J. *Journal of the American Chemical Society* **2009**, *131*, 13590.

(98) Moore, B. D.; Simpson, M. B.; Poliakoff, M.; Turner, J. J. *Journal of the Chemical Society, Chemical Communications* **1984**, 972.

(99) Oppelt, K.; Egbe, D. A. M.; Monkowius, U.; List, M.; Zabel, M.; Sariciftci, N. S.; Knör, G. *Journal of Organometallic Chemistry* **2011**, *696*, 2252.

(100) Hsu, C.-C.; Lin, C.-C.; Chou, P.-T.; Lai, C.-H.; Hsu, C.-W.; Lin, C.-H.; Chi, Y. *Journal of the American Chemical Society* **2012**, *134*, 7715.

(101) Lomont, J. P.; Nguyen, S. C.; Harris, C. B. *Organometallics* **2012**, *31*, 3947.

(102) Ma, C.; Chan, C. T.-L.; Kwok, W.-M.; Che, C.-M. *Chemical Science* **2012**, *3*, 1883.

(103) Zhou, Q.; Lei, W.; Chen, Y.; Li, C.; Hou, Y.; Zhang, B.; Wang, X. *Chemistry – A European Journal* **2012**, *18*, 8617.

(104) Siegbahn, P. E. M. *Journal of the American Chemical Society* **1996**, *118*, 1487.

(105) Portius, P.; Yang, J.; Sun, X.-Z.; Grills, D. C.; Matousek, P.; Parker, A. W.; Towrie, M.; George, M. W. *Journal of the American Chemical Society* **2004**, *126*, 10713.

(106) Crabtree, R. H. *The Organometallic Chemistry of Transition Metals 4th ed.; John Wiley & Sons: New York, NY, 2005, p. 241.*

(107) Long, G. T.; Weitz, E. *Journal of the American Chemical Society* **2000**, *122*, 1431.

(108) Sawyer, K. R.; Glascoe, E. A.; Cahoon, J. F.; Schlegel, J. P.; Harris, C. B. *Organometallics* **2008**, *27*, 4370.

(109) Shanoski, J. E.; Glascoe, E. A.; Harris, C. B. *The Journal of Physical Chemistry B* **2006**, *110*, 996.

(110) **L1** = alkane-coordinated token ligand; **L2** = hydroxyl-coordinated token ligand.

(111) Bachler, V.; Grevels, F.-W.; Kerpen, K.; Olbrich, G.; Schaffner, K. *Organometallics* **2003**, *22*, 1696.

(112) Burdett, J. K. *Journal of the Chemical Society, Faraday Transactions 2: Molecular and Chemical Physics* **1974**, *70*, 1599.

(113) The peak areas for kinetics traces of all species are baseline-corrected and integrated from 1883 to 1903 cm^{-1} in the TRIR spectra. Each rise time constant is fitted to a single exponential; the error is one standard deviation of the mean. (see Appendix B)

(114) In the ideal condition for diffusion-controlled bimolecular reaction of the metal center and hydroxyl group, the rise time constant should increase proportionally with the viscosity of the solution. However, our experimental rise time constants increase slower than they are expected with viscosity. We think the solvation may happen faster than the expected diffusion of the hydroxyl group because the hydroxyl group may be already closed to the metal complexes in the first solvation shell.

(115) Rosspeintner, A.; Lang, B.; Vauthey, E. *Annual Review of Physical Chemistry* **2013**, *64*, 247.

(116) Hamm, P.; Ohline, S. M.; Zinth, W. *The Journal of Chemical Physics* **1997**, *106*, 519.

(117) Kovalenko, S. A.; Dobryakov, A. L.; Pollak, E.; Ernsting, N. P. *The Journal of Chemical Physics* **2013**, *139*, 011101.

(118) Lian, T.; Locke, B.; Kholodenko, Y.; Hochstrasser, R. M. *The Journal of Physical Chemistry* **1994**, *98*, 11648.

(119) Deàk, J. C.; Iwaki, L. K.; Dlott, D. D. *The Journal of Physical Chemistry A* **1999**, *103*, 971.

(120) Iwaki, L. K.; Dlott, D. D. *The Journal of Physical Chemistry A* **2000**, *104*, 9101.

(121) Fini, G.; Mirone, P. *Spectrochimica Acta Part A: Molecular Spectroscopy* **1976**, *32*, 439.

(122) Allen, N. D. C.; Harrison, J. J.; Bernath, P. F. *Journal of Quantitative Spectroscopy and Radiative Transfer* **2011**, *112*, 1961.

(123) Bian, H.; Wen, X.; Li, J.; Zheng, J. *The Journal of Chemical Physics* **2010**, *133*.

(124) Reimers, J. R.; Hall, L. E. *Journal of the American Chemical Society* **1999**, *121*, 3730.

(125) Rinsland, C. P.; Sharpe, S. W.; Sams, R. L. *Journal of Quantitative Spectroscopy and Radiative Transfer* **2005**, *96*, 271.

(126) Harris, A. L.; Brown, J. K.; Harris, C. B. *Annual Review of Physical Chemistry* **1988**, *39*, 341.

(127) Lian, T.; Bromberg, S. E.; Asplund, M. C.; Yang, H.; Harris, C. B. *The Journal of Physical Chemistry* **1996**, *100*, 11994.

(128) Weigel, A.; Ernsting, N. P. *The Journal of Physical Chemistry B* **2010**, *114*, 7879.

(129) This term has been used widely in literature, see Ref 121, 124, 130. The population of this hot band arises from the anharmonic coupling of the CN-stretching mode to the thermally excited low frequency CCN-bending mode at high temperature.

(130) Vojta, D.; Baranović, G. *Vibrational Spectroscopy* **2010**, *52*, 178.

(131) Pace, E. L.; Lewis, J. N. *The Journal of Chemical Physics* **1968**, *49*, 5317.

(132) Tanaka, H.; Matsumoto, A.; Unger, K. K.; Kaneko, K. In *Studies in Surface Science and Catalysis*; K.K. Unger, G. K., Baselt, J. P., Eds.; Elsevier: 2000; Vol. Volume 128, p 251.

(133) These spectra are scaled to their solution density at each elevated temperature so that all the measurement spectra have the same number of absorption molecules. Thermal expansion of the sample cell is negligible. When not scaled, the difference spectra still looks similar to the scaled spectra and the linear dependence between the temperature change and the IR absorption change is still hold.

(134) Lebedkin, S. F.; Klimov, A. D. *Chemical Physics Letters* **1992**, *190*, 313.

(135) Bernstein, M.; Simon, J. D.; Peters, K. S. *Chemical Physics Letters* **1983**, *100*, 241.

(136) Lewis, K. E.; Golden, D. M.; Smith, G. P. *Journal of the American Chemical Society* **1984**, *106*, 3905.

(137) Goodman, J. L.; Peters, K. S.; Vaida, V. *Organometallics* **1986**, *5*, 815.

(138) Smith, G. P. *Polyhedron* **1988**, *7*, 1605.

(139) Fletcher, T. R.; Rosenfeld, R. N. *Journal of the American Chemical Society* **1988**, *110*, 2097.

(140) Cammenga, H. K.; Emel'yanenko, V. N.; Verevkin, S. P. *Industrial & Engineering Chemistry Research* **2009**, *48*, 10120.

(141) Berg, M.; Harris, A. L.; Harris, C. B. *Physical Review Letters* **1985**, *54*, 951.

(142) Harris, A. L.; Berg, M.; Harris, C. B. *The Journal of Chemical Physics* **1986**, *84*, 788.

(143) Xu, X.; Yu, S.-C.; Lingle, J. R.; Zhu, H.; Hopkins, J. B. *The Journal of Chemical Physics* **1991**, *95*, 2445.

(144) Scherer, N. F.; Jonas, D. M.; Fleming, G. R. *The Journal of Chemical Physics* **1993**, *99*, 153.

(145) Xu, J.; Schwentner, N.; Chergui, M. *The Journal of Chemical Physics* **1994**, *101*, 7381.

(146) Lee, J. H.; Wulff, M.; Bratos, S.; Petersen, J.; Guerin, L.; Leicknam, J.-C.; Cammarata, M.; Kong, Q.; Kim, J.; Møller, K. B.; Ihee, H. *Journal of the American Chemical Society* **2013**, *135*, 3255.

(147) Kang, T. J.; Yu, J.; Berg, M. *The Journal of Chemical Physics* **1991**, *94*, 2413.

(148) Smith, D. E.; Harris, C. B. *The Journal of Chemical Physics* **1987**, *87*, 2709.

(149) Both 400 and 267 nm excitation yield qualitatively similar spectra, but 267 nm excitation yields too weak of a signal to observe quality kinetic traces; this is due to the low absorption cross section of I_2 at 267 nm combined with the lower intensity of the 267 nm pulses, relative to the 400 nm pulses, in our experimental setup.

(150) Ho, T.-I.; Su, T.-M.; Hwang, T.-C. *Journal of Photochemistry and Photobiology A: Chemistry* **1988**, *41*, 293.

(151) Sension, R. J.; Repinec, S. T.; Szarka, A. Z.; Hochstrasser, R. M. *The Journal of Chemical Physics* **1993**, *98*, 6291.

(152) Rodier, J. M.; Myers, A. B. *Journal of the American Chemical Society* **1993**, *115*, 10791.

(153) Phillips, D. L.; Rodier, J. M.; Myers, A. B. In *Time-Resolved Vibrational Spectroscopy VI*; Lau, A., Werncke, W., Siebert, F., Eds.; Springer Berlin Heidelberg: 1994; Vol. 74, p 95.

(154) Steinhurst, D. A.; Baronavski, A. P.; Owrutsky, J. C. *Chemical Physics Letters* **2002**, *361*, 513.

(155) Owrutsky, J. C.; Baronavski, A. P. *The Journal of Chemical Physics* **1996**, *105*, 9864.

(156) Baiz, C. R.; McCanne, R.; Nee, M. J.; Kubarych, K. J. *The Journal of Physical Chemistry A* **2009**, *113*, 8907.

(157) Dougherty, T. P.; Heilweil, E. J. *Chemical Physics Letters* **1994**, *227*, 19.

(158) King, J. C.; Zhang, J. Z.; Schwartz, B. J.; Harris, C. B. *The Journal of Chemical Physics* **1993**, *99*, 7595.

(159) Baiz, C. R.; Kubarych, K. J. *Journal of the American Chemical Society* **2010**, *132*, 12784.

(160) Lian, T.; Kholodenko, Y.; Hochstrasser, R. M. *The Journal of Physical Chemistry* **1995**, *99*, 2546.

(161) Sukowski, U.; Seilmeier, A.; Elsaesser, T.; Fischer, S. F. *The Journal of Chemical Physics* **1990**, *93*, 4094.

(162) Stratt, R. M.; Maroncelli, M. *The Journal of Physical Chemistry* **1996**, *100*, 12981.

(163) O'Driscoll, E.; Simon, J. D. *Journal of the American Chemical Society* **1990**, *112*, 6580.

(164) Deàk, J. C.; Pang, Y.; Sechler, T. D.; Wang, Z.; Dlott, D. D. *Science* **2004**, *306*, 473.

(165) Kim, Y. S.; Hochstrasser, R. M. *Proceedings of the National Academy of Sciences of the United States of America* **2005**, *102*, 11185.

(166) Simon, J. D.; Xie, X. *The Journal of Physical Chemistry* **1986**, *90*, 6751.

(167) Joly, A. G.; Nelson, K. A. *Chemical Physics* **1991**, *152*, 69.

(168) The oscillation strength of COs stretching vibration of these organometallics complexes are about 600 times stronger than that of CN stretching of AcN, based on the FTIR spectra of these complexes in AcN solution. As demonstrated in the TRIR spectra of $Cr(CO)_6$ solution, the COs stretching bands of the depleted $Cr(CO)_6$ are measured about 4 mOD at 100 ps delay, thus the CN stretching band of photoproduct-coordinated AcN is roughly expected at 7 μOD, a quite small value comparing to the instensity of TRIR spectra (See Fig. 5.5).

(169) Pigliucci, A.; Duvanel, G.; Daku, L. M. L.; Vauthey, E. *The Journal of Physical Chemistry A* **2007**, *111*, 6135.

(170) Xu, X.; Yu, S.-C.; Robert Lingle, J.; Zhu, H.; Hopkins, J. B. *The Journal of Chemical Physics* **1991**, *95*, 2445.

(171) Since the solvent absorption cross section changes linearly with changes in temperature, a nonuniform temperature within the probed volume would be expected to yield spectra essentially identical to those in which there is a uniform temperature within the

volume probed, given that the same total amount of heat was deposited, see Ref.160. In reality, the Gaussian spatial profile of the UV/Vis excitation laser pulses will create a nonuniform photoproduct distribution, and consequently a nonuniform temperature distribution within the probed volume.

(172) Handbook of Chemistry & Physics, 93th ed. CRC Press [Online] 2012.

(173) L.D. Landau, E. M. L. Fluid Mechanics, 2nd ed; Pergamon Press; New York, **1987**, 192.

(174) Were these two factors to contribute to the TRIR solvent spectra, we would see either the negative or positive bands at 2254 and 2294 cm^{-1} but not the broad positive regions on the low and high frequency side of the 2254 cm^{-1} band. The fact that these spectral features, as a result of temperature broadening and blue-shifting, are observed in both the temperature-dependent FTIR (Fig. 5.2b) and TRIR (Fig. 5.3-5.5) spectra confirms that the TRIR spectra arise from heating of the solvent.

(175) Sajadi, M.; Dobryakov, A. L.; Garbin, E.; Ernsting, N. P.; Kovalenko, S. A. *Chemical Physics Letters* **2010**, *489*, 44.

(176) Laman, D. M.; Falvey, D. E. *Review of Scientific Instruments* **1996**, *67*, 3260.

(177) Lukianova-Hleb, E.; Hu, Y.; Latterini, L.; Tarpani, L.; Lee, S.; Drezek, R. A.; Hafner, J. H.; Lapotko, D. O. *ACS Nano* **2010**, *4*, 2109.

(178) Govorov, A. O.; Richardson, H. H. *Nano Today* **2007**, *2*, 30.

(179) Huang, J.; Park, J.; Wang, W.; Murphy, C. J.; Cahill, D. G. *ACS Nano* **2012**, *7*, 589.

(180) Tyrell, H. J. V. H., K. R. *Diffusion in Liquids;* Butterworths: London*, 1984*.

(181) G. R. Fleming *Chemical Applications of Ultrafast Spectroscopy,* Oxford University Press: New York, *1986.*

(182) Jacek Waluk, *Conformational Analysis of Molecules in Excited States*, Wiley-VCH, Inc., 2000.

(183) Nichols, K. B.; Rodriguez, A. A. *The Journal of Physical Chemistry A* **2005**, *109*, 3009.

(184) Kim, Y. R.; Hochstrasser, R. M. *The Journal of Physical Chemistry* **1992**, *96*, 9595.

(185) Hynes, J. T.; Kapral, R.; Weinberg, M. *The Journal of Chemical Physics* **1978**, *69*, 2725.

(186) Ould-Kaddour, F.; Levesque, D. *Physical Review E* **2000**, *63*, 011205.

(187) Willeke, M. *Molecular Physics* **2003**, *101*, 1123.

(188) Willeke, M. *Molecular Physics* **2005**, *103*, 1353.

(189) Easteal, A. J.; Woolf, L. A. *Chemical Physics Letters* **1990**, *167*, 329.

(190) Bauer, D. R.; Brauman, J. I.; Pecora, R. *Journal of the American Chemical Society* **1974**, *96*, 6840.

(191) Kivelson, D.; Madden, P. A. *Annual Review of Physical Chemistry* **1980**, *31*, 523.

(192) Fury, M.; Jonas, J. *The Journal of Chemical Physics* **1976**, *65*, 2206.

(193) Mills, R.; Harris, K. R. *Chemical Society Reviews* **1976**, *5*, 215.

(194) Weingartner, H. *Journal of the Chemical Society, Faraday Transactions 1: Physical Chemistry in Condensed Phases* **1985**, *81*, 1031.

(195) Shankland, I. R.; Arora, P. S.; Dunlop, P. J. *The Journal of Physical Chemistry* **1977**, *81*, 1518.

(196) John, G. A.; Keichi, A. *The Journal of Chemical Physics* **1976**, *64*, 81.

(197) Motohiro, B.; Koichi, I.; Hiro-o, H. *Intra- and intermolecular vibrational energy transfer in tungsten carbonyl complexes W(CO)$_5$(X) (X = CO, CS, CH$_3$CN, and CD$_3$CN)*; AIP, 2007; Vol. 126.

(198) Golonzka, O.; Tokmakoff, A. *The Journal of Chemical Physics* **2001**, *115*, 297.

(199) Robin M, H. *Chemical Physics* **2001**, *266*, 273.

(200) Tokmakoff, A.; Urdahl, R. S.; Zimdars, D.; Francis, R. S.; Kwok, A. S.; Fayer, M. D. *Vibrational spectral diffusion and population dynamics in a glass forming liquid: Variable bandwidth picosecond infrared spectroscopy*; AIP, 1995; Vol. 102.

(201) Gerald, M. S.; Zhong, Q.; Owrutsky, J. C. *Vibrational and rotational dynamics of cyanoferrates in solution*; AIP, 2004; Vol. 121.

(202) For example, vibrational life time of the 2045 cm^{-1} peak of Mn$_2$(CO)$_{10}$ in *n*-hexadecane is 166 ± 24 ps, which does not have enough intensity at long delay time to determine when *r(t)* is closed to zero. Thus, *r(t)* fitting is not reliable.

(203) Fitzpatrick, P. J.; Le Page, Y.; Sedman, J.; Butler, I. S. *Inorganic Chemistry* **1981**, *20*, 2852.

(204) Calculated molecular volume (cm^3/mol): CpMn(CO)$_3$: 121; CpRe(CO)$_3$: 123; Mn$_2$(CO)$_{10}$: 202; Re$_2$(CO)$_{10}$: 203; *n*-pentane (roll configuration): 76; *n*-pentane (linear configuration): 83; *n*-hexadecane (linear configuration): 238; *n*-hexadecane (roll configurations): 239-243.

(205) Shilov, A. E.; Shul'pin, G. B. *Chemical Reviews* **1997**, *97*, 2879.

(206) The moment of inertia could be calculated from frequency calculation. However, Gaussian cannot report this value for Re$_2$(CO)$_{10}$ since the result is too large. We, therefore calculate this values for all compounds. Our result is in exellence agreement with Gaussian.

(207) Churchill, M. R.; Amoh, K. N.; Wasserman, H. J. *Inorganic Chemistry* **1981**, *20*, 1609.

(208) Kivelson, D. *Faraday Symposia of the Chemical Society* **1977**, *11*, 7.

(209) The metal is located at 0.019 and 0.025 Angstrom for CpMn(CO)$_3$ and CpRe(CO)$_3$, respectively, from the center of mass.

(210) David, C. *The Journal of Chemical Physics* **1975**, *62*, 1358.

(211) Lomont, J. P.; Shearer, A. J.; Nguyen, S. C.; Harris, C. B. *Organometallics* **2013**, *32*, 2178.

(212) Glascoe, E. A.; Sawyer, K. R.; Shanoski, J. E.; Harris, C. B. In *The Journal of Physical Chemistry C* **2007**; *111*, 8789.

Appendix A. Supporting information for Chapter 3

1. DFT calculation for the Ru system

1.1. FTIR spectra

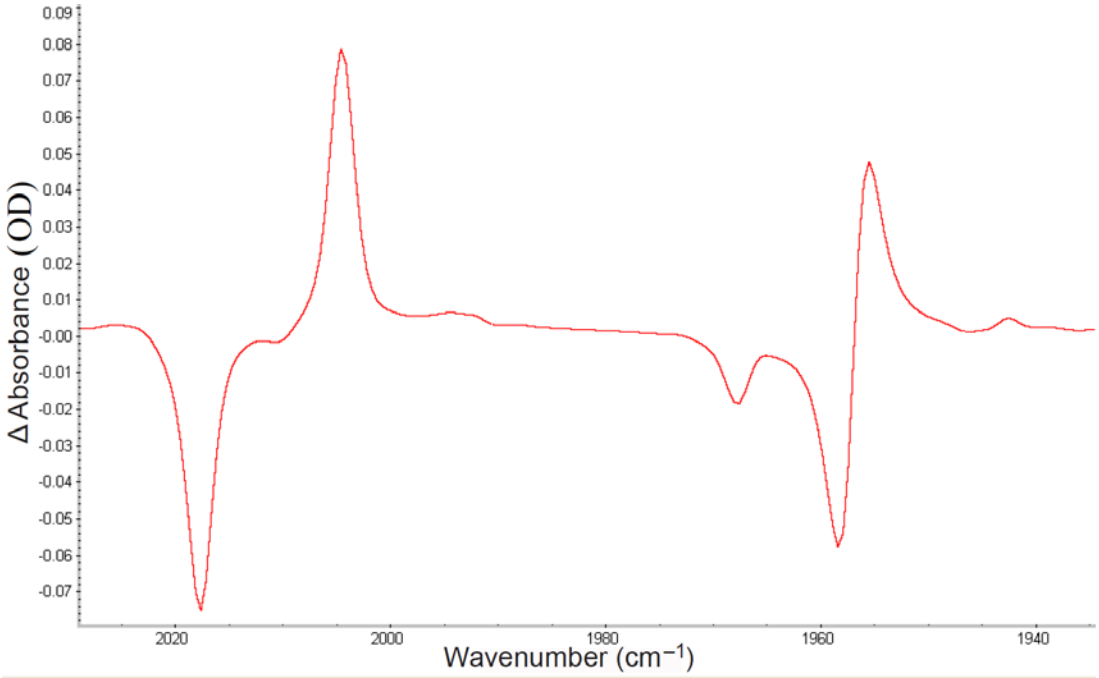

Figure A1. FTIR characterization of **1b** (2017, 1966, 1957 cm^{-1}) and **2b** (2004, 1955 cm^{-1}) in heptane. The difference spectra are obtained by subtracting the signals of the sample in the non-flowed Harrick cell from those generated after irradiating with a 400 nm laser pulse.

1.2. Potential energy surface scan – DFT calculation

An energy scan was performed by stretching the Ru–Ru bond in **1a** on the singlet and triplet surfaces. The singlet syn-biradical structure **D*** collapses back to **1a**, while the triplet analog **E*** could be located and exhibits a Ru–Ru distance of 4.530 Å. For purposes of illustration, an artificial structure of **D*** was modeled by first inserting butane between the two Ru centers and optimization. This adduct exhibits a local minimum with a Ru–Ru distance of 4.790 Å. The picture for **D*** was then generated by deleting the solvent. Product **F*** was simulated by removing one CO ligand from **1a** and subsequent optimization of the structure.

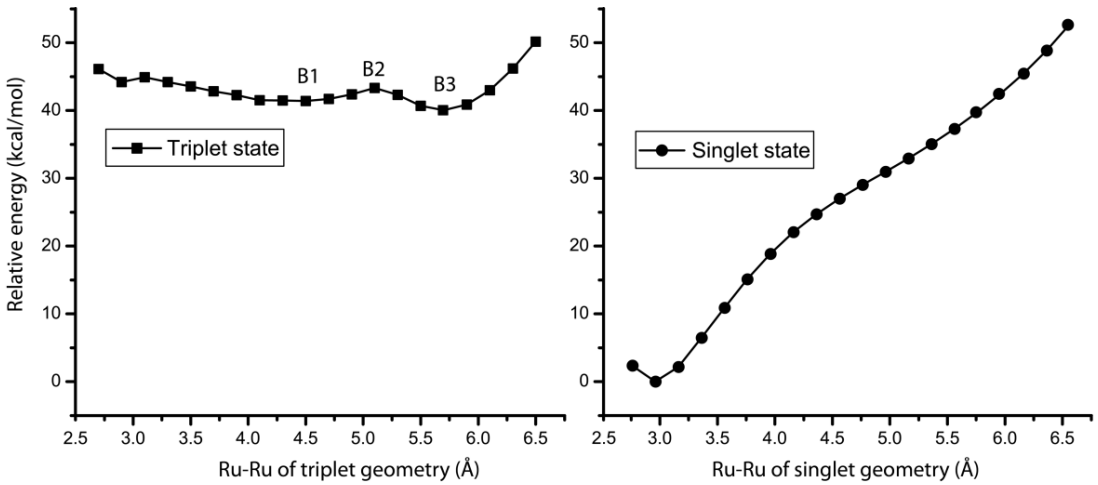

Figure A2: Energy scan of singlet and triplet ground states when scanning Ru-Ru distant (BP86 result). Minimum of singlet state is set at 0 for both graph. The triplet state has two local minima at long distant, while the singlet state only has one minimum at structure of **1**.

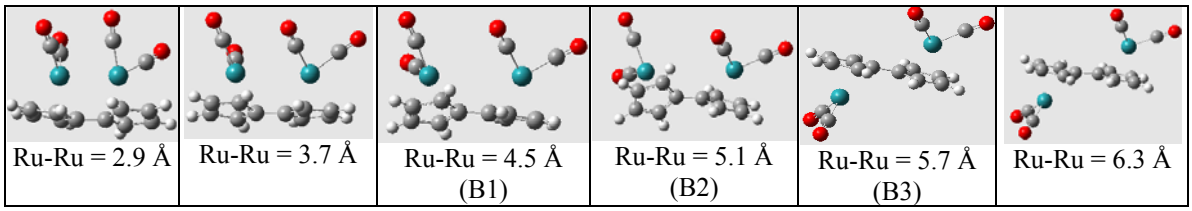

Figure A3: Selected structures at triplet state when scanning Ru-Ru distance.

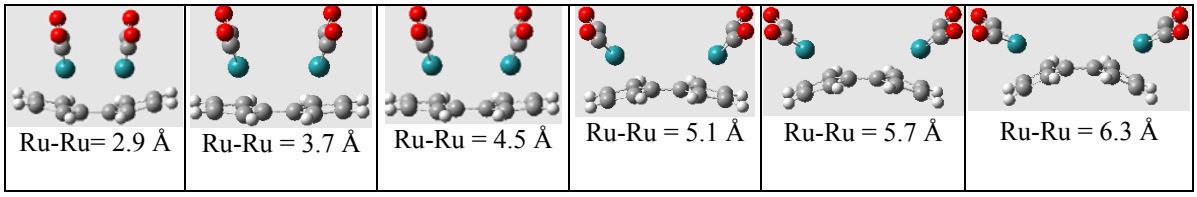

Figure A4: Selected structures at singlet state when scanning Ru-Ru distance.

Molecular coordinates

D*

C	3.16543600	-1.97732900	-1.01453400
C	0.94449200	-1.97595500	-0.22649300
C	1.79648900	-1.75864200	-1.38830000
C	1.85735500	-2.09883000	0.90232900
C	3.20320700	-2.18958300	0.40892700
C	3.24275900	1.23684200	-1.16531400

C	3.35813300	0.81296300	1.48530400
C	-2.68207700	-2.47877900	-0.92865200
C	-0.47382300	-2.09001700	-0.20527200
C	-1.37930000	-2.04330800	-1.34575700
C	-1.32481100	-2.33351400	0.95159700
C	-2.64899200	-2.65775500	0.49961700
C	-3.34197700	0.64276200	-1.14682000
C	-3.28439100	0.30088500	1.51769700
H	4.02046900	-1.99810400	-1.69027700
H	1.44690800	-1.59457500	-2.40798100
H	1.56261800	-2.24696400	1.94160300
H	4.09178400	-2.40196800	1.00347800
H	-3.53782500	-2.65944000	-1.57918600
H	-1.08661000	-1.85212500	-2.37863300
H	-0.98377600	-2.40279700	1.98495700
H	-3.47485300	-2.99977600	1.12340600
O	3.72243800	1.98394000	-1.93351400
O	3.91131900	1.28972100	2.40481000
O	-3.98596900	1.25053800	-1.91795000
O	-3.88751800	0.69569000	2.44471900
Ru	2.56201400	-0.06485200	0.01980300
Ru	-2.39124700	-0.46586600	0.04600300

E*

C	-3.01167200	-1.95773800	-0.24827800
C	-0.70183000	-1.56878400	-0.21698200
C	-1.83072000	-1.97385700	0.58645200
C	-1.20761200	-1.22639000	-1.52151200
C	-2.62858900	-1.49488400	-1.54626800
H	-4.01627000	-2.24679000	0.06020700
H	-1.77913800	-2.32435800	1.61735700
H	-0.60752100	-0.86511300	-2.35720500
H	-3.28999100	-1.36148400	-2.40216300
C	2.62858600	-1.49496000	1.54621300
C	0.70182300	-1.56879900	0.21693200
C	1.20761200	-1.22645200	1.52147100
C	1.83070700	-1.97385500	-0.58652000
C	3.01166100	-1.95777500	0.24820700
H	3.28999200	-1.36159500	2.40211100
H	0.60752800	-0.86519200	2.35717600
H	1.77911700	-2.32432200	-1.61743700
H	4.01625500	-2.24682700	-0.06029100
Ru	-2.26469700	0.21538600	-0.02886300
Ru	2.26470700	0.21536800	0.02886800
C	-3.36177600	0.85808800	1.36034100

O	-4.08832700	1.20142100	2.21574300
C	-2.58787000	1.75489300	-1.06949600
O	-2.82257200	2.67025200	-1.76432400
C	2.58786500	1.75484400	1.06955100
O	2.82255200	2.67018600	1.76440400
C	3.36178100	0.85816400	-1.36029800
O	4.08832100	1.20158100	-2.21567500

F*

C	2.72718500	-1.36848800	-1.09627600
C	0.56519900	-1.96110300	-0.41386400
C	1.36888400	-1.52621400	-1.53918500
C	1.45027700	-2.01947600	0.73072000
C	2.77512300	-1.66485400	0.30011600
H	3.57047600	-1.07323700	-1.72057600
H	1.01110600	-1.37302800	-2.55729700
H	1.16607500	-2.29728300	1.74550400
H	3.66393800	-1.63618000	0.93052200
C	-3.01606400	-0.91708100	-0.67396000
C	-0.88950400	-1.89685100	-0.33715500
C	-1.71696400	-1.13779800	-1.29258500
C	-1.67495000	-2.03879000	0.85285700
C	-2.98146600	-1.45696700	0.65147700
H	-3.86743100	-0.42982300	-1.14951900
H	-1.45056400	-0.89945400	-2.32248000
H	-1.32126500	-2.46480000	1.79326700
H	-3.79588300	-1.44955900	1.37537100
Ru	1.32980400	0.19571800	0.01944100
Ru	-1.39787100	0.20597100	0.31649000
C	1.34929700	1.76317700	-1.00469700
O	1.40191400	2.72438500	-1.67634500
C	1.50382300	1.22688900	1.57174900
O	1.64813500	1.84876400	2.55949100
C	-1.85424300	1.93203400	-0.23546900
O	-2.25268500	2.96962400	-0.62791500

2. DFT Calculations for Fe system

The structural assignment of the experimentally detected species **E,** *tert*-$Bu_2FvFe_2(CO)_3$, was assisted by DFT calculations of the unsubstituted analog $FvFe_2(CO)_3$ (Fig. A5). This structure was simulated by removing one CO ligand from $FvFe_2(CO)_4$ and subsequent optimization. Figure A6 shows the ground-state structure of triplet $FvFe_2(CO)_4$, the energy of which is reported in Figure 3.9.

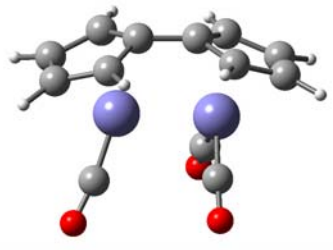

Figure A5. Structure of $FvFe_2(CO)_3$.

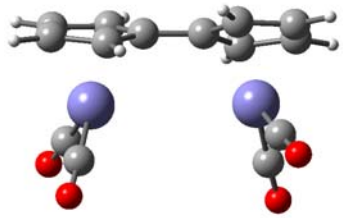

Figure A6. Structure of triplet $FvFe_2(CO)_4$ (**3a**).

Molecular coordinates

$FvFe_2(CO)_3$

C	2.86755300	-0.73510500	-0.91687700
C	0.83359800	-1.74542000	-0.33792300
C	1.59635300	-1.18006200	-1.42968700
C	1.65562100	-1.62921600	0.84609200
C	2.90186900	-1.00740900	0.48013100
H	3.65337400	-0.25298600	-1.49821400
H	1.25912400	-1.08065000	-2.46114200
H	1.37273800	-1.92871700	1.85464800
H	3.71997900	-0.77272900	1.16086800
C	-2.78432000	-1.03106700	-0.69757300
C	-0.62667600	-1.86353400	-0.30711600
C	-1.50150100	-1.25917600	-1.30979900
C	-1.39990600	-1.96412400	0.90179100
C	-2.71932900	-1.45345700	0.67192900
H	-3.64326600	-0.57177400	-1.18733700
H	-1.23730300	-1.01681800	-2.33886100
H	-1.01375200	-2.26971700	1.87568800
H	-3.52125200	-1.39241500	1.40711600
Fe	1.20585600	0.28719900	0.04036100
Fe	-1.23742300	0.03558600	0.21570900
C	1.02794200	1.69925700	-0.95975200
O	0.95509700	2.64255400	-1.65497300
C	1.00436400	1.22618800	1.49407600

O	0.91752600	1.85532100	2.48491300
C	-1.93116000	1.62164700	-0.06627600
O	-2.53704200	2.60490500	-0.29052500

Triplet $FvFe_2(CO)_4$

C	3.04335200	-1.72101500	-0.01859700
C	0.71676800	-1.53149200	0.16071000
C	1.79563600	-1.76392800	-0.76012800
C	1.30897100	-1.26638500	1.44609500
C	2.74345800	-1.42924600	1.33902800
H	4.03614300	-1.87558300	-0.44111700
H	1.69191300	-2.00427200	-1.81815700
H	0.76313900	-1.02013100	2.35739400
H	3.46186000	-1.30476900	2.14871700
C	-2.74343600	-1.42927200	-1.33902900
C	-0.71674700	-1.53149800	-0.16071000
C	-1.30895100	-1.26639900	-1.44609600
C	-1.79561300	-1.76393700	0.76012900
C	-3.04332800	-1.72103900	0.01859700
H	-3.46183900	-1.30480100	-2.14871900
H	-0.76312100	-1.02014400	-2.35739600
H	-1.69188900	-2.00427700	1.81815900
H	-4.03611800	-1.87561200	0.44111600
Fe	2.05330900	0.19492500	0.05676500
Fe	-2.05330200	0.19490900	-0.05677000
C	2.96639600	1.00586100	-1.19787800
O	3.61677600	1.52243800	-2.02639500
C	2.09447700	1.57292400	1.13965200
O	2.15679500	2.46968400	1.89274400
C	-2.09446400	1.57291100	-1.13965400
O	-2.15686700	2.46972200	-1.89267800
C	-2.96640600	1.00583100	1.19786900
O	-3.61682100	1.52240900	2.02635800

Appendix B. Supporting information for Chapter 4

TRIR spectra of $Fe(CO)_5$ in *n*-heptane solution with 267-nm light.

We have repeated this experiment to verify the peak positions, helping us to assign the spectra in alcohol solvents better. Figure B1 shows TRIR spectra of $Fe(CO)_5$ recorded in room temperature n-heptane using 267-nm pump pulses. All peaks in the spectra are associated with CO stretching modes. For clarity, the spectra are scaled to the height of the photoproduct peaks, rather than the parent bleaches at 2001 and 2023 cm^{-1}. The peaks at 1967 and 1988 cm^{-1} correspond to triplet $^3Fe(CO)^4$, and the peak at 1953 cm^{-1} corresponds to alkane-coordinated $^1Fe(CO)_4$ (^{1}**4•L1**). The 1973 and 1989 cm^{-1} peaks of ^{1}**4•L1** are overlapped by the peaks of ^{3}**4**. The peak at 1928 cm^{-1} has been assigned to alkane-coordinated $^3Fe(CO)_3$ (^{3}**3•L1**) by other authors (Table 2, their assignment is 1926 cm^{-1}, the reason for this difference comes from the resolution of the detector).

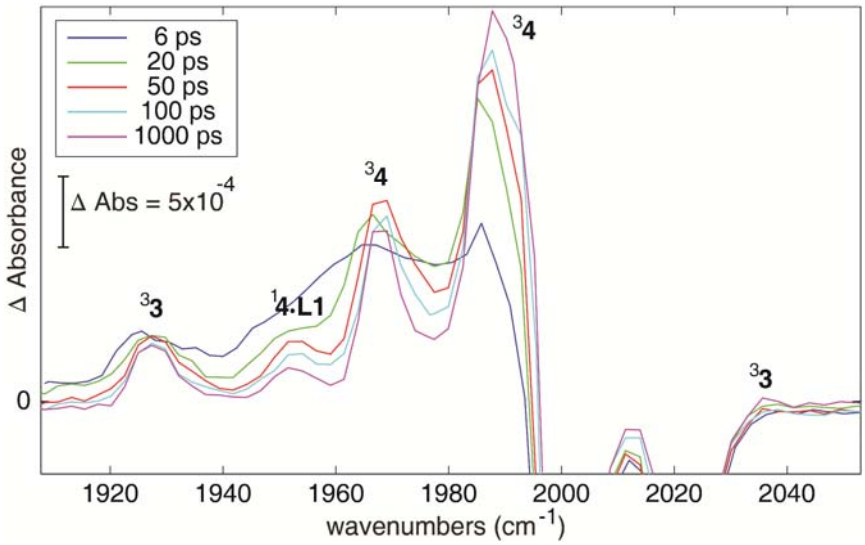

Figure B1. TRIR spectra of $Fe(CO)_5$ in *n*-heptane with 267-nm excitation pulses. Previous studies assigned the 1928 cm^{-1} peak to alkane-coordinated triplet $^3Fe(CO)_3$, while our new assignment is to unsolvated triplet $^3Fe(CO)_3$. Parent bleaches are not shown.

We also observed a very weak peak corresponding to ^{3}**3** at ~2036 cm^{-1} (Figure B1) but its low intensity means that we cannot make definitive statements about its kinetics. We also see a small shoulder in the 1935–1940 cm^{-1} region in Figure B2. This shoulder is stable for >1.5 ns. It is likely this feature is a ^{13}CO stretch, shifted from the 1967 cm^{-1} CO stretching mode of ^{3}**4**. In ^{13}CO enrichment experiments, the same ^{13}CO stretching mode was observed at 1940 cm^{-1} in argon matrices. DFT frequency calculations also predict a ~33 cm^{-1} red-shift for ^{13}CO stretching absorptions. Compared to the ^{12}CO stretching frequency of 1967 cm^{-1} band, this is in good agreement with our observed results.

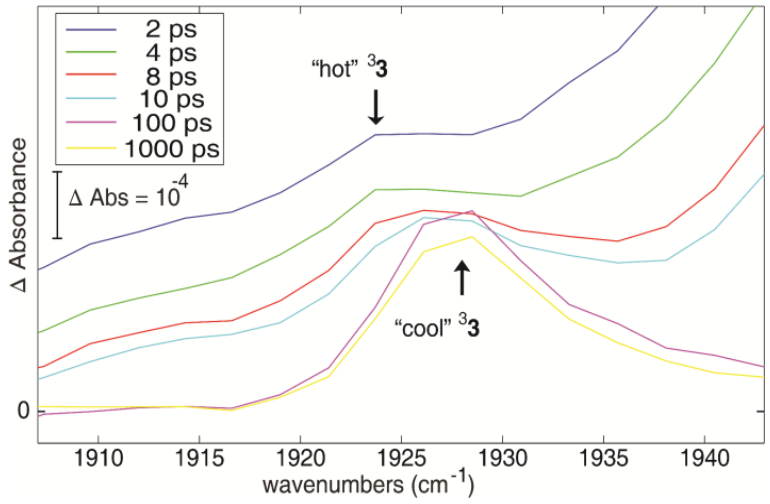

Figure B2. Detailed TRIR spectra of $Fe(CO)_5$ in *n*-heptane with 267-nm excitation pulses in $Fe(CO)_3$-absorbance region.

TRIR spectra of $Fe(CO)_5$ in 1-butanol solution 267-nm light

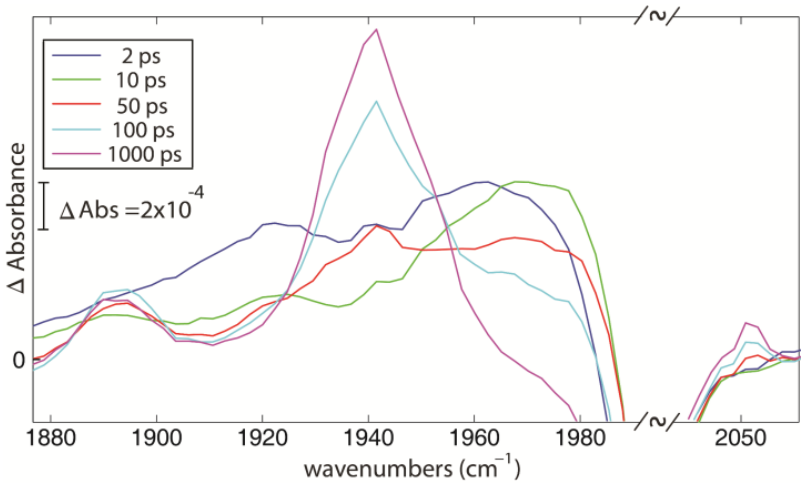

Figure B3. TRIR spectra of $Fe(CO)_5$ in 1-butanol with 267 nm pulse, parent peaks are not shown. The spectra show a qualitative conversion of the 1923 cm^{-1} to 1893 cm^{-1} peak.

Rise time constant of hydroxyl-coordinated $^3Fe(CO)_3$. Kinetic plots of the hydroxyl-coordinated $^3Fe(CO)_3$ in 1-hexanol, 1-butanol, 1-propanol and methanol are presented in Figure B4 and B5. The rise time constants are fitted to a single exponential up to 200 ps, data for $^3Fe(CO)_3$•(OHC_4H_9) are fitted up to 400 ps; the error is one standard deviation of the mean.

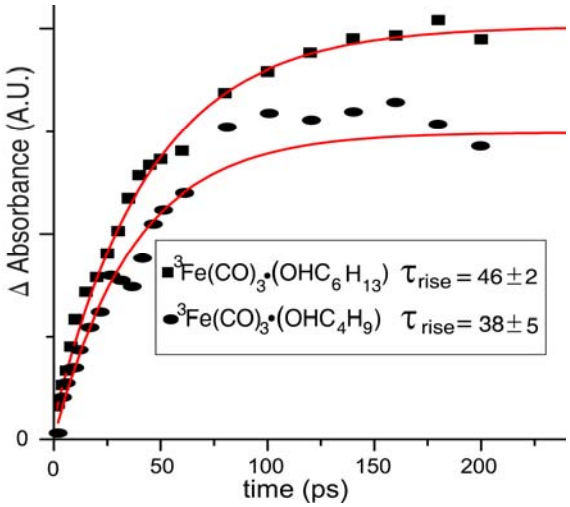

Figure B4. TRIR kinetic trace of hydroxyl-coordinated $^3Fe(CO)_3$•(OHC_6H_{13}) in 1-hexanol solution and hydroxyl-coordinated $^3Fe(CO)_3$•(OHC_4H_9) in 1-butanol solution with 267-nm excitation. The peak areas of both species are baseline-corrected and integrated from 1883 to 1903 cm^{-1}.

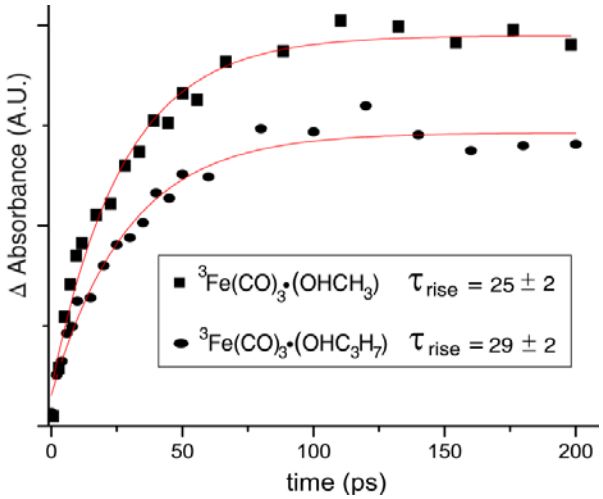

Figure B5. TRIR kinetic trace of hydroxyl-coordinated $^3Fe(CO)_3$•$(OHCH_3)$ in methanol solution and hydroxyl-coordinated $^3Fe(CO)_3$•(OHC_3H_7) in 1-propanol solution with 267 nm excitation. The peak areas of both species are baseline-corrected and integrated from 1883 to 1903 cm^{-1}.

Intensity dependence of photoproduct yield. To confirm that $Fe(CO)_3$ and $FeC(O)_4$ are indeed the results of a single-photon absorption, we quantified the dependence of their yields on the laser power of 267-nm pulse. We observed a linear dependence of the reaction yield on the intensity of pump pulses (Figure B3), consistent with a single-photon absorption process. This result has also been confirmed by other authors. Experiments with 400-nm excitation in both alkane and alcohol solution do not create any $Fe(CO)_3$ product, since the energy of the excitation photon is quite close to the required energy for breaking the two first Fe–CO bonds.

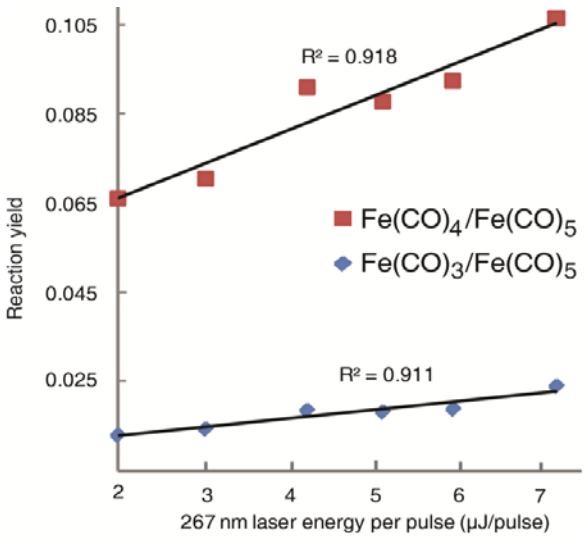

Figure B6. Reaction yields of $Fe(CO)_3$ and $Fe(CO)_4$ after 267-nm photolysis of $Fe(CO)_5$ in *n*-heptane solution. Reaction yields are calculated base on ratio of peak areas at 1928 cm^{-1} for $Fe(CO)_3$, 1967 cm^{-1} for $Fe(CO)_4$, and 2000 cm^{-1} for $Fe(CO)_5$ at 200 ps delay in the TRIR spectra.

Molecular coordinates:

$^1Fe(CO)_3$, BP86 result

Fe	-0.00002000	-0.35931800	-0.53297500
C	0.00006600	1.28306200	-0.06605400
C	1.64343400	-0.55359100	0.10453000
C	-1.64350300	-0.55351500	0.10451800
O	0.00013300	2.42346300	0.21023500
O	2.63994100	-0.69389700	0.70734000
O	-2.64000600	-0.69374900	0.70734900

$^1Fe(CO)_3$, B3LYP result

Fe	-0.00000500	-0.31218800	-0.53525500
C	0.00001800	1.35693700	-0.02218900
C	1.65256800	-0.59180900	0.09879600
C	-1.65259900	-0.59178600	0.09876700
O	0.00003400	2.47740600	0.25897800
O	2.63488400	-0.79641900	0.67452700
O	-2.63489300	-0.79638100	0.67454400

$^3Fe(CO)_3$, BP86 result

Fe	-0.00000400	-0.00001100	0.71117600
C	-1.55984400	-0.42568800	-0.09306900
C	1.14858300	-1.13800900	-0.09307700
C	0.41125400	1.56370200	-0.09304200
O	-2.52333100	-0.68861000	-0.70066400

O	1.85803800	-1.84094400	-0.70066500
O	0.66531100	2.52958700	-0.70060200

$^{3}Fe(CO)_{3}$, B3LYP result

Fe	-0.00002300	0.00001000	0.66116000
C	0.16823200	1.67025000	-0.10770700
C	-1.53060900	-0.68943900	-0.10770400
C	1.36236900	-0.98082400	-0.10762100
O	0.27103900	2.69049200	-0.63553800
O	-2.46553300	-1.11055500	-0.63557400
O	2.19457500	-1.57996200	-0.63538500

$^{1}Fe(CO)_{3}$•$OHC_{6}H_{13}$, BP86 result

Fe	0.13206600	-0.14688000	0.18567500
C	-1.18360800	-0.96455500	-0.64949300
C	0.76706700	0.34865000	-1.34348800
C	0.24452000	1.51996900	0.73913100
O	-2.15846100	-1.30964900	-1.21377800
O	1.24862300	0.64921000	-2.37077000
O	0.12625900	2.66443200	0.99283300
C	0.02623900	-0.55517800	3.29225500
H	0.77244400	0.24769700	3.22543000
H	0.41598400	-1.34661900	3.95506100
O	-0.01850300	-1.11307400	1.93465100
H	-0.65946900	-1.84543500	1.90965700
C	-1.33074800	-0.03834500	3.76004400
H	-2.06093900	-0.86969400	3.76177500
H	-1.69658600	0.70922700	3.03634800
C	-1.25910500	0.58136600	5.16994600
H	-0.87337700	-0.16802500	5.88594000
H	-0.52875900	1.41084400	5.16607400
C	-2.61883200	1.10532300	5.66631600
H	-3.35138400	0.27659000	5.66967500
H	-3.00475100	1.85237900	4.94857000
C	-2.55696300	1.73377600	7.06985700
H	-2.17003600	0.98661500	7.78676300
H	-1.82381700	2.56070800	7.06512500
C	-3.91612800	2.25779700	7.55961400
H	-4.66286300	1.44814800	7.61009300
H	-3.83661600	2.70083000	8.56478700
H	-4.31250700	3.03335600	6.88378200

$^{1}Fe(CO)_{3}$•$OHC_{6}H_{13}$, B3LYP result

Fe	0.14542500	-0.14993800	0.15640700
C	-1.17613200	-0.98051400	-0.68836100

C	0.87674300	0.31216500	-1.37384500
C	0.19000600	1.53271900	0.71688400
O	-2.14074900	-1.33408000	-1.23322400
O	1.42012800	0.57242100	-2.36277200
O	0.02465800	2.65157300	0.98848900
C	-0.00722700	-0.52691000	3.27350900
H	0.72804500	0.27648000	3.20288100
H	0.39251500	-1.30818400	3.93073700
O	-0.07333400	-1.07786200	1.92687400
H	-0.66341500	-1.84237600	1.91133100
C	-1.35731700	-0.01787000	3.75980000
H	-2.07981900	-0.84734100	3.76302200
H	-1.73221900	0.72905500	3.04999300
C	-1.27119900	0.59076000	5.16842700
H	-0.88077400	-0.15944900	5.87110300
H	-0.54541900	1.41587500	5.16244200
C	-2.62190500	1.10985900	5.68097700
H	-3.34982300	0.28555500	5.68653200
H	-3.01221500	1.85824500	4.97690400
C	-2.54525900	1.72643200	7.08436900
H	-2.15490600	0.97786000	7.78793900
H	-1.81674900	2.54887700	7.07785000
C	-3.89680800	2.24586900	7.58887200
H	-4.63808900	1.43939500	7.63917100
H	-3.80852000	2.67927400	8.59084900
H	-4.29589100	3.02157400	6.92471300

^{3}**Fe(CO)$_3$•OHC$_6$H$_{13}$**, BP86 result

Fe	0.18746800	0.20170700	0.50074300
C	-0.67504500	-0.24631500	-1.01530700
C	1.58845000	-0.91617000	0.33378900
C	0.97294000	1.71326400	-0.08729500
O	-1.16820700	-0.52669100	-2.04219200
O	2.51137000	-1.61720400	0.14997400
O	1.51197200	2.65381100	-0.53396900
C	-0.62124800	-0.23583700	3.51806900
H	-1.48816400	-0.14882000	4.19854000
H	-0.19069900	-1.25119500	3.60491100
O	-1.10311300	-0.04049200	2.14552900
H	-1.82650500	-0.66743900	1.95879800
C	0.42305300	0.83247200	3.81264000
H	-0.04507400	1.82996700	3.71899700
H	1.21406100	0.77427400	3.03687100
C	1.05065900	0.66852200	5.21050200
H	0.25370400	0.70067800	5.98049100

H	1.51908400	-0.33245300	5.29071000
C	2.10224000	1.74846500	5.52573800
H	1.63543400	2.75011700	5.43998800
H	2.90071600	1.71592200	4.75805000
C	2.73209500	1.59891300	6.92255100
H	1.93226500	1.63214600	7.68844400
H	3.19570600	0.59643300	7.00732700
C	3.78328800	2.67850100	7.22985200
H	3.34176100	3.69042900	7.18640100
H	4.21608300	2.54538300	8.23628300
H	4.61339800	2.64666700	6.50151100

$^{3}Fe(CO)_{3}$•$OHC_{6}H_{13}$, B3LYP result

Fe	0.17954700	0.15459300	0.42523600
C	-0.76978500	-0.27057600	-1.09783500
C	1.64763000	-0.93305500	0.17676600
C	0.88737000	1.77762600	-0.09765300
O	-1.33358600	-0.53032400	-2.07491900
O	2.57181500	-1.60392300	-0.01303400
O	1.34319800	2.77936200	-0.45354000
C	-0.56709000	-0.25947600	3.52743400
H	-1.43073100	-0.12245400	4.18864700
H	-0.17344400	-1.27472400	3.66007000
O	-1.02266600	-0.10857600	2.15369700
H	-1.79581900	-0.66529500	1.99653700
C	0.50130200	0.78370500	3.80723600
H	0.07556200	1.78085500	3.64012900
H	1.31751500	0.65876200	3.08286600
C	1.05523000	0.67916800	5.23626200
H	0.23247400	0.78765300	5.95762500
H	1.47446700	-0.32452300	5.39484300
C	2.13239900	1.73039700	5.53818900
H	1.71457800	2.73443800	5.37675200
H	2.95561700	1.62278200	4.81772500
C	2.69177100	1.63802000	6.96433100
H	1.86790700	1.74507400	7.68376400
H	3.10884200	0.63409900	7.12473800
C	3.76711300	2.69048300	7.25933900
H	3.37085500	3.70601300	7.14118500
H	4.14539900	2.59804900	8.28307000
H	4.62022500	2.58690100	6.57848700

Appendix C. Supporting information for Chapter 5

Predicting the local solvent temperature of a photoreaction via a thermal conduction model:

In this model, each photoproduct molecule is treated as a point heat source and the surrounding solvent is considered as a continuum. The temperature distribution at time t is described by:

$$T(x,y,z,t) = \frac{1}{8(\pi\chi t)^{3/2}} \int_{-\infty}^{\infty}\int_{-\infty}^{\infty}\int_{-\infty}^{\infty} dx'dy'dz' T_o(x',y',z') \times exp\left[-\frac{(x-x')^2+(y-y')^2+(z-z')^2}{4\chi t}\right]$$

Where $T_o(x',y',z')$ is the initial temperature distribution at the heat source. Since $T_o(x',y',z')$ can be considered as a δ function, $Q\delta(x')\delta(y')\delta(z')$ at the origin, the equation becomes:

$$T(r,t) = \frac{Q}{8(\pi\chi t)^{3/2}} exp\left[-\frac{r^2}{4\chi t}\right]$$

Where r is the distance from the origin, and Q is the strength of the heat source, defined as $E/\rho C$. E is the heat released from each photoreaction molecule, and ρ and C are the density and the heat capacity of the solvent.

Since E changes according to time, we can describe E as $\frac{A}{\tau}e^{-t/\tau}$ where τ is the time constant for heat transfer from photoproduct to solvent, and A is a normalized constant satisfying $\int_0^{\infty} Edt$, equal to total heat transfer from a single photoreaction center.

For example, in the case of the $Cr(CO)_6$, the total heat transfer after 267 nm photodissociation is 107 (the photon energy) -37 (the M-CO bond strength) = 70 kcal/mol, and the heat transfer time τ is 7.8 ps. Inserting these values into our equation for $T(r,t)$, we can calculate the temperature increase of the solvent, relative to the room temperature, at any distance from the center of the photoproduct and at any time after the photoreaction has taken place (see Figure 5).

In the case that $Cr(CO)_6$ absorbs the excitation photons but follow a non-radiative relaxation or a fast recovery (in fs regime) from geminate recombination of photoproducts to dissipate all of the excitation in to heat, we adapt the total heat transfer of 107 kcal/mol and the heat transfer time of 7.8 ps to calculate the evolution of temperature increase of local solvent. Figure S1 shows the result of the calculation.

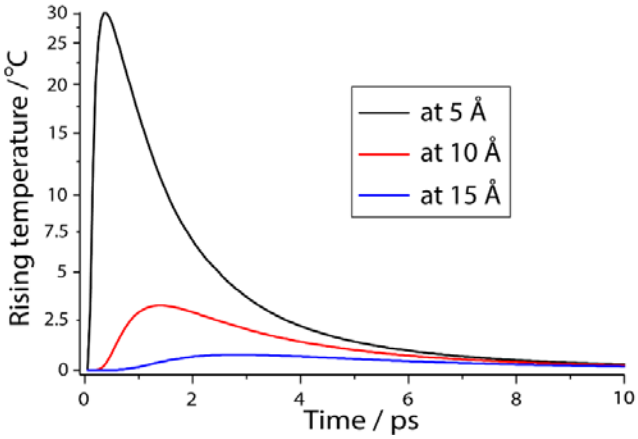

Figure C1: Calculated temperature increase (relative to room temperature) of local AcN solvent at various distances from a non-radiative relaxation of $Cr(CO)_6$ molecule after 267 nm excitation via thermal conduction model.

Figure C2 shows the similar calculation for a photoisomerization reaction of *cis*-stilbene to *trans*-stilbene when we adapt the heat transfer rate of 14.8 ps and the total heat transfer after 267 nm excitation is 107 (the photon energy) - 4 (the enthalpy energy change) = 103 kcal/mol.

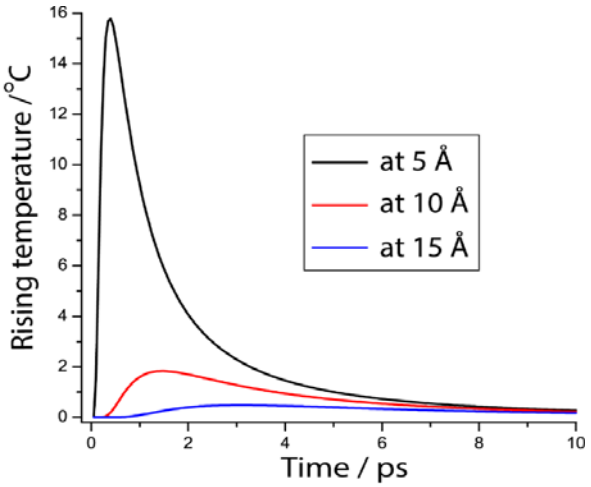

Figure C2: Calculated temperature increase (relative to room temperature) for of local AcN solvent at various distances from a photoisomerization of cis-stilbene to trans-stilbene via thermal conduction model.

Due to the long distance between solutes in this experiment (i.e. low concentrations were used), the quick drop in temperature confirms the initial assumption to treat the solvent as infinite medium is valid. Though the continuum assumption of solvent medium at short distance does not describe precisely the specific structural interaction between photoproducts and solvent, this assumption is still strongly supported in this study because the heat transfer via translational and rotational motions are not really sensitive to the composition and structure of the solvent.

Appendix D. Supporting information for Chapter 6

1. FTIR spectra of studied solutes

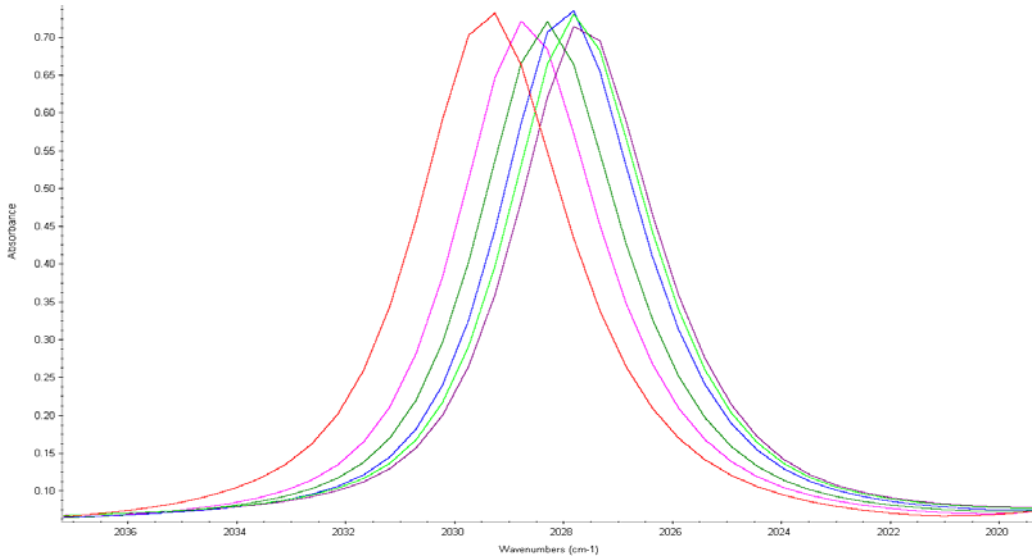

Figure D1. FTIR spectra of $CpMn(CO)_3$ in the region used to determine τ_C. The center frequency redshifts slightly moving from *n*-pentane, *n*-heptane, *n*-nonane, *n*-dodecane, *n*-tetradecane, to *n*-hexadecane. The spectral widths (HWHM) are 3.3 cm^{-1} in all solvents, except 3.5 cm^{-1} in *n*-pentane.

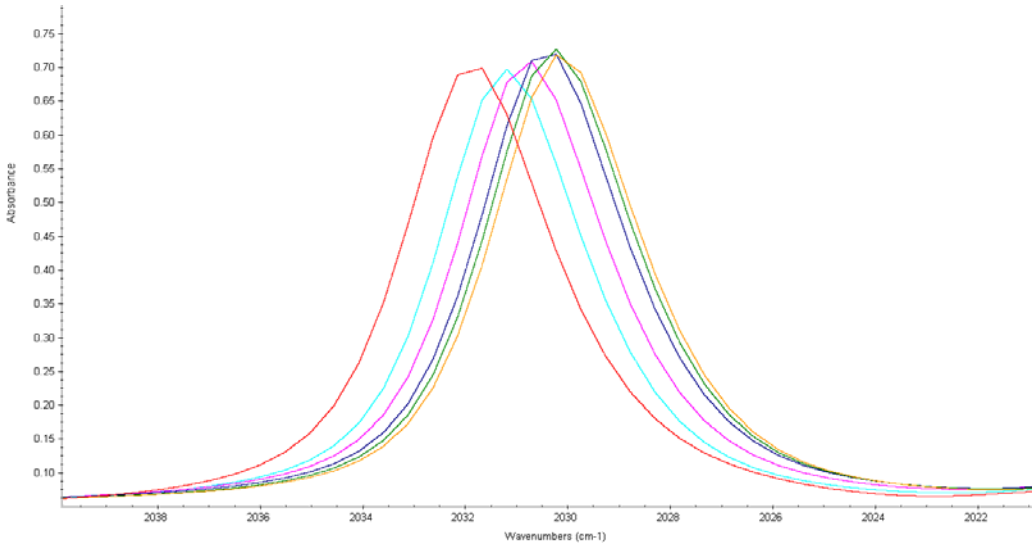

Figure D2. FTIR spectra of $CpRe(CO)_3$ in the region used to determine τ_C. The center frequency redshifts slightly moving from *n*-pentane, *n*-heptane, *n*-nonane, *n*-dodecane, *n*-tetradecane, to *n*-hexadecane. The spectral widths (HWHM) are 3.0 cm^{-1} in all solvents, except 3.3 cm^{-1} in *n*-pentane and 3.1 cm^{-1} in *n*-heptane.

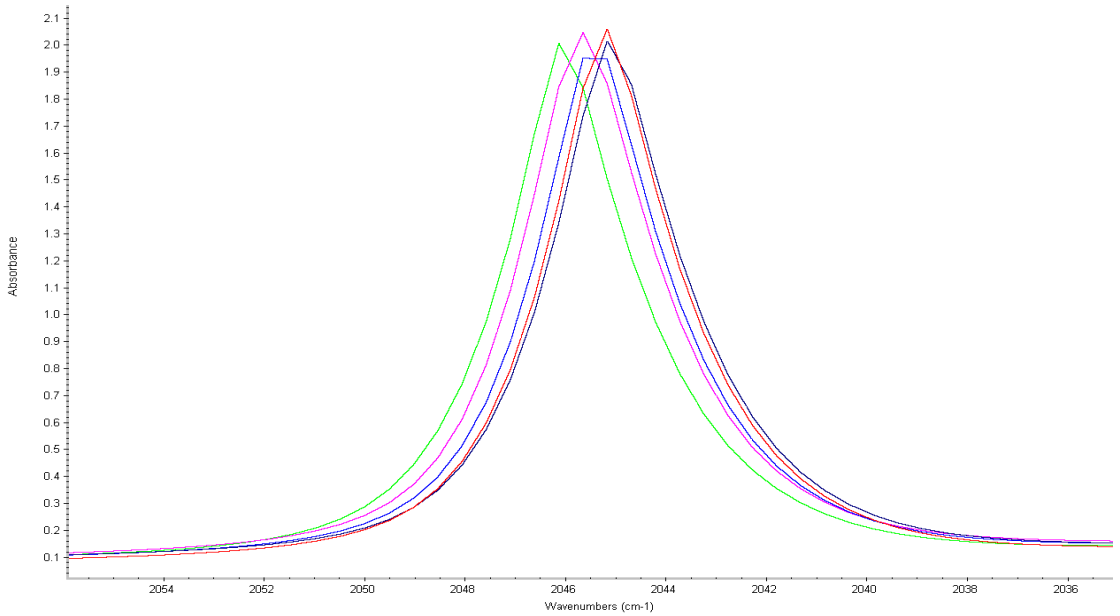

Figure D3. FTIR spectra of $Mn_2(CO)_{10}$ in the region used to determine τ_C. The center frequency redshifts slightly moving from *n*-pentane, *n*-heptane, *n*-nonane, *n*-dodecane to *n*-tetradecane. The spectral widths (HWHM) are 3.2 cm^{-1} in all solvents, except 3.4 cm^{-1} in *n*-pentane.

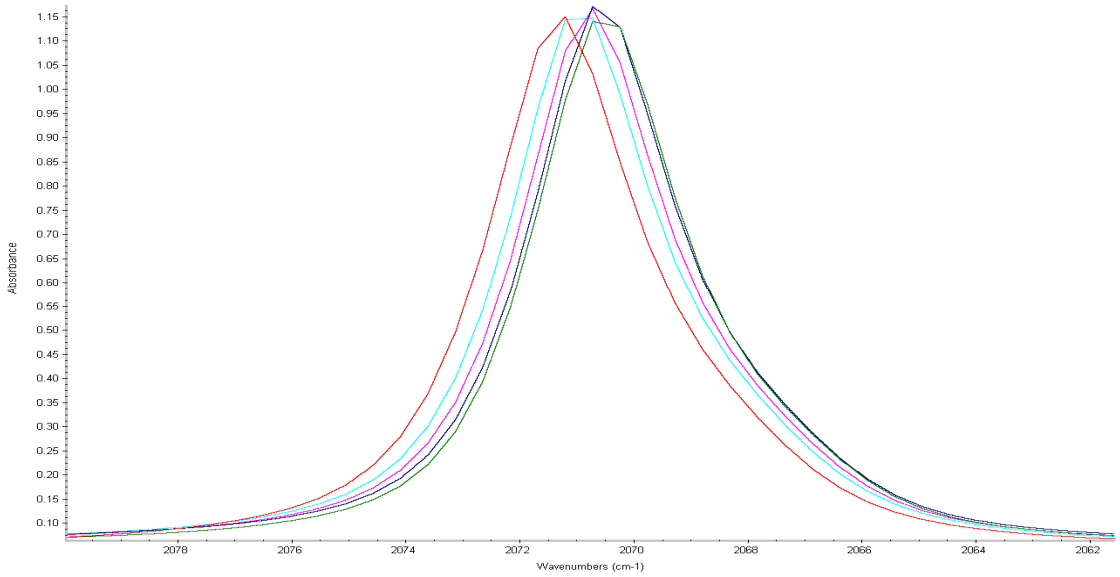

Figure D4. FTIR spectra of $Re_2(CO)_{10}$ in the region used to determine τ_C. The center frequency redshifts slightly moving from *n*-pentane, *n*-heptane, *n*-nonane, *n*-dodecane, *n*-tetradecane. The spectral width (HWHM) is 3.5 cm^{-1} in *n*-pentane, 3.4 cm^{-1} in *n*-heptane and *n*-nonane, and 3.3 cm^{-1} in *n*-dodecane and *n*-tetradecane.

2. The ln(r(t)) vs. t plot of data in Figure 6.3

To further demonstrate the quality of the fits of the exponential decays in Figure 6.3, we have replotted the same data from Figure 6.3 to show the linear relationship between ln(r(t)) and t in the below figures.

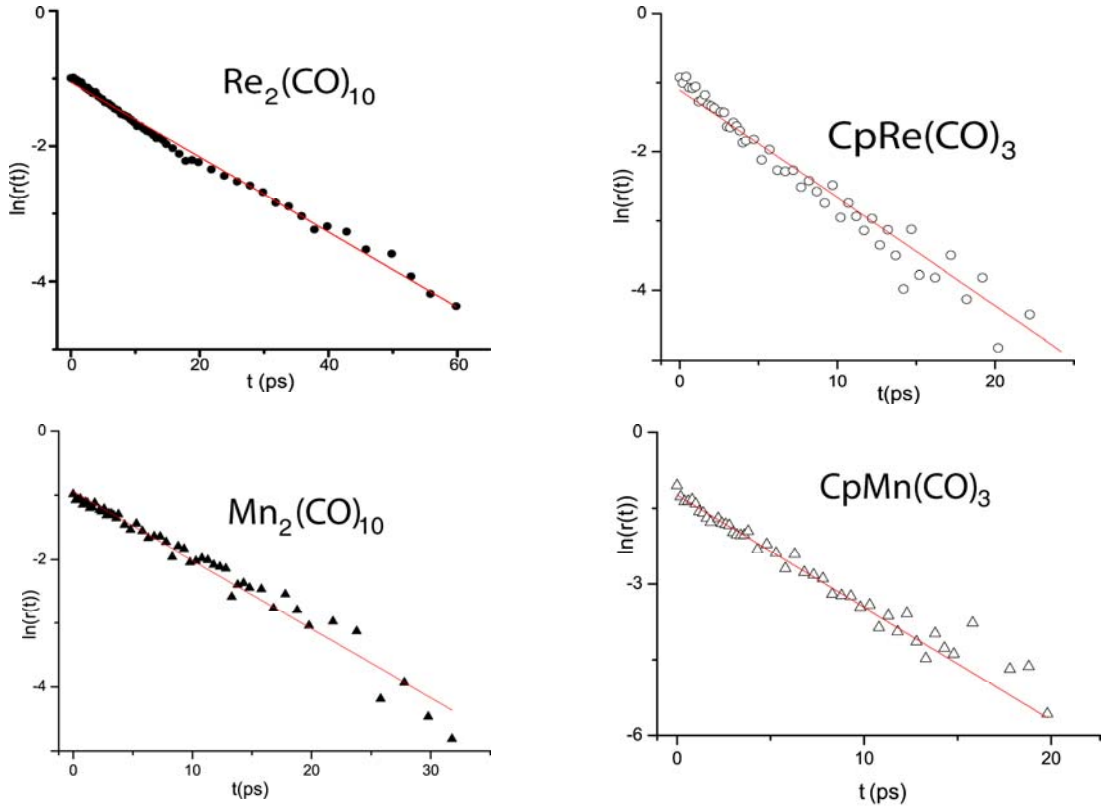

Figure C5: Time-dependent polarization anisotropies of $CpM(CO)_3$ and $M_2(CO)_{10}$ (M=Mn, Re) in *n*-heptane solution obtained from narrow-band IR pump broad-band IR probe spectroscopy. The data are plotted as ln(r(t)) vs. t to demonstrate the quality of the fits of the exponential decays in Fig. 6.3.

3. Characteristics of the IR vibrations

In all solute molecules, the IVR is about 2-4 ps. The vibrational lifetime for $CpMn(CO)_3$, $CpRe(CO)_3$, $Mn_2(CO)_{10}$, $Re_2(CO)_{10}$ in all solvents are about 41 ± 4, 33 ± 5, 158 ± 14, 105 ± 25 ps, respectively (these are the values in *n*-pentane, they are similar in other solvents). Within the experimental error, we do not see any significant solvent dependence of vibrational lifetime.

The nature of the monitored vibrational mode in each molecule changes slightly. This is evident from the fact that the frequencies and the lifetimes of the vibrations are different for

the Mn vs. Re species. We expect the pi back-bonding would be a bit stronger for the Re species since a theoretical study of relativistic effect shows this trend for similar structure compounds, $C_8H_6[Mn(CO)_3]_2$ and $C_8H_6[Re(CO)_3]_2$. DFT frequency calculations show that the monitored vibrations in each solute pairs are delocalized along local carbonyls stretching and the contribution of each carbonyl stretching is similar among the different congeners in each pair. We believe that the effects of such differences in the vibrational modes of each congener on the differences in the rotational correlation times must be quite small, since the rotational motion of the solute is a diffusive process, which is not controlled by the vibrational modes.

4. Molecular polarizability

To compare the molecular polarizability of the solutes, we report the calculated isotropic polarizability (the average of dipole polarizability tensor components along the three principle axes) from the frequency calculation by Gaussian software:

Solutes	Isotropic polarizability ($Bohr^3$)
$CpMn(CO)_3$	122.2
$CpRe(CO)_3$	134.3
$Mn_2(CO)_{10}$	216.1
$Re_2(CO)_{10}$	242.8

When replacing Mn by Re in the $CpM(CO)_3$ pairs and $M_2(CO)_{10}$ pairs, the calculated polarizabilties increase by 10 and 12 %, respectively

Molecular coordinates:

$CpMn(CO)_3$

Mn	2.16712600	0.87252800	0.60025700
C	1.39591900	2.90043700	0.68437800
H	2.01482500	3.79569800	0.63665300
C	0.80922200	2.20959400	-0.43524700
H	0.91836700	2.48431000	-1.48446400
C	0.07672000	1.08816400	0.06393800
H	-0.47099400	0.36300100	-0.53773400
C	1.01330900	2.19593800	1.87466500
H	1.30772000	2.45697900	2.89146800
C	0.20261700	1.07561900	1.50054500
H	-0.23798400	0.34563200	2.17882200
C	3.39177700	1.07380900	-0.67298700
C	3.41139600	0.75124000	1.86505600
C	2.11947800	-0.89148600	0.38375900
O	4.18290700	1.23265900	-1.52467500

O	2.05396000	-2.05438800	0.24234600
O	4.21618400	0.69127500	2.71646100

$CpRe(CO)_3$

Re	2.24141000	0.82132100	0.59325300
C	1.29670900	2.97485800	0.69193900
H	1.89672100	3.88276400	0.64291700
C	0.70924100	2.27597000	-0.42817300
H	0.80336400	2.55760100	-1.47713000
C	-0.02498600	1.15407200	0.07590700
H	-0.58814900	0.43735000	-0.52176100
C	0.92241600	2.26469000	1.88596700
H	1.20964300	2.53455200	2.90271600
C	0.10221200	1.14492300	1.51703800
H	-0.35425500	0.42863200	2.19935800
C	3.58512800	1.00771900	-0.76215500
C	3.60469800	0.65724400	1.93204800
C	2.23312400	-1.08110600	0.35270600
O	4.37231600	1.17495100	-1.61956400
O	2.15847200	-2.24546900	0.20600200
O	4.40448700	0.60093500	2.79217200

$Mn_2(CO)_{10}$

Mn	0.00000000	0.00000000	1.46812600
Mn	0.00000000	0.00000000	-1.46812600
C	0.70386100	-1.70061800	1.36401300
C	1.70061800	0.70386100	1.36401300
C	0.00000000	0.00000000	3.25918200
C	-0.70386100	1.70061800	1.36401300
C	-1.70061800	-0.70386100	1.36401300
C	-1.70061800	0.70386100	-1.36401300
C	-0.70386100	-1.70061800	-1.36401300
C	0.70386100	1.70061800	-1.36401300
C	1.70061800	-0.70386100	-1.36401300
C	0.00000000	0.00000000	-3.25918200
O	-1.14894200	2.77599900	1.36167400
O	-2.77599900	1.14894200	-1.36167400
O	0.00000000	0.00000000	-4.42594000
O	-1.14894200	-2.77599900	-1.36167400
O	1.14894200	-2.77599900	1.36167400
O	2.77599900	-1.14894200	-1.36167400
O	1.14894200	2.77599900	-1.36167400
O	2.77599900	1.14894200	1.36167400
O	0.00000000	0.00000000	4.42594000
O	-2.77599900	-1.14894200	1.36167400

$Re_2(CO)_{10}$

Re	0.00000000	0.00000000	1.56148400
Re	0.00000000	0.00000000	-1.56148400
C	-0.76271900	-1.84740000	1.44048300
C	1.84740000	-0.76271900	1.44048300
C	0.00000000	0.00000000	3.50351100
C	0.76271900	1.84740000	1.44048300
C	-1.84740000	0.76271900	1.44048300
C	-0.76271900	1.84740000	-1.44048300
C	-1.84740000	-0.76271900	-1.44048300
C	1.84740000	0.76271900	-1.44048300
C	0.76271900	-1.84740000	-1.44048300
C	0.00000000	0.00000000	-3.50351100
O	1.20666500	2.92244600	1.38652100
O	-1.20666500	2.92244600	-1.38652100
O	0.00000000	0.00000000	-4.67260300
O	-2.92244600	-1.20666500	-1.38652100
O	-1.20666500	-2.92244600	1.38652100
O	1.20666500	-2.92244600	-1.38652100
O	2.92244600	1.20666500	-1.38652100
O	2.92244600	-1.20666500	1.38652100
O	0.00000000	0.00000000	4.67260300
O	-2.92244600	1.20666500	1.38652100

n-pentane (linear configuration)

C	-2.57086500	0.32515500	0.00000000
H	-3.47672000	-0.30572800	0.00000000
H	-2.61743900	0.97737800	-0.89082500
H	-2.61744000	0.97737800	0.89082500
C	-1.28945900	-0.52468900	0.00000000
H	-1.28830500	-1.19180400	-0.88454000
H	-1.28830500	-1.19180400	0.88454000
C	0.00000000	0.31582500	0.00000000
H	0.00000000	0.98431200	-0.88512700
H	0.00000000	0.98431100	0.88512700
C	1.28945900	-0.52468900	0.00000000
H	1.28830500	-1.19180400	-0.88454000
H	1.28830500	-1.19180400	0.88454000
C	2.57086500	0.32515500	0.00000000
H	2.61743900	0.97737800	-0.89082500
H	2.61744000	0.97737800	0.89082500
H	3.47672000	-0.30572800	0.00000000

n-pentane (roll configuration)

C	1.92587100	-0.65998100	-0.33985000
H	2.76199100	-1.17526800	0.16415300
H	2.35269600	-0.05195500	-1.15852400
H	1.29131000	-1.43714800	-0.80064200
C	1.13655000	0.21702500	0.64766600
H	1.83391400	0.91988800	1.14215300
H	0.72684400	-0.41628000	1.45784000
C	-0.00000100	1.03791300	0.00000000
H	0.43940900	1.70475100	-0.76851200
H	-0.43940100	1.70475600	0.76851300
C	-1.13654900	0.21702800	-0.64766400
H	-1.83392000	0.91988700	-1.14214800
H	-0.72685100	-0.41627800	-1.45784400
C	-1.92587000	-0.65998200	0.33984900
H	-2.76200100	-1.17525100	-0.16415500
H	-1.29131400	-1.43716400	0.80062400
H	-2.35267900	-0.05196100	1.15853600

n-hexadecane (linear configuration)

C	-9.66231400	-0.33637600	0.00000000
H	-9.71523300	-0.98813700	0.89083800
H	-9.71523100	-0.98813700	-0.89084000
H	-10.56189900	0.30337600	0.00000000
C	-8.37275200	0.50100500	0.00000000
H	-8.36498600	1.16803500	-0.88453700
H	-8.36498700	1.16803500	0.88453900
C	-7.09157000	-0.35235500	0.00000000
H	-7.09899200	-1.02042800	0.88521400
H	-7.09899200	-1.02042900	-0.88521000
C	-5.79481500	0.47669200	0.00000000
H	-5.78838300	1.14453400	0.88525900
H	-5.78838400	1.14453500	-0.88525700
C	-4.51421400	-0.37732700	0.00000000
H	-4.52067500	-1.04516300	-0.88521900
H	-4.52067400	-1.04516300	0.88521800
C	-3.21750500	0.45198700	-0.00000200
H	-3.21110900	1.11982800	0.88522700
H	-3.21111000	1.11982700	-0.88523300
C	-1.93701100	-0.40215600	-0.00000200
H	-1.94348800	-1.06999700	-0.88522900
H	-1.94349000	-1.06999800	0.88522400
C	-0.64024600	0.42708200	0.00000000
H	-0.63379800	1.09492100	0.88522800
H	-0.63379600	1.09492100	-0.88522800
C	0.64024600	-0.42708200	0.00000200

H	0.63379800	-1.09492200	-0.88522600
H	0.63379600	-1.09492000	0.88523100
C	1.93701100	0.40215600	0.00000200
H	1.94348900	1.06999700	0.88522900
H	1.94348900	1.06999700	-0.88522400
C	3.21750500	-0.45198700	0.00000000
H	3.21110900	-1.11982700	-0.88522900
H	3.21111000	-1.11982700	0.88523100
C	4.51421400	0.37732700	0.00000000
H	4.52067500	1.04516400	0.88521800
H	4.52067400	1.04516300	-0.88521900
C	5.79481500	-0.47669200	0.00000000
H	5.78838400	-1.14453400	-0.88525800
H	5.78838400	-1.14453400	0.88525700
C	7.09157000	0.35235500	0.00000000
H	7.09899200	1.02042800	0.88521200
H	7.09899200	1.02042800	-0.88521200
C	8.37275200	-0.50100500	0.00000000
H	8.36498600	-1.16803500	-0.88453800
H	8.36498600	-1.16803500	0.88453800
C	9.66231400	0.33637600	0.00000000
H	9.71523200	0.98813700	0.89083900
H	10.56189900	-0.30337600	0.00000000
H	9.71523200	0.98813700	-0.89083900

n-hexadecane (roll configuration 1)

C	-4.97389800	3.48910500	-0.45491300
H	-4.88325800	4.32328000	0.26240400
H	-6.04659100	3.23803600	-0.54184100
H	-4.63934000	3.85762300	-1.44166800
C	-4.15239100	2.26767700	-0.00981700
H	-3.08785300	2.55697000	0.09744000
H	-4.48664600	1.95174700	0.99642500
C	-4.25416700	1.08459600	-0.99130700
H	-3.96627100	1.43858200	-2.00116800
H	-5.31446300	0.76792400	-1.07078700
C	-3.38563200	-0.13843000	-0.62666700
H	-3.42802100	-0.86662000	-1.46077300
H	-2.32854700	0.18430700	-0.55395400
C	-3.80765600	-0.85033300	0.67349000
H	-4.89929600	-1.04021000	0.62729000
H	-3.65424700	-0.17338500	1.53681400
C	-3.09679900	-2.18960600	0.97094900
H	-3.58820000	-2.63312600	1.85762400
H	-3.28411500	-2.89817700	0.13845800

C	-1.57178000	-2.10750100	1.23817400
H	-1.29296800	-2.88879200	1.97217300
H	-1.33786600	-1.14085200	1.72945600
C	-0.67124300	-2.28605700	-0.00082300
H	-0.89809700	-3.26574700	-0.46897600
H	-0.91419700	-1.52290000	-0.76446400
C	0.83184400	-2.21687700	0.32344700
H	1.06146700	-1.23502700	0.77977300
H	1.07277300	-2.97389500	1.09759200
C	1.73420200	-2.45790200	-0.90352200
H	1.48161200	-1.72594100	-1.69786000
H	1.47701500	-3.45055800	-1.32204400
C	3.25864800	-2.40553500	-0.62416800
H	3.76726600	-3.13805800	-1.27907900
H	3.45166400	-2.74677400	0.41320600
C	3.94022400	-1.03746700	-0.84778000
H	5.03305200	-1.16791600	-0.71569200
H	3.79831000	-0.73700900	-1.90604200
C	3.47224900	0.11167600	0.06415600
H	2.40060000	0.32371800	-0.11742600
H	3.54823400	-0.20631800	1.12394600
C	4.27696200	1.40904000	-0.13571700
H	4.21141800	1.72035900	-1.19826000
H	5.35051200	1.20630100	0.05546500
C	3.81398200	2.57130300	0.76112000
H	2.74261500	2.77591900	0.56696400
H	3.87693100	2.25884700	1.82215500
C	4.62742700	3.86000300	0.55662000
H	4.55536000	4.21640200	-0.48691100
H	4.27161500	4.67319200	1.21290000
H	5.69769700	3.69594400	0.77741300

n-hexadecane (roll configuration 2)

C	-1.95660900	-1.78066700	-0.09864400
H	-2.30383700	-2.81046300	0.12008400
H	-1.23076200	-1.87507800	-0.92822100
C	-3.16482800	-0.95483100	-0.59427500
H	-3.92462400	-0.90532700	0.20943400
H	-3.63699000	-1.51848600	-1.42143300
C	-2.82476000	0.47869100	-1.08583700
H	-1.79005900	0.47087600	-1.48056100
H	-3.46387100	0.73015000	-1.95505700
C	-2.96780100	1.61507800	-0.03777600
H	-2.77113300	1.21708500	0.97638500
H	-2.18686700	2.37784600	-0.21986900

C	-4.33431000	2.33554800	-0.04278800
H	-4.28683100	3.18263100	0.66864700
H	-4.49200700	2.78764700	-1.04249100
C	-5.54665800	1.45630200	0.30918400
H	-5.68955300	0.64134800	-0.42165000
H	-5.43093900	0.99413300	1.30652500
H	-6.47623000	2.05202400	0.32369300
C	-1.25603600	-1.23346900	1.16165600
H	-0.83228100	-0.22961700	0.96193400
H	-2.03328700	-1.08080900	1.93691100
C	-0.15190800	-2.14409800	1.75645800
H	-0.08902200	-1.94002300	2.84278900
H	-0.47431100	-3.20229600	1.67087800
C	1.28276800	-2.00897200	1.19269700
H	1.93816800	-2.62421900	1.83876700
H	1.62239800	-0.96465400	1.33439100
C	1.50255200	-2.43347000	-0.28437700
H	0.76984100	-3.22502900	-0.53206800
H	2.49437100	-2.91809300	-0.37737500
C	1.42536600	-1.29914400	-1.34218400
H	0.96624300	-1.69473300	-2.26817500
H	0.74427200	-0.50120700	-0.99073300
C	2.79202400	-0.69097400	-1.73654900
H	3.42803800	-1.50908400	-2.12949800
H	2.63813800	0.00636700	-2.58442300
C	3.57276100	0.05010800	-0.62899600
H	3.71781600	-0.61944600	0.24251400
H	4.58772700	0.26553300	-1.01331200
C	2.91994600	1.36471300	-0.16034100
H	2.80482700	2.04137400	-1.03212600
H	1.89397200	1.15875300	0.20033400
C	3.69147000	2.10293700	0.95464700
H	3.07359000	2.94909600	1.31131400
H	3.80958800	1.42505300	1.82332900
C	5.07110600	2.63783200	0.53133200
H	5.54802600	3.20238600	1.35140400
H	5.76143500	1.82453300	0.24798200
H	4.98365900	3.31822600	-0.33556200